

SEARCH FOR STANDARD MODEL TOP QUARK AND Z BOSON  
ASSOCIATED PRODUCTION AT ATLAS

By

Bradley D. Schoenrock

A DISSERTATION

Submitted to  
Michigan State University  
in partial fulfillment of the requirements  
for the degree of

Physics - Doctor of Philosophy

2018

## ABSTRACT

### SEARCH FOR STANDARD MODEL TOP QUARK AND Z BOSON ASSOCIATED PRODUCTION AT ATLAS

By

Bradley D. Schoenrock

This document reports on the search for the production of a top quark in association with a  $Z$  boson using data from the ATLAS detector. The data was collected during 2015, from proton-proton collisions at a center-of-mass energy of 13 TeV delivered by the Large Hadron Collider (LHC) at CERN. To isolate this production mode, selection requirements are made on the three leptons, b-quark jet and light quark jet that  $tZ$  naturally contains. A profile likelihood fit is performed to put an upper limit on the Standard Model predicted cross-section. The resulting measurement is consistent with the Standard Model prediction.

To my wonderful, beautiful, loving, at times odd, but always supportive wife Rachel.  
I love you.

## **ACKNOWLEDGMENTS**

I would like to thank the following people.

My family, specifically my parents. Without their guidance I would not be the person I am today. I often think they should have written a parenting book because of the remarkable example they have set for me.

The members of the Wisconsin Trailblazers. Growing up around all of you showed me what hard work and kindness could accomplish.

My wife Rachel, who has inspired me every day to accomplish all that I have.

My high school teachers who took an interest in the education of every student they taught. They inspired me to be creative and investigative when I solved problems which were skills that served me well in graduate school and life.

My undergraduate and graduate professors, specifically Dr. Tireman and Dr. Donovan who encouraged me to get involved with research as an undergraduate.

My committee members who oversaw this research: Drs. Reinhard Schwienhorst, Kirsten Tollefson, Carl Schmidt, Norman Birge, and Gerd Kortemeyer.

My adviser Reinhard Schwienhorst for his continued mentorship.

All of the post docs and other students who I have had the pleasure of working with at MSU. Some of you helped me debug code while others gave me something to smile at every day.

The entire ATLAS community without which there would be no experiment nor chance at answering the great questions.

## TABLE OF CONTENTS

<b>LIST OF TABLES . . . . .</b>	<b>vii</b>
<b>LIST OF FIGURES . . . . .</b>	<b>viii</b>
<b>Chapter 1 Introduction . . . . .</b>	<b>1</b>
1.1 The Standard Model . . . . .	1
1.2 Feynman Diagrams . . . . .	6
1.3 Top Quark Physics . . . . .	7
1.4 tZ Associated Production . . . . .	10
<b>Chapter 2 CERN, the LHC, and ATLAS . . . . .</b>	<b>15</b>
2.1 The Accelerator Chain . . . . .	16
2.2 The Large Hadron Collider . . . . .	16
2.3 ATLAS . . . . .	22
2.3.1 Magnet System . . . . .	25
2.3.2 Inner Detector . . . . .	29
2.3.3 Calorimeters . . . . .	31
2.3.4 Muon Systems . . . . .	35
<b>Chapter 3 The Trigger System on ATLAS . . . . .</b>	<b>39</b>
3.1 Level 1 Trigger and Data Acquisition (DAQ) . . . . .	41
3.2 High Level Trigger (HLT) . . . . .	43
3.3 Trigger Chains . . . . .	43
3.3.1 Single Muon . . . . .	44
3.3.2 Single Electron . . . . .	44
<b>Chapter 4 Event Simulation . . . . .</b>	<b>47</b>
4.1 The Monte Carlo Method . . . . .	48
4.2 Signal Simulation . . . . .	49
4.3 Diboson Production . . . . .	50
4.4 Top-Quark Pair Production . . . . .	50
4.5 Top-Quark Pair + Boson Production . . . . .	51
4.6 Z boson+jets . . . . .	51
4.7 Single Top Quark . . . . .	51
4.8 W boson+jets and Multijet . . . . .	52
4.9 Weighting and Corrections . . . . .	52
<b>Chapter 5 Object &amp; Event Reconstruction . . . . .</b>	<b>54</b>
5.1 Electron Reconstruction . . . . .	54

5.2	Muon Reconstruction . . . . .	55
5.3	Jet Reconstruction . . . . .	56
5.3.1	Jet <i>b</i> -tagging . . . . .	57
5.4	<i>Z</i> boson . . . . .	58
5.5	Missing Transverse Energy ( $E_T^{\text{miss}}$ ) and the <i>W</i> boson . . . . .	59
5.6	Reconstructing the top quark . . . . .	60
<b>Chapter 6</b>	<b>Analysis . . . . .</b>	<b>62</b>
6.1	Preselection . . . . .	62
6.2	Control Regions . . . . .	69
6.3	Cut Flow . . . . .	79
<b>Chapter 7</b>	<b>Results . . . . .</b>	<b>87</b>
7.1	Systematic Uncertainties . . . . .	87
7.2	Statistical Analysis . . . . .	93
7.3	Outlook . . . . .	94
<b>Chapter 8</b>	<b>Conclusion . . . . .</b>	<b>96</b>
<b>BIBLIOGRAPHY . . . . .</b>		<b>97</b>

## LIST OF TABLES

Table 1.1: The cross-section for different modes of single top-quark production at the LHC at $\sqrt{s} = 8$ TeV [1] [2]. . . . .	10
Table 4.1: Information on generators for each process considered. All cross-sections consider full decays including hadronic. . . . .	48
Table 6.1: Event yields for various stages of analysis to compare with control region (CR) yields. The final selection is described in Section 6.3 and uncertainties provided on the final selection are described in Chapter 7 taken in quadrature for each sample. They are provided here for reference. . . . .	70
Table 6.2: Event yields after selection cuts are applied. Uncertainties provided on the final selection are the uncertainties described in Chapter 7 taken in quadrature for each sample. . . . .	80
Table 7.1: Systematic uncertainties related to background normalization and theory modeling. Other Top is the combination of $t\bar{t}V$ and single top. . . . .	91
Table 7.2: Systematic uncertainties related to object identification, resolution, and scale. Other Top is the combination of $t\bar{t}V$ and single top. . . . .	92

## LIST OF FIGURES

Figure 1.1: The SM of high energy physics [3]. . . . .	2
Figure 1.2: History of high energy physics illustrating the time it took from theorizing the existence of the particles until discovery [4]. . . . .	4
Figure 1.3: Representative Feynman diagram for the $t$ -channel single top quark process [5]. . . . .	9
Figure 1.4: Representative Feynman diagrams for the $Wt$ -channel single top quark process [5]. . . . .	9
Figure 1.5: Representative Feynman diagram for the $s$ -channel single top quark process [5]. . . . .	9
Figure 1.6: Representative Feynman diagram for the $tZ$ associated production decaying to three leptons via a $Z$ boson and a $W$ boson [6]. . . . .	11
Figure 1.7: Top-Quark pair and single top quark cross-sections with and without accompanying $Z$ boson [7]. . . . .	12
Figure 1.8: Information drawn from simulation of $tZ$ . Light quark $p_T$ and $\eta$ as well as $b$ -quark $p_T$ and $\eta$ . This simulation is described in detail in Section 4.2 with added simulation steps taken for a more complete analysis. . . . .	13
Figure 1.9: Information drawn from simulation of $tZ$ . The $p_T$ of other objects in $tZ$ including the lepton from the decay of the $Z$ boson and the lepton from the decay of the $W$ boson. This simulation is described in detail in Section 4.2 with added simulation steps taken for a more complete analysis. . . . .	14
Figure 2.1: Diagram of the accelerator complex for protons to get to the LHC [8]. . . . .	17
Figure 2.2: A Segment of the LHC beampipe [9]. . . . .	18
Figure 2.3: Peak instantaneous luminosity over time [10]. . . . .	20
Figure 2.4: Total LHC delivered integrated luminosity over time for run 1 [10] . . . . .	20
Figure 2.5: Total LHC delivered integrated luminosity over time for run 2 [10] . . . . .	20

Figure 2.6: Number of interactions per bunch crossing for 7 and 8 TeV [10]. . . . .	21
Figure 2.7: Number of interactions per bunch crossing for 13 TeV [2.6]. . . . .	21
Figure 2.8: ATLAS with its namesake toroidal magnets prominently visible [11]. . .	24
Figure 2.9: Cutaway diagram of ATLAS [12]. . . . .	25
Figure 2.10: A figure diagramming how particle identification can be achieved using multiple layers of the detector [13]. . . . .	26
Figure 2.11: Illustration of the ATLAS magnet system, showing the barrel solenoid, barrel toroid, and endcap toroid coils [14]. . . . .	27
Figure 2.12: A mapping of the magnetic fields in ATLAS [15]. . . . .	28
Figure 2.13: Cutaway diagram of the ATLAS inner detector [16]. . . . .	30
Figure 2.14: Track reconstruction efficiencies for the ID in ATLAS [17]. . . . .	32
Figure 2.15: Cutaway diagram of the ATLAS calorimeter systems [18]. . . . .	33
Figure 2.16: Cutaway diagram of the ATLAS muon spectrometer and toroid magnet systems [19]. . . . .	36
Figure 2.17: The TGC wheel [20]. . . . .	37
Figure 3.1: A $Z$ boson decaying to an electron positron pair. . . . .	41
Figure 3.2: Trigger efficiency for the single muon trigger in (a) the barrel region and (b) the endcap region. [21] . . . . .	45
Figure 3.3: Efficiency of the single electron trigger over transverse energy ranges in the ATLAS detector [22]. . . . .	46
Figure 5.1: Diagram illustrating a displaced vertex. [23]. . . . .	58
Figure 6.1: Distributions of Lepton $p_T$ for (a) leading, (b) second, and (c) third leptons as well as (d) leading jet $p_T$ with preselection applied except the cuts on minimum $p_T$ thresholds shown which are 40 GeV for the leading lepton, 20 GeV for the second lepton, 10 GeV for the third lepton, or 40 GeV for the leading jet. There are minimum $p_T$ reconstruction thresholds for these objects which are 25 GeV for the leading lepton and leading jet, and 10 GeV for the second and third leptons. . . . .	66

Figure 6.2: Distributions of (a) number of jets, (b) number of $b$ -jets, (c) $m_T^W$ , (d) $E_T^{\text{miss}}$ . At least one jet is required at this level in all cases, but the cut on the variable shown is omitted in order to assess the full distribution. The distribution of the number of jets does not include the cut on the number of jets, the distribution of the number of $b$ -jets does not include the cut on the number of $b$ -jets, and the $m_T^W$ and $E_T^{\text{miss}}$ distributions do not contain the $E_T^{\text{miss}}$ or the notch cuts.	67
Figure 6.3: Distributions of (a) two-dimentional map of $m_T^W$ vs $E_T^{\text{miss}}$ for the signal, (b) two dimentional map of $m_T^W$ vs $E_T^{\text{miss}}$ for the data, and (c) invariant mass of the $Z$ boson. For both (a) and (b) the $E_T^{\text{miss}}$ cut and the notch cut are not applied and for (c) the $Z$ -boson mass window cut is not applied in order to show the full distribution.	68
Figure 6.4: Distributions of transverse momenta for (a) the leading lepton, (b) the second lepton, (c) the third lepton, and (d) the leading jet in the control region for $t\bar{t}$ .	71
Figure 6.5: Distributions of (a) jet multiplicity, (b) $b$ -jet multiplicity, (c) $m_T^W$ , and (d) $E_T^{\text{miss}}$ in the control region for $t\bar{t}$ .	72
Figure 6.6: Distributions of transverse momenta for (a) the leading lepton, (b) the second lepton, (c) the third lepton, and (d) the leading jet in the intermediate control region for Diboson and $Z+jets$ .	73
Figure 6.7: Distributions of (a) jet multiplicity, (b) $b$ -jet multiplicity, (c) $m_T^W$ , and (d) $E_T^{\text{miss}}$ in the intermediate control region for Diboson and $Z+jets$ .	74
Figure 6.8: Distributions of transverse momenta for (a) the leading lepton, (b) the second lepton, (c) the third lepton, and (d) the leading jet in the control region for Diboson.	75
Figure 6.9: Distributions of (a) jet multiplicity, (b) $b$ -jet multiplicity, (c) $m_T^W$ , and (d) $E_T^{\text{miss}}$ in the control region for Diboson.	76
Figure 6.10: Distributions of transverse momenta for (a) the leading lepton, (b) the second lepton, (c) the third lepton, and (d) the leading jet in the control region for $Z+jets$ .	77
Figure 6.11: Distributions of (a) jet multiplicity, (b) $b$ -jet multiplicity, (c) $m_T^W$ , and (d) $E_T^{\text{miss}}$ in the control region for $Z+jets$ .	78

Figure 6.12: Distributions of (a) $m_T^W$ which is required to be $> 50$ GeV, (b) the $\eta$ of the leading non b-tagged jet which is required to be $> 1.5$ , and (c) the $\Delta R$ between the $b$ -jet and leading non- $b$ -jetwhich is required to be $> 2.5$ . Each has the entire selection applied except the variable plotted to view the full distribution. . . . .	81
Figure 6.13: Distributions of transverse momenta for (a) the leading lepton, (b) the second lepton, (c) the third lepton, and (d) the leading jet in the signal region. . . . .	83
Figure 6.14: Distributions of (a) jet multiplicity, (b) $b$ -jet multiplicity, (c) $m_T^W$ , and (d) $E_T^{\text{miss}}$ in the signal region. . . . .	84
Figure 6.15: (a) Number of electrons and (b) number of muons. . . . .	85
Figure 6.16: Distributions of the top-quark polarization in the (a) Optimal basis and (b) the helicity basis, (c) the $W$ -boson helicity, and (d) the mass of the top quark. . . . .	86

# Chapter 1

## Introduction

If you have knowledge, let others light their candles in it. -Margaret Fuller

High energy physics is concerned with obtaining the most fundamental understanding of the universe. In practice this means categorizing all fundamental particles and their interactions in order to understand what the world is made of. Assorted scientific fields question what the world is made of in various detail. Chemistry asks which atoms and molecules comprise the things around us, nuclear physics investigates what makes up the nuclei of atoms and how nuclei are formed, and high energy physics studies what we currently think are the most fundamental particles in existence. In order to understand high energy physics we need a framework to describe the elementary particles and their interactions. This framework is referred to as the Standard Model (SM).

### 1.1 The Standard Model

The SM of high energy physics has been among the most successful theories of the past century. It has been tested again and again and has encountered few unexplained anomalies. It started as an effort to combine the fundamental forces we know into one overarching theory. Electricity and magnetism had been combined into electromagnetism long ago and in the last century the SM was developed. Electromagnetism was combined with weak interactions,

followed by the inclusion of the Higgs mechanism and strong interactions to form the SM we know today [24, 25, 26].

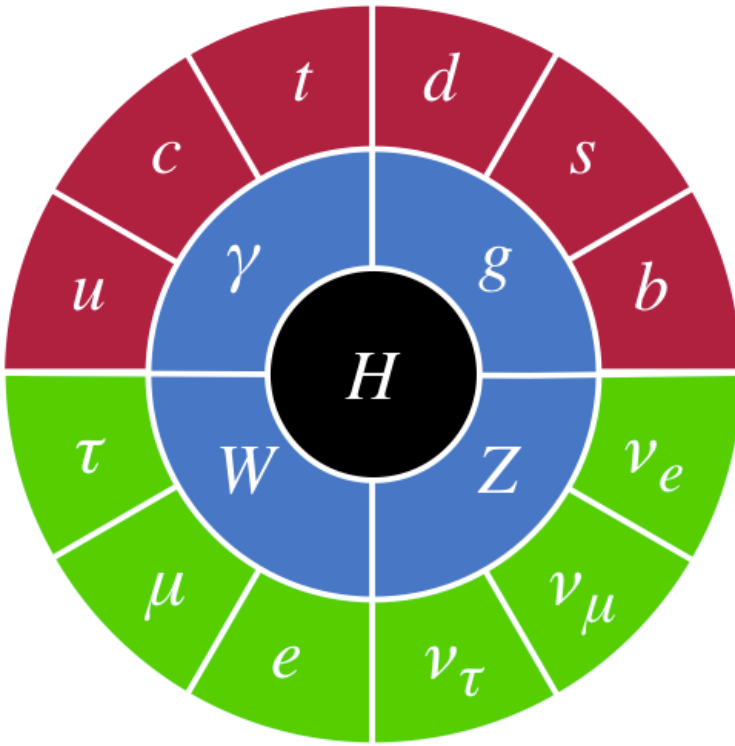


Figure 1.1: The SM of high energy physics [3].

The SM particles are classified based on their properties and interactions and are shown in Figure 1.1. One way we can classify particles is by their spin. A particle with half integer spin is called a fermion (colored red or green in Figure 1.1) while a particle with integer spin is a boson (colored blue or black in Figure 1.1). All discovered fundamental particles are either spin 0, spin  $\frac{1}{2}$  or spin 1. We further break down the fermions into two categories, the first set are the leptons which have an electric charge  $\pm 1$  (electron, muon, and tau) to interact with the electroweak force, and three neutral neutrinos which only interact via the weak force. The other type of fermion is the quark. Quarks interact via the weak, electromagnetic, and strong forces carrying half integer spins,  $\pm \frac{1}{3}$  or  $\pm \frac{2}{3}$  electrical charges, and color charges. The

strong force, at low energies, imparts color confinement onto individual quarks which binds them together in mesons (quark antiquark pairs) or baryons (three quark systems such as the proton or neutron). If quarks are high enough energy they undergo a process known as hadronization where new quark-antiquark pairs are created from that energy until all that remain are many mesons and baryons. Quarks also interact electromagnetically and weakly like their charged leptonic counterparts. The vector bosons (spin 1) moderate the forces involved in the Standard Model. The gluon interacts via the strong force, the photon and the  $W^\pm$  interact electromagnetically, and the  $W^\pm$  and  $Z$  bosons interact weakly. The final particle we have is the recently discovered Higgs boson [27] which took nearly 50 years to discover. A history of particle discovery can be seen in Figure 1.2.

A deeper understanding of the SM can be obtained through the Lagrange density [25],

$$\begin{aligned} \mathcal{L} = & -\frac{1}{2}tr[G_{\mu\nu}G^{\mu\nu}] - \frac{1}{2}tr[W_{\mu\nu}W^{\mu\nu}] - \frac{1}{4}B_{\mu\nu}B^{\mu\nu} \\ & + i\bar{\psi}[\not{D} - m]\psi + \bar{\psi}_i L y_{ij} \psi_j R \phi + h.c. + |D_\mu \phi|^2 - V(\phi) \end{aligned} \quad (1.1)$$

where  $\psi$  is the Dirac field with a sum over the matter particles with  $L$  denoting left-handed particles and  $R$  denoting right-handed particles,  $\phi$  is the Higgs field,  $y_{ij}$  are the Yukawa couplings,  $\not{D}$  is the covariant derivative defined through Dirac slash notation as

$$\not{D} = \gamma_\mu D^\mu \quad (1.2)$$

$$D^\mu = \partial^\mu - ig_S T^a G^{a\mu} - iY g_Y B^\mu - \frac{ig_L}{2} \sigma^a W^{a\mu} \quad (1.3)$$

where  $Y$  is the hypercharge of a particle. Hypercharge for left-handed particles are  $-\frac{1}{2}$  for

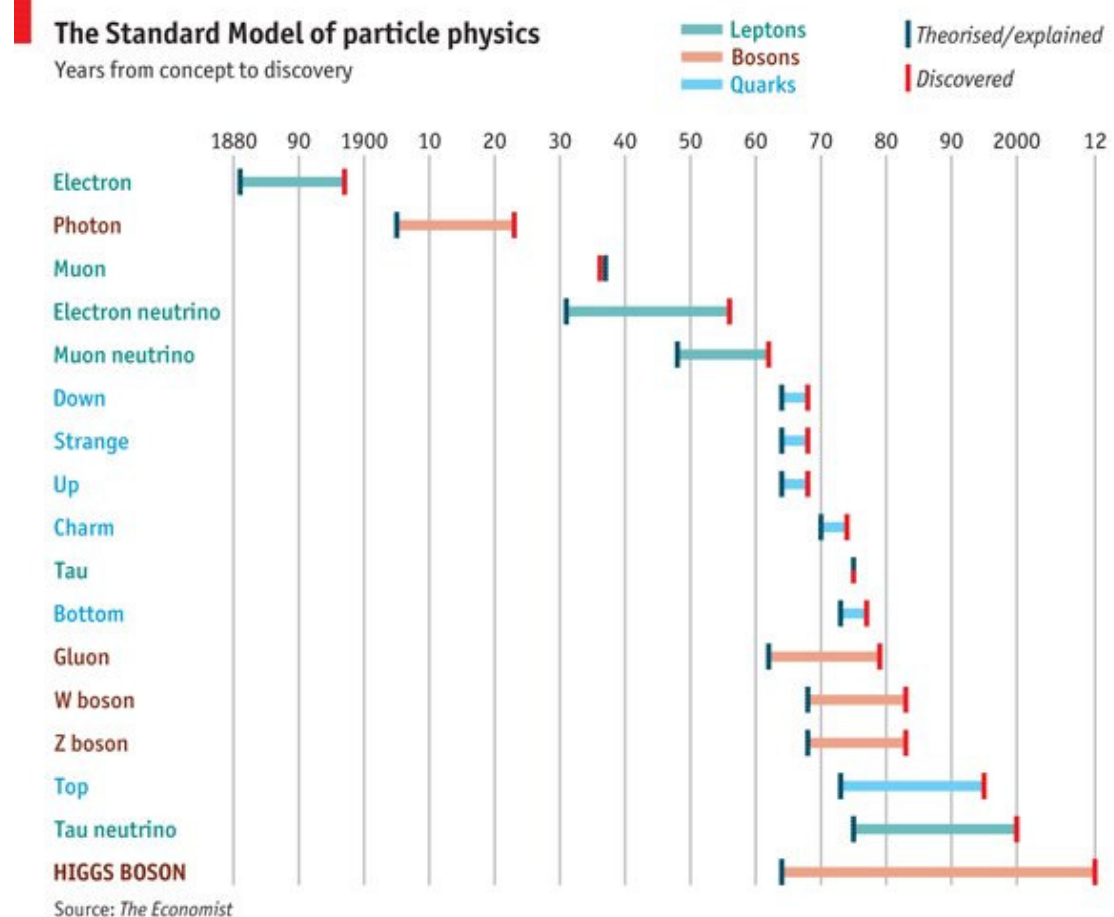


Figure 1.2: History of high energy physics illustrating the time it took from theorizing the existence of the particles until discovery [4].

leptons and  $\frac{1}{6}$  for quarks while for right-handed particles hypercharge is the electric charge of the particle. The tensor  $T^a$  is defined as half of  $\lambda_a$  (which are the 8 Gell Mann matrices) for quarks, and is zero for leptons. The  $\sigma_a$  matrices are the 3 Pauli matrices. The covariant derivative also applies to the Higgs boson, with  $T^a = 0$  (no coupling to strong force) and  $Y = -\frac{1}{2}$ . The gauge field strength tensor is denoted by  $B_{\mu\nu}$  and is defined by

$$B_{\mu\nu} = \frac{\partial B_\nu}{\partial \mu} - \frac{\partial B_\mu}{\partial \nu} \quad (1.4)$$

where  $B_\nu$  is the hypercharge gauge potential. The QCD field tensor  $G_{\mu\nu}$  defines the gluon fields and are defined as

$$G_{\mu\nu} = \frac{\lambda_a}{2} G_{\mu\nu}^a = \frac{i}{g_s} [D_\mu, D_\nu] \quad (1.5)$$

$$G_{\mu\nu}^a = \partial_\mu G_\nu^a - \partial_\nu G_\mu^a + g_s f^{abc} G_{\mu b} G_{\nu c} \quad (1.6)$$

where  $G_\nu$  is the strong gauge potential. The weak tensor  $W_{\mu\nu}$  is defined as

$$W_{\mu\nu} = \frac{\sigma_a}{2} W_{\mu\nu}^a = \frac{i}{g} [D_\mu, D_\nu] \quad (1.7)$$

$$W_{\mu\nu}^a = \partial_\mu W_\nu^a - \partial_\nu W_\mu^a + g f^{abc} W_{\mu b} W_{\nu c} \quad (1.8)$$

where  $W_\nu$  is the weak gauge potential. Note that the  $W^{a\mu}$  term in equation 1.3 only couples to left-handed particles.

The SM Lagrangian in equation 1.1 contains a lot of information on the SM in one concise equation. The first three terms in the Lagrange density formula contains the strong and electroweak forces, the fourth term describes how the particles interact with these fields,

the fifth term and its Hermitian conjugate (*h.c.*) describes how the fermions get their masses (note the  $\phi$  dependence means that the Higgs contributes but does not determine the value of their masses), the next to last term describes how the Higgs gives mass to the bosons, and the final term is the Higgs potential [24, 25, 26].

This formulation represents a group with a  $SU(3) \times SU(2) \times U(1)$  symmetry. The  $SU(3)$  represents the strong force, with the threefold symmetry in color charge. The eight generators of this  $SU(3)$  symmetry correspond to the various color combinations of the gluon which can be mathematically represented by the Gell-Mann matrices. The  $SU(2) \times U(1)$  represents the electroweak force which unified electricity, magnetism, and the weak forces whose generators can be represented by the Pauli matrices. The Higgs mechanism breaks this symmetry and this phenomenon is known as electroweak symmetry breaking. By breaking this symmetry the massless electroweak bosons ( $W_1$ ,  $W_2$ ,  $W_3$ ), and the hypercharge boson ( $B$ ) are recombined as the massive  $W^+$ ,  $W^-$  (which are linear combinations of  $W_1$  and  $W_2$ ), the massive  $Z^0$  (which is a linear combination of  $W_3$  and  $B$ ) and the massless photon (which is a combination of  $W_3$  and  $B$  as well). The Higgs doublet has 4 degrees of freedom, three of which are consumed by the longitudinal components of the massive  $W^+$ ,  $W^-$ , and  $Z^0$ . The remaining degree of freedom is a neutral scalar particle, the Higgs boson [28, 29].

## 1.2 Feynman Diagrams

Thanks to Richard Feynman we can obtain an intuitive understanding of particles and their interactions through Feynman diagrams [25]. We can view these pictures as having direct correlation with the processes involved and even set up the relevant equations to compute the scattering amplitude of a particular process. In these diagrams we compact the spacial

dimensions into one vertical axis while time is represented on the horizontal axis.

The cross-section for a particular scattering process is defined as the ratio of number of particles scattered per unit time ( $dN(t)$ ) to number of particles passing through a defined area per unit time ( $n$ ), see equation 1.9.

$$d\sigma = dN(t)/n \quad (1.9)$$

$$N_{events} = \sigma \int L(t) dt \quad (1.10)$$

$$L(t) = \frac{n_1 n_2}{4\pi\sigma_x\sigma_y} \quad (1.11)$$

Informally this is how probable that process is to occur in each interaction. The standard unit for cross-section ( $\sigma$ ) is the Barn ( $10^{-24}$  cm $^2$ ) but we commonly use picobarn or femtobarn to describe cross-sections. Consequently we define the beam intensity, or luminosity ( $L$ ), in inverse picobarns or inverse femtobarns. That way we can easily calculate the expected number of events from equation 1.10. Luminosity can be calculated from the beam parameters of the accelerator by equation 1.11 where  $n_1$  and  $n_2$  are the number of particles in each beam, and  $\sigma_x$  and  $\sigma_y$  are the Gaussian RMS beam sizes in their respective directions [25].

### 1.3 Top Quark Physics

The top quark is of specific interest to high energy physics and in particular this thesis. It has a mass that makes it the heaviest fundamental particle that we know today, 173.2 GeV,

which is about the mass of a gold atom [30].

Due to the top quark's large natural width, which is defined as the probability per unit time that a particle decays, it is the only quark with an observed decay lifetime ( $10^{-25}$  s) shorter than the timescale for strong interactions ( $10^{-24}$  s) [31, 32, 33, 34].

Because of this, and that the CKM matrix element  $V_{tb}$  ( $V_{tb}$  corresponds to the strength of the top quark flavor changing to bottom quark through a weak decay) is approximately equal to 1, the top quark almost always decays into a  $W$  boson and a  $b$  quark before it hadronizes into a jet [35, 25].

The top quark was originally discovered through pair production at the Tevatron in 1995 [36, 37]. Later the production of a single top quark was discovered at the Tevatron [38, 39] and its width measured [32, 33, 34]. These production channels have also been investigated at the LHC [40, 41, 42, 43, 44].

There are three channels of single top quark physics that have been studied at the LHC. They are  $t$ -channel,  $s$ -channel, and associated production (also referred to as  $Wt$ -channel). The largest contribution to single top at the LHC is  $t$ -channel, followed by  $Wt$ -channel, with  $s$ -channel being the smallest of the three. Being the largest,  $t$ -channel was observed first and has been observed independent of the other single top-quark production modes [45].  $Wt$ -channel has also been observed in ATLAS [46] and CMS [47]. Cross-sections for the different single top-quark processes at a proton-proton collider with  $\sqrt{s} = 8$  TeV are given in Table ???. The center-of-mass energy is denoted as  $\sqrt{s}$  for the proton-proton collision. The LHC's high beam energies make gluons in the proton more prevalent than when compared to energetic quarks so a look into the initial states of these processes shown in Figures 1.3, 1.4, and 1.5 reveal the hierarchical nature of their cross-sections.

The  $t$ -channel process has an initial state of an energetic gluon as well as a light quark,

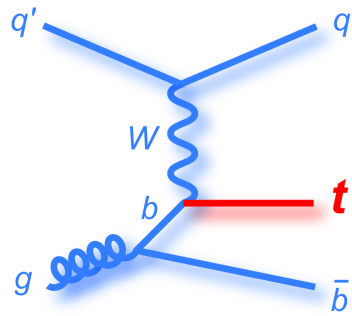


Figure 1.3: Representative Feynman diagram for the  $t$ -channel single top quark process [5].

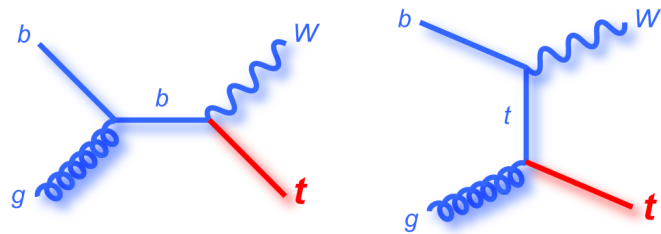


Figure 1.4: Representative Feynman diagrams for the  $Wt$ -channel single top quark process [5].

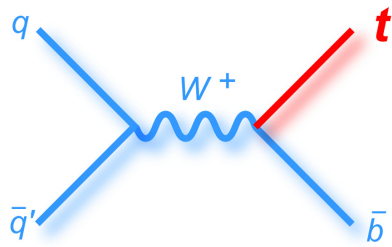


Figure 1.5: Representative Feynman diagram for the  $s$ -channel single top quark process [5].

$Wt$ -channel has an initial state of an energetic gluon as well as an energetic  $b$  quark (which will be harder to get from a proton when compared to a light quark which is naturally in a proton), and  $s$ -channel has an energetic antiquark in its initial state making it difficult to produce at the LHC. While  $s$ -channel has a comparatively small cross-section at the LHC it was not so disfavored at the Tevatron because the Tevatron was a proton anti-proton collider, making energetic anti-quarks more prevalent.

$t$ -channel	$216.99 +9.04 -7.71$ pb
$Wt$ -channel	$84.4 +5.00 -6.80$ pb
$s$ -channel	$10.32 +0.40 -0.36$ pb

Table 1.1: The cross-section for different modes of single top-quark production at the LHC at  $\sqrt{s} = 8$  TeV [1] [2].

## 1.4 tZ Associated Production

The production of a top quark in association with a  $Z$  boson has not been considered at the LHC until now. The Feynman diagram for  $tZ$  can be seen in Figure 1.6. The related  $t\bar{t}Z$  cross-section has been measured, and although the uncertainty is quite high, the top quark +  $Z$  boson processes are a potentially fruitful one to investigate [48]. The rate of the  $tZ$  process suggests that it should be visible in the 8 TeV data set as seen in Figure 1.7 which shows NLO cross-sections for the processes shown at various energies. The  $tZ$  signature investigated includes three charged leptons, missing transverse energy, and two jets, one of which may be identified as a  $b$  quark [7].

Several histograms can be seen in Figures 1.8 and 1.9 which show simulations of particles before any detector interaction or decays. Some notable features of  $tZ$  are the disparity between the  $\eta$  ( $\eta$  is defined in Section 2.3) of the light jet vs.  $b$  quark, the higher transverse

momentum ( $p_T$ ) of the light jet compared to the  $b$  quark, the similarity in  $p_T$  of leptons from the  $Z$  boson and  $W$  boson , and the  $p_T$  of the neutrino which will manifest as  $E_T^{\text{miss}}$ . The variable  $E_T^{\text{miss}}$  is discussed in more detail in Section 5.5.

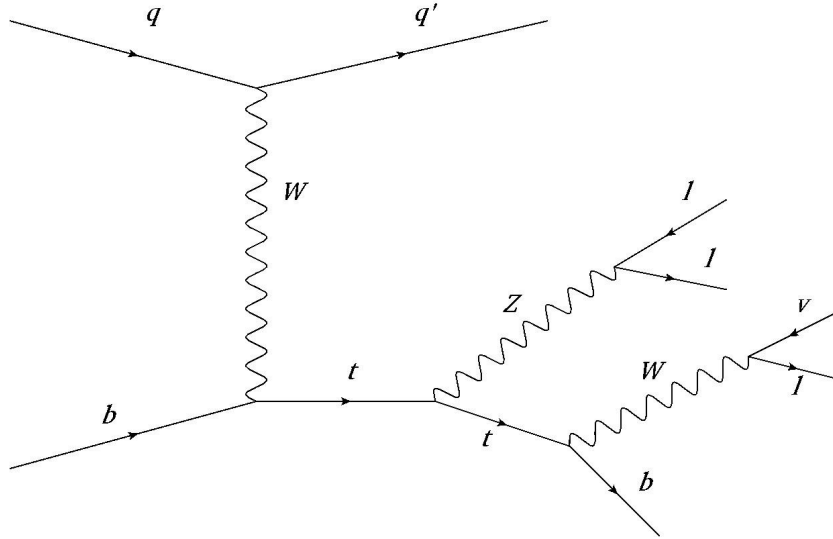


Figure 1.6: Representative Feynman diagram for the  $tZ$  associated production decaying to three leptons via a  $Z$  boson and a  $W$  boson [6].

Standard model  $tZ$  is important to measure because it is able to probe the coupling of the top quark with a  $Z$  boson [7]. Standard model  $tZ$  is also a background to several SM processes and Beyond the SM processes. Anomalous  $tZ$  couplings are one model that are of interest [49]. Monotop-quark production is one of these involving a top quark and large missing transverse energy coming from theorized dark mater candidates. Single top quark production in association with a Higgs boson is important to look for to probe the coupling of a Higgs boson to the top quark. One can also consider  $tZ$  as a background to Flavor Changing Neutral Current (FCNC) decays from  $t\bar{t}$  where one of the top quarks decays to a  $Z$  boson and a light quark which would enhance the cross section for this analysis.

For this analysis a cut and count method is used. By examining the kinematic properties

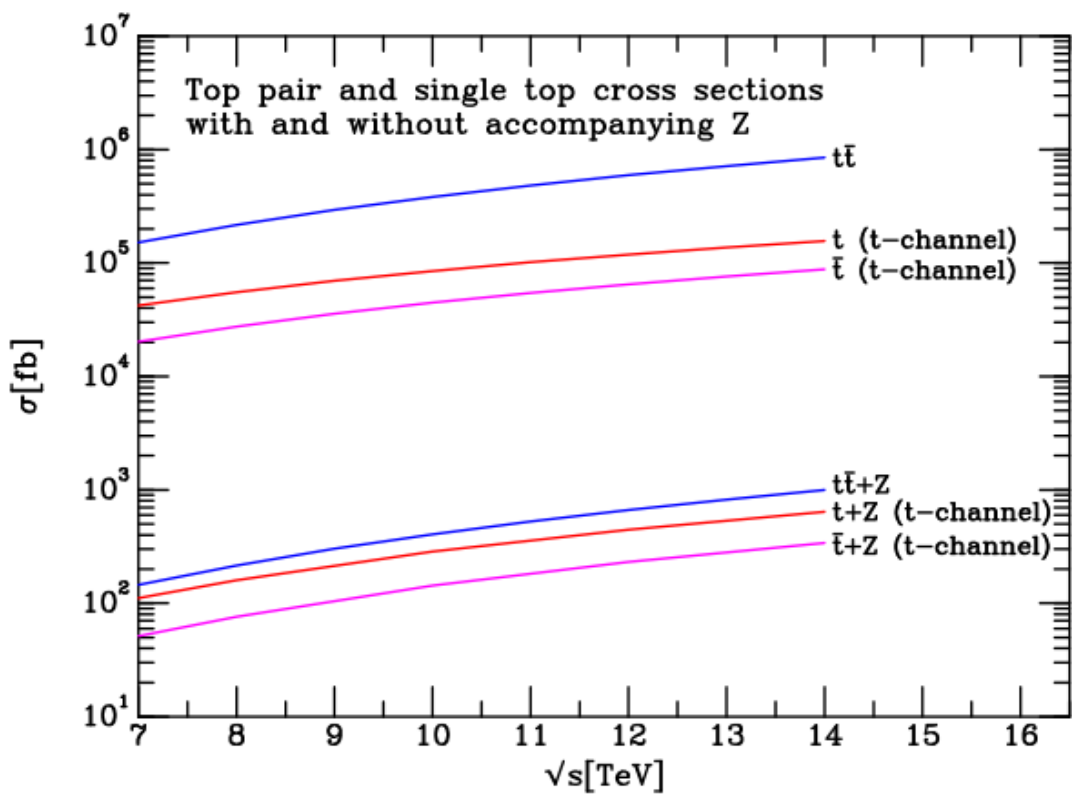


Figure 1.7: Top-Quark pair and single top quark cross-sections with and without accompanying  $Z$  boson [7].

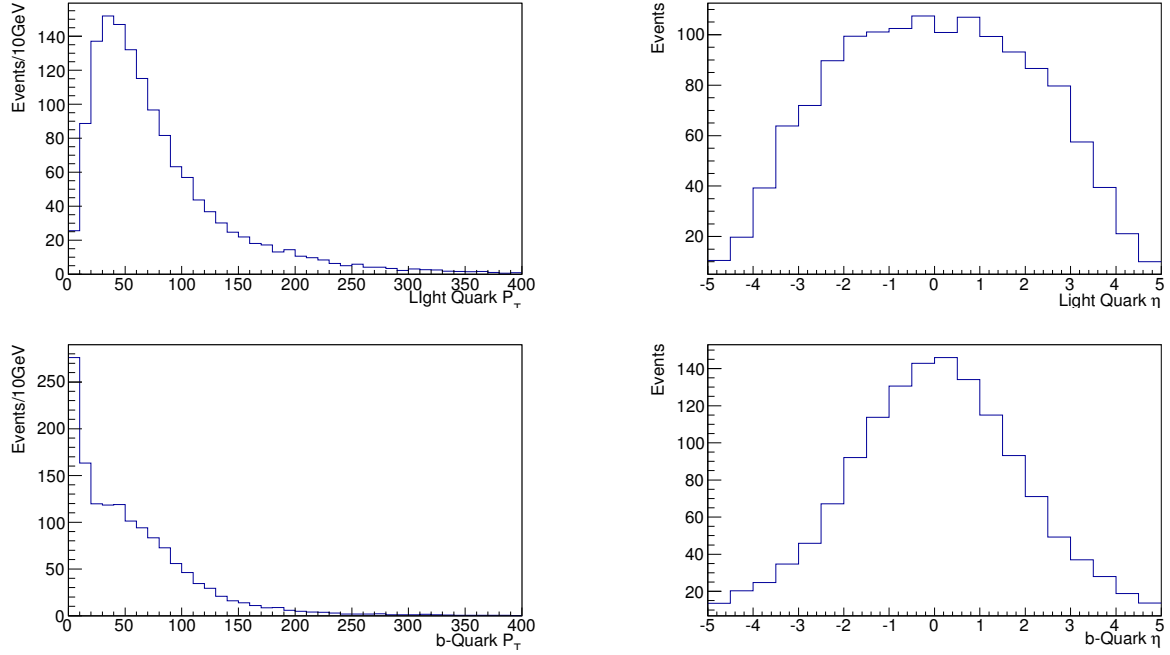


Figure 1.8: Information drawn from simulation of  $tZ$ . Light quark  $p_T$  and  $\eta$  as well as  $b$ -quark  $p_T$  and  $\eta$ . This simulation is described in detail in Section 4.2 with added simulation steps taken for a more complete analysis.

of the particles, as we have begun to do in Figures 1.8 and 1.9, regions of phase space can be created to isolate backgrounds to ensure proper data modeling through simulation as well as isolating the  $tZ$  signal to improve sensitivity for a statistical analysis.

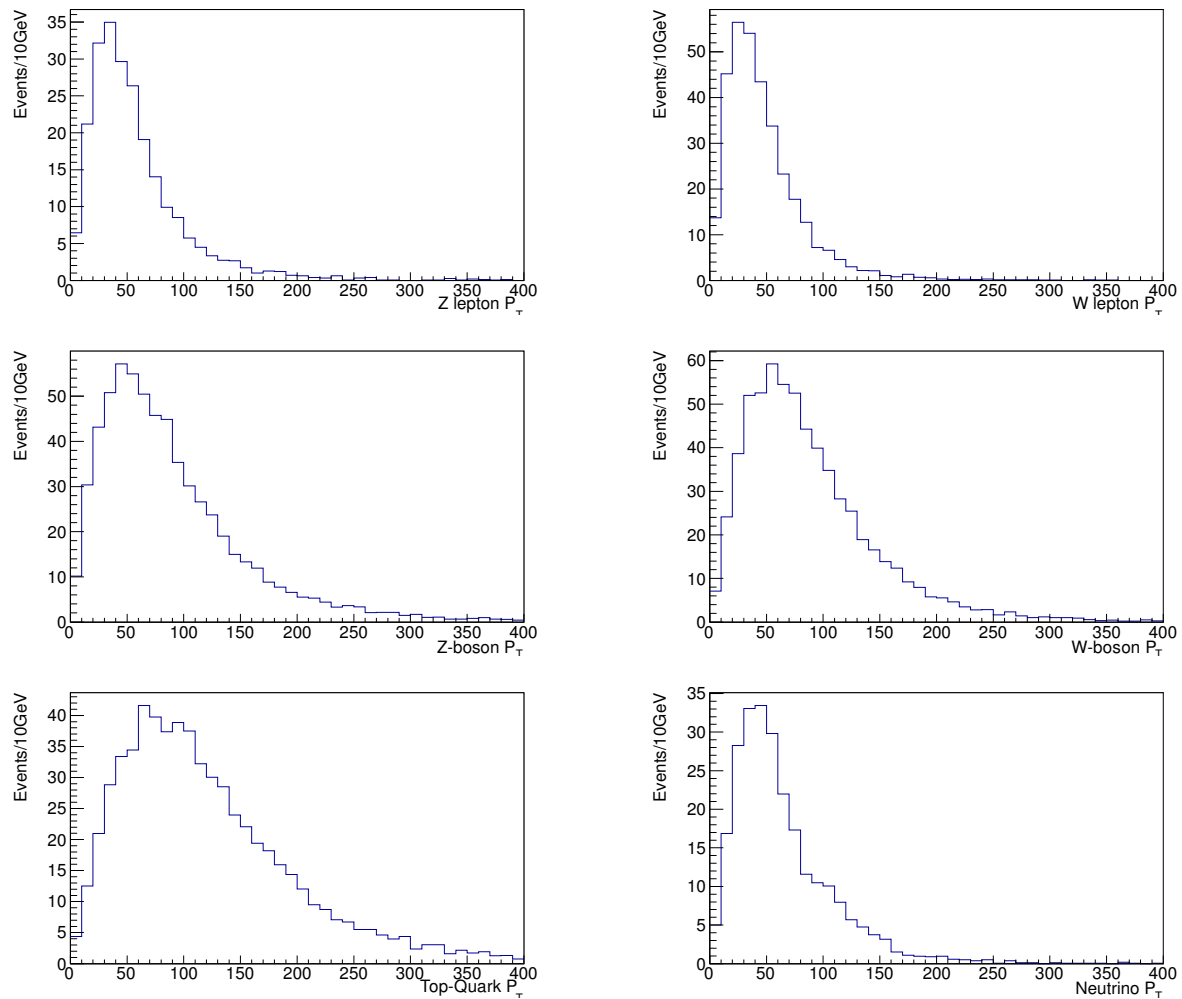


Figure 1.9: Information drawn from simulation of  $tZ$ . The  $p_T$  of other objects in  $tZ$  including the lepton from the decay of the  $Z$  boson and the lepton from the decay of the  $W$  boson. This simulation is described in detail in Section 4.2 with added simulation steps taken for a more complete analysis.

# Chapter 2

## CERN, the LHC, and ATLAS

When one tugs at a single thing in nature, he finds it attached to the rest of the world -John Muir.

In 1954 the Conseil Europen pour la Recherche Nuclaire (CERN) formed a nuclear physics laboratory just outside of Geneva, Switzerland. CERN has since delivered on their promise to give us dozens of experiments that study everything from meteorology to biology. Some of the labs accomplishments include: the discovery of the  $W$  boson [50] and  $Z$  boson [51]; the determination of the number of light neutrino families [52]; the creation of the world wide web [53]; the creation, isolation, and stabilization of anti-hydrogen for up to 15 minutes [54]; and the discovery of the Higgs boson [55, 56].

Over the past few decades CERN has focused on accelerator physics, housing the Large Electron-Positron Collider (LEP) [57] which ran from 1989 until 2000. LEP was then replaced with the Large Hadron Collider (LHC) [58] starting operations in 2009 after a faulty start in 2008 due to a failure in an electrical connection leading to a rupture of the liquid helium enclosure of one of the superconducting magnets. The LHC and LEP are often thought of hand in hand because they both used the same 27 km tunnel.

## 2.1 The Accelerator Chain

The LHC is capable of colliding protons as well as heavy ions, although we focus on the proton accelerator chain shown in Figure 2.1. The protons used in the LHC start from a hydrogen bottle where a magnetic field strips the electrons from  $H_2$  and the resulting protons are sent through linear accelerator 3 (Linac3). Linac3 uses radio-frequency cavities that charge cylindrical conductors which are alternately positively and negatively charged. The conductors directly behind the protons are positively charged while the conductors in front of the protons are negatively charged, with both working to accelerate the protons. Once the protons are through Linac3 they will be bunched with 100 ms bunch spacing and will be up to 50 MeV in energy [59]. From here they are sent through the 157 m circumference Proton Synchrotron Booster which accelerate the protons to an energy of 1.4 GeV in only 530 ms [60]. From there the protons go to the 628 m circumference Proton Synchrotron (PS) for tighter bunching of 25 ns, and are accelerated to 25 GeV [61]. The final step before the LHC is the Super Proton Synchrotron (SPS) which is 7 km in circumference. The SPS can accelerate protons to 450 GeV in 4.3 seconds [62]. The SPS is notable for the 1984 Nobel prize winning discovery of the  $W$  boson and  $Z$  boson [63].

Finally the protons make it to the LHC to be ramped up to the desired energy for collision. A segment of the LHC can be seen in Figure 2.2 which shows the housing for the magnets with the beam pipe located inside.

## 2.2 The Large Hadron Collider

It takes a few minutes to fill each LHC ring (one in each direction) forming the beams with thousands of bunches of protons which get accelerated together. After a 20 minute wait time

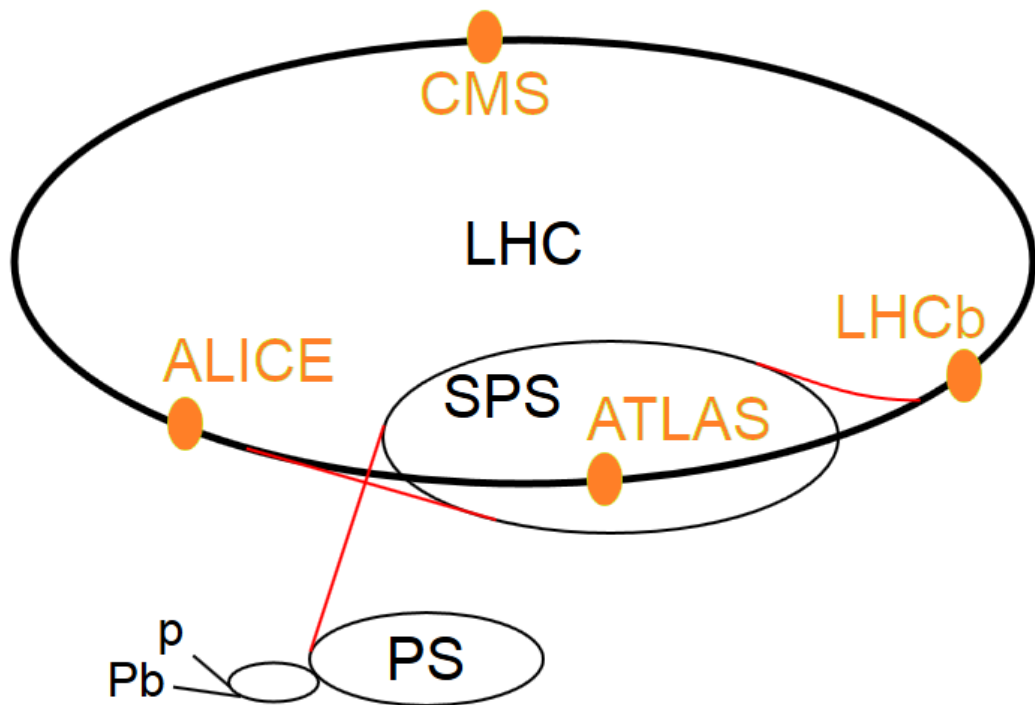


Figure 2.1: Diagram of the accelerator complex for protons to get to the LHC [8].

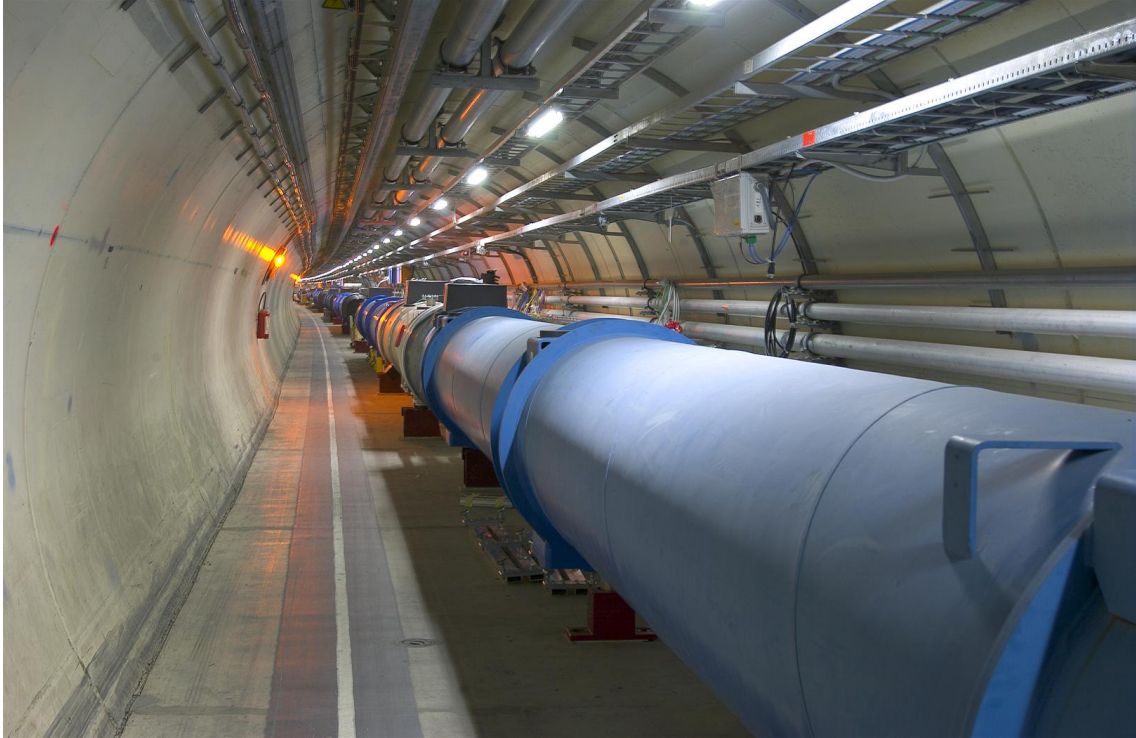


Figure 2.2: A Segment of the LHC beampipe [9].

after injection to stabilize and tighten the beams they are accelerated over half an hour to get up to full energy. In total it takes between 5 and 20 seconds to get the protons from Linac3 to the LHC, then a little less than an hour to get them up to energy. Once set up they can be stored for collisions for around 10 hours. The lifetime of the usable beam is limited mostly by protons in the beam exchanging momentum between the transverse and longitudinal directions. This is known as the Touschek effect [64]. Particles are lost from the beam if their longitudinal momentum deviation is great enough for them to escape the RF bucket (the longitudinal space that defines bunches) or the momentum aperture (the transverse space that defines how large a bunch can be in the transverse plane). After approximately 10 hours of beam collisions the beam is exhausted and is dumped and the injection process is repeated [65].

Given that the necessary conditions for the discovery of new physics were so extreme, the LHC was designed with unprecedeted capabilities. While most people think of the LHC as the highest energy collider in the world, which it is, there are more considerations when building an accelerator. In order to discover rare processes we consider instantaneous luminosity in order to collect as many interesting events as can be produced as quickly as possible. Peak ATLAS online luminosity is around  $5 * 10^{33} \text{ cm}^{-2} \text{ s}^{-1}$  (as seen in Figure 2.3) which is around 20 times the peak Tevatron luminosity [66, 67]. A greater instantaneous luminosity leads to a greater integrated luminosity, which is a measure of how much data has been collected over time, as seen in Figure 2.4 for previous the 7 TeV and 8 TeV run (Run 1) and Figure 2.5 for the 13 TeV run (run 2). As run 2 went on instantaneous luminosity was increased to maximize data collection showing the dramatic increase in data collection in August and September [10]. The generic term luminosity will usually refer to integrated luminosity in this thesis unless otherwise stated.

In order to keep the beams on track and together, the LHC has 1232 dipole magnets to steer the beam and 392 quadrupole magnets for focusing and a total of around 9600 superconducting magnets. The beams are segmented into 2808 buckets which can be filled with bunches of protons or not. The LHC was designed to deliver bunches that are spaced so that the resulting collisions are 25 ns apart (corresponding to approximately 10 meters between bunches). In 2015 the LHC operated at 50 ns bunch spacing (leaving every other bucket empty) to help with pile up. Pile up is when two separate proton proton collisions are read in at the same time and can come in two forms. The first is out-of-time pile up and refers to two different bunch crossings interacting with the detector more quickly than the detectors response time. Running with 50ns bunch spacing helps with out-of-time pile up

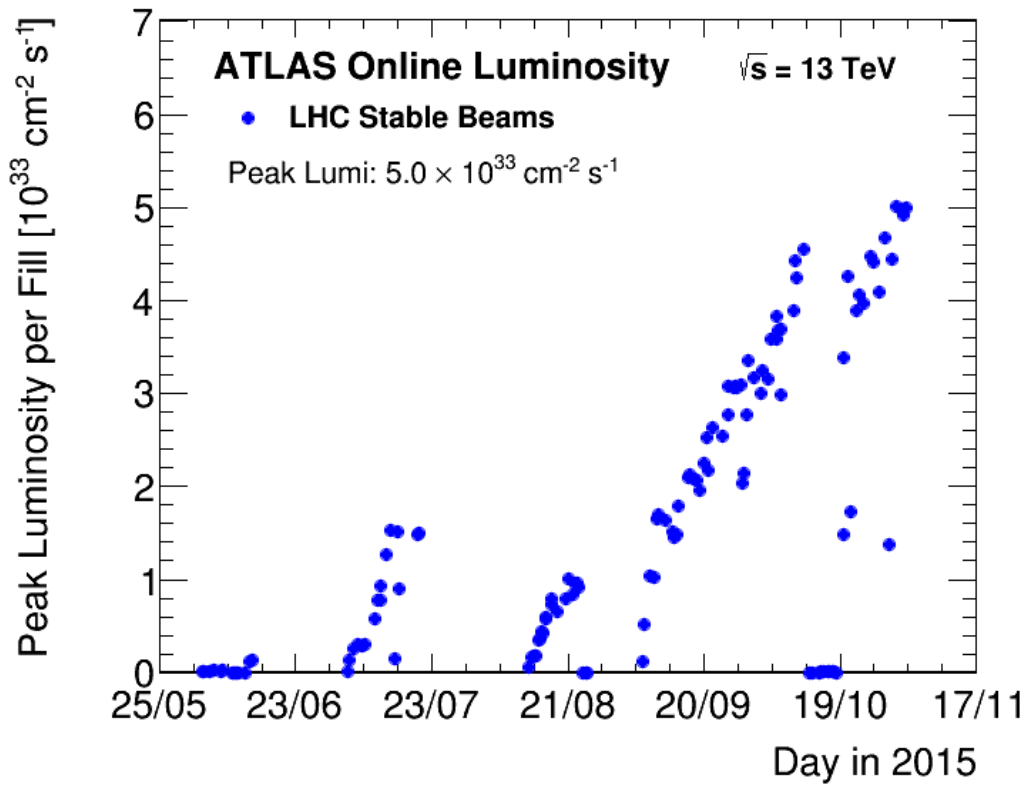


Figure 2.3: Peak instantaneous luminosity over time [10].

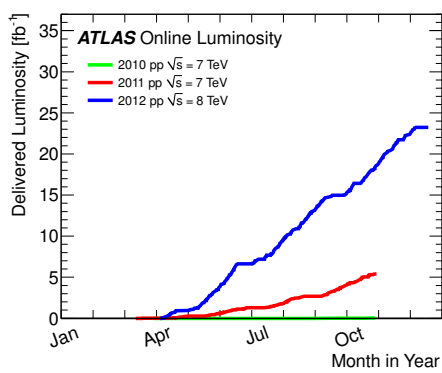


Figure 2.4: Total LHC delivered integrated luminosity over time for run 1 [10]

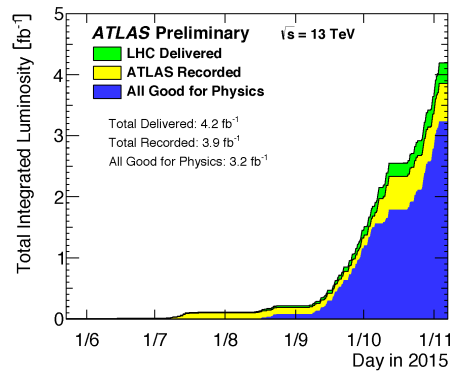


Figure 2.5: Total LHC delivered integrated luminosity over time for run 2 [10]

while running with 25ns bunch spacing helps with the other type of pile up, in-time pile up. In-time pile up is when two parton collisions happen within the same bunch crossing and both interact with the detector at the same time. Our data collection techniques are designed around some degree of pileup. Raising the pileup allows us to collect more data, potentially at the cost of data quality if it is not carefully monitored. With this in mind pile up was increased from the 7 TeV run with an average of 9.1 interactions per bunch crossing to the 8 TeV run with 20.7 interactions per bunch crossing as seen in Figure 2.6. In run 2 a more conservative 13.7 interactions per bunch crossing was used as seen in Figure 2.7. Pile up is an important consideration in triggering and is discussed in this capacity in chapter 3 [65].

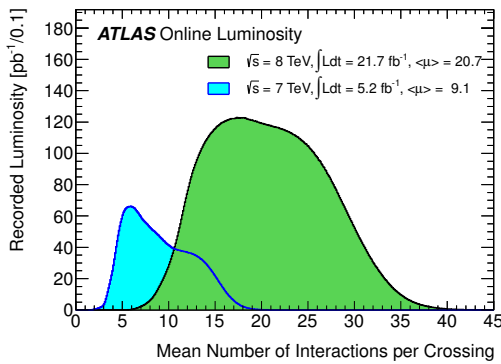


Figure 2.6: Number of interactions per bunch crossing for 7 and 8 TeV [10].

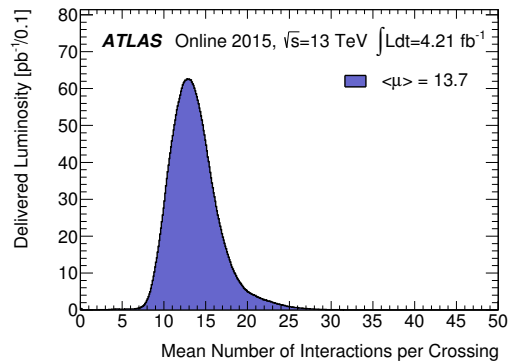


Figure 2.7: Number of interactions per bunch crossing for 13 TeV 2.6.

With an accelerator of this magnitude and a diversity of possible research topics, investigation through multiple experiments is merited. CMS [68] and ATLAS [69] are the largest general purpose detectors designed to search for the broadest range of possible new physics models and precision measurements. MoEDAL [70] searches for magnetic monopoles. TOTEM [71] and LHCf [72] are looking for forward particles and are positioned near CMS and ATLAS, respectively. ALICE [73] was specially designed to study heavy ion collisions

at the LHC to search for a state of matter known as quark-gluon plasma. LHCb [74] is an asymmetric detector studying the effects of matter antimatter asymmetry in proton-proton collisions.

With the LHC at such high energies and luminosities, the detectors had to be designed to be fast, radiation hard, and finely segmented all while maintaining a sensible budget.

## 2.3 ATLAS

A Large Toroidal LHC AparatuS (also known as ATLAS or the ATLAS detector) is among the largest and most complex particle detectors in the world and can be seen in Figure 2.8 with its namesake toroidal magnets in full view before much of the detector was added. A schematic view can be seen in Figure 2.9 It utilizes a multilayer design which has become ubiquitous in high energy physics. With this multilayer design comes a coordinate system that is vital to the design and use of the detector. There is a Cartesian coordinate system superimposed in ATLAS with the  $\hat{y}$  coordinate running vertically to the surface, the  $\hat{x}$  coordinate running toward the center of the LHC ring, and the  $\hat{z}$  coordinate running the length of ATLAS pointing in the counter clockwise direction around the LHC ring when viewed from above. There is also a spherical coordinate system defined with  $\phi$  running around the detector sweeping from the  $\hat{x}$  axis toward the  $\hat{y}$  axis while  $\theta$  runs away from the  $\hat{z}$  axis. While useful for construction and planning purposes, these variables are not as useful for analysis. A Lorentz invariant variable is desirable so particle properties in the detector can be measured in any reference frame. One is rapidity which is defined through energy ( $E$ ) and momentum ( $\vec{p}$ ) as

$$y = \frac{1}{2} \ln \left( \frac{E + p_z}{E - p_z} \right) \quad (2.1)$$

which has the unfortunate property of being dependent on the particle's mass. Another is the widely used pseudorapidity, defined as

$$\eta = \frac{1}{2} \ln \left( \frac{|\vec{p}| + p_z}{|\vec{p}| - p_z} \right) \quad (2.2)$$

which can be rewritten in terms of detector geometry variables as

$$\eta = -\ln \left( \tan \left( \frac{\theta}{2} \right) \right) \quad (2.3)$$

where  $\eta = \infty$  corresponds to the beamline.  $\eta$  is Lorentz invariant as long as  $m \ll E$  which is true in the low mass regime. In this regime pseudorapidity approximates rapidity. Pseudorapidity, therefore, has both the properties of describing detector geometry and describing particles in the detector that have boosts along the  $\hat{z}$  axis [14].

ATLAS can be segmented into several parts: the inner detector, the calorimeters, the muon spectrometer, and the magnets. Overall these systems are designed to work together to give measurements of particle energies as well as particle identification as diagrammed in Figure 2.10. An electron can be identified by tracks in the inner detector and a shower in the electromagnetic calorimeter, and it is distinguished from the photon which has no tracks in the inner detector. Jets get stopped in the hadronic instead of the electromagnetic calorimeter and muons will go all the way through the detector leaving hits in all detector elements. Many particles like the  $Z$  boson and top quark decay before reaching the detector. These objects must be reconstructed from their decay products. Neutrinos can be difficult

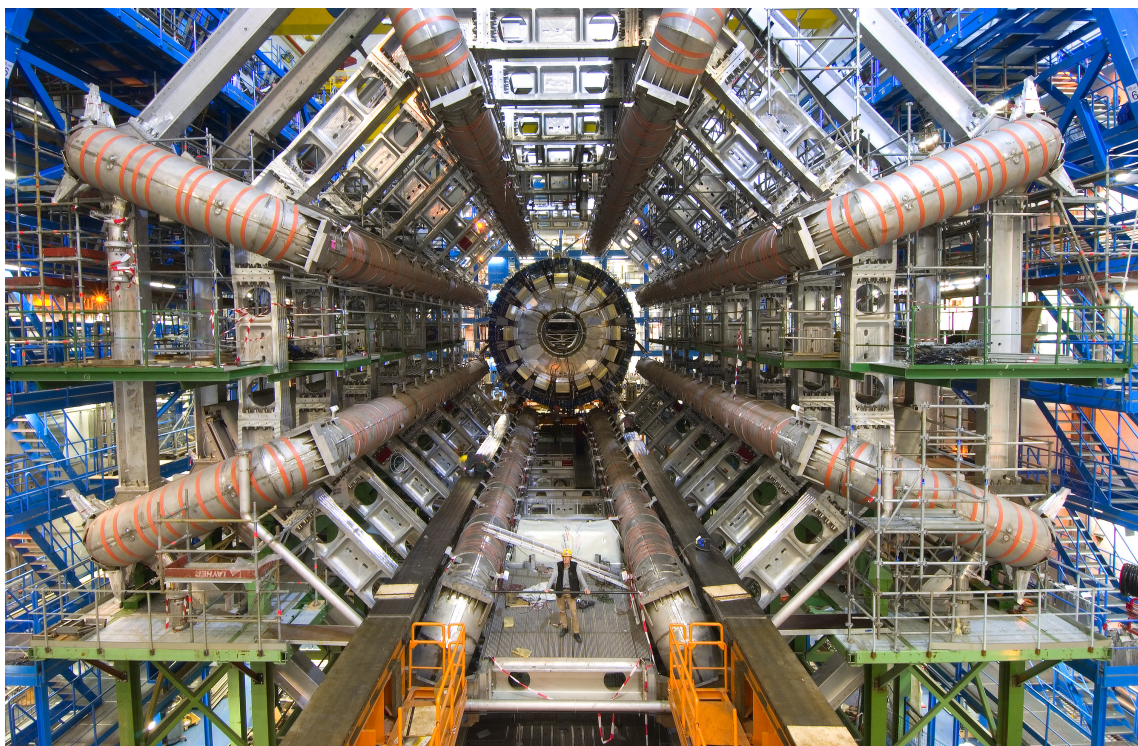


Figure 2.8: ATLAS with its namesake toroidal magnets prominently visible [11].

to reconstruct because they go through the entire detector without interacting at all. The object reconstruction is described in chapter 5 but for now we can take a deeper look into the subsystems of ATLAS.

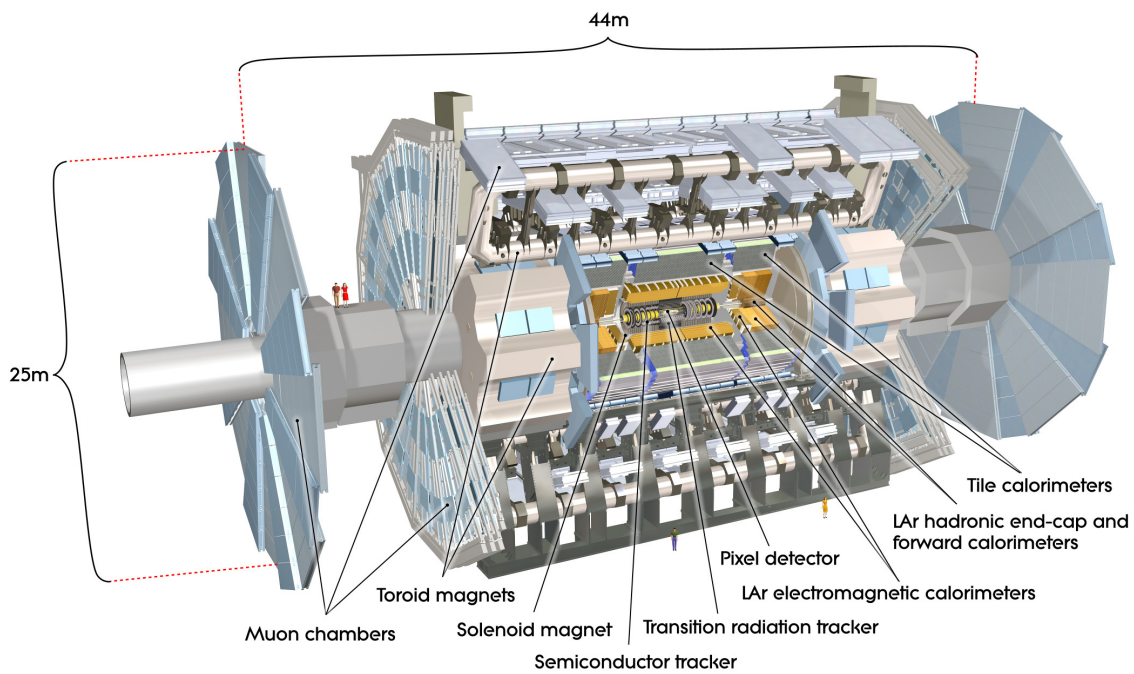


Figure 2.9: Cutaway diagram of ATLAS [12].

### 2.3.1 Magnet System

ATLAS has a magnet system designed to assist in particle identification by curving the path of charged particles through the detector systems. There are three parts to the magnet systems; the solenoidal magnet around the inner detector, the barrel toroids, and the endcap toroids. A schematic diagram of the layouts of these magnets can be seen in Figure 2.11. The magnetic field can be seen in Figure 2.12 which shows the inhomogeneous nature of the toroidal fields of the main toroids (positioned at approximately  $4.5 < R < 10$ ) and the

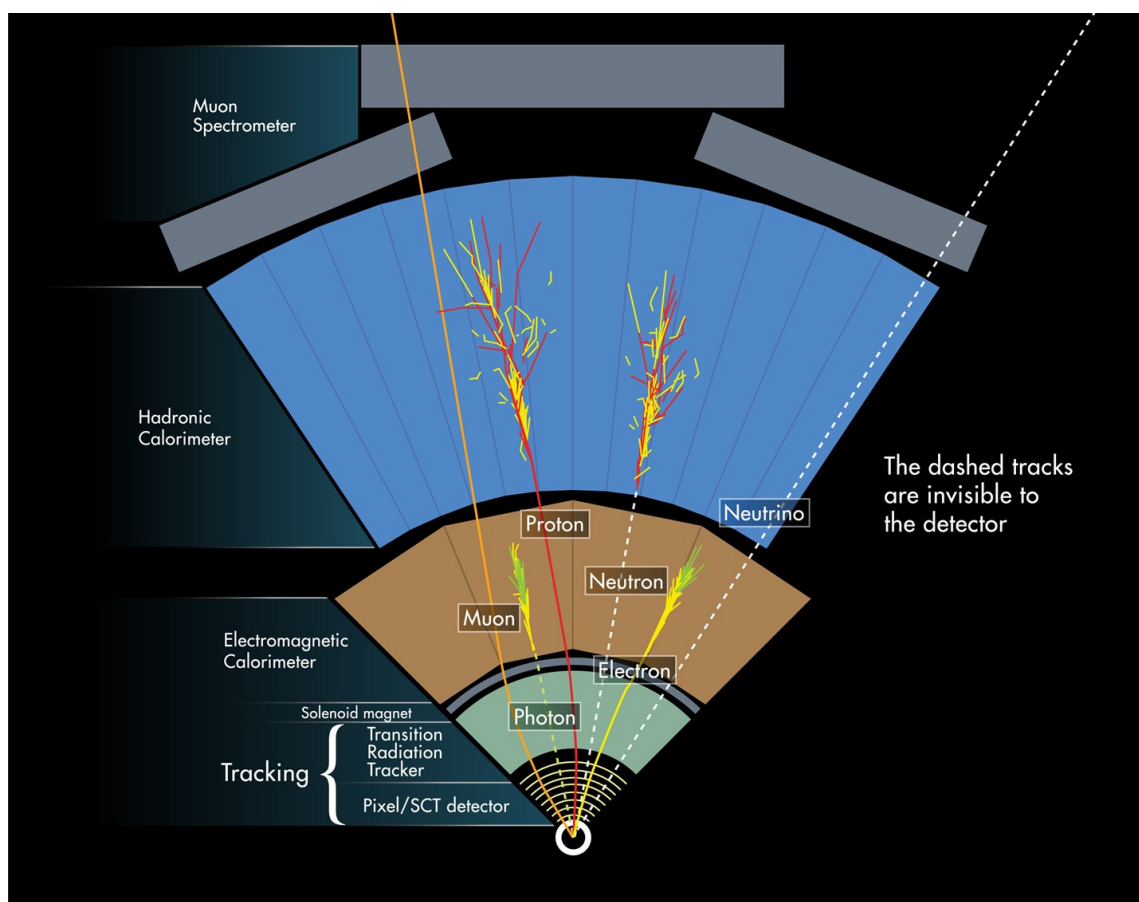


Figure 2.10: A figure diagramming how particle identification can be achieved using multiple layers of the detector [13].

endcap toroids (positioned at approximately  $R < 4.5$  and  $8 < z < 12$ ) and the comparative constant nature of the solenoidal field (positioned at approximately  $R < 1.5$  and  $z < 3$ ).

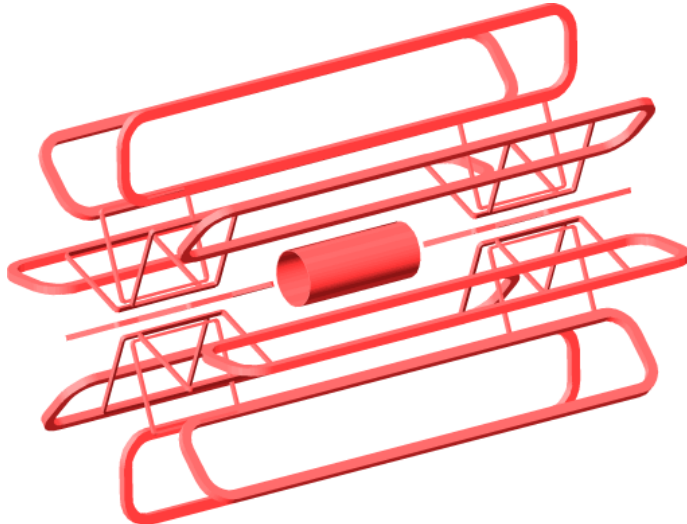


Figure 2.11: Illustration of the ATLAS magnet system, showing the barrel solenoid, barrel toroid, and endcap toroid coils [14].

The solenoidal magnet provides a nearly uniform 2 T magnetic field for the inner detector. The Solenoid is designed to be as thin as possible to minimize the interaction of the particles from physics events to aid in calorimetry. Any interaction in the solenoid will begin the showering process which means energy from the interacting particle will be lost and will have to be accounted for in calorimetry.

The eight barrel toroids are visible in Figure 2.8 and run  $\eta < 1.6$  providing a peak magnetic field of 3.9 T around the muon spectrometers and are highly irregular as seen in Figure 2.12. Because of this irregularity the magnetic field must be mapped carefully for accurate muon tracking.

The endcap toroids complete the ATLAS magnet systems providing a peak magnetic field of 4.1T for the forward detectors at  $1.4 < \eta < 2.7$ . The endcap magnets are offset from

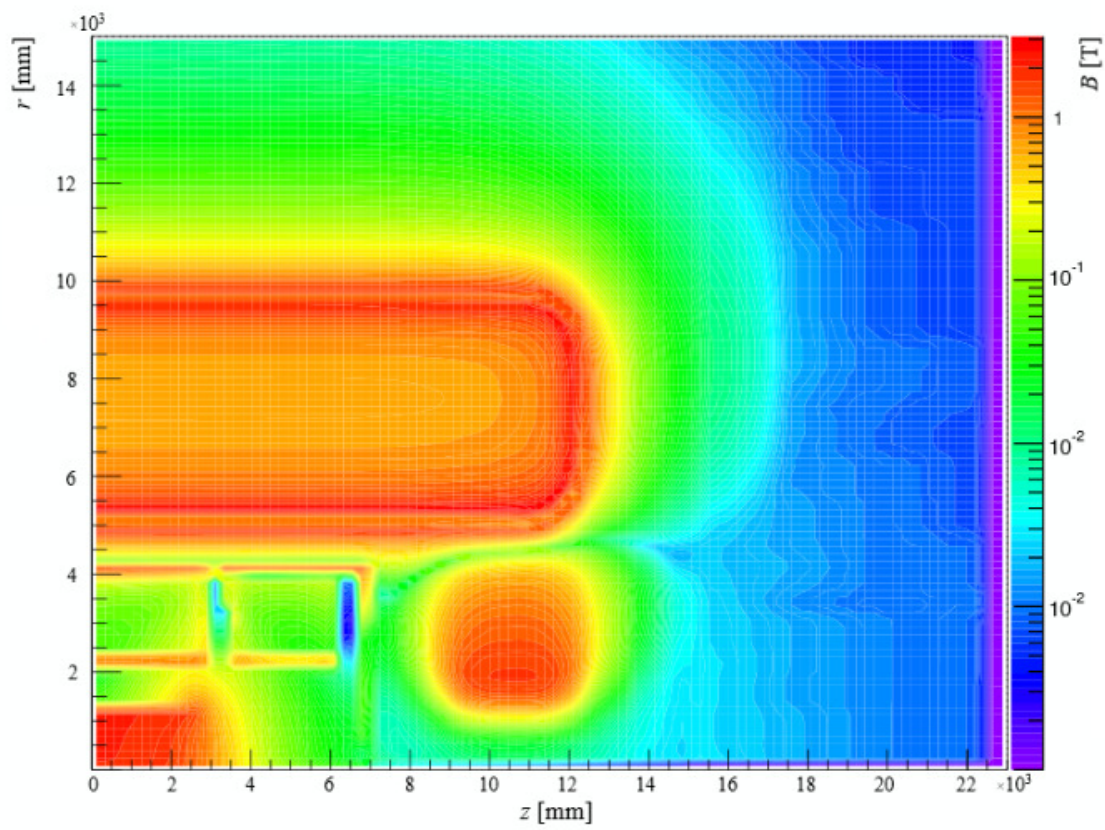


Figure 2.12: A mapping of the magnetic fields in ATLAS [15].

the barrel toroids by  $\frac{1}{16}$  of a turn so that they bisect the angle (in  $\phi$ ) between the barrel toroids seen in Figure 2.12.

These magnets are crucial for particle identification and momentum measurements of charged particles and are strategically placed around the detector subsystems described hereafter [75].

### 2.3.2 Inner Detector

The inner detector provides tracking information for tracked particles close to the beamline. Track reconstruction consists of finding sets of measurements coming from one charged particle and building the associated trajectory through the detector. In order to achieve this the inner detector was designed to be as hermetic as possible with high granularity as close to the beamline as possible [76, 77].

The inner detector has three parts and can be seen in its entirety in Figure 2.13. Those parts are the pixel detector, the SemiConducting Tracker (SCT), and the Transition Radiation Tracker (TRT) [78]. In May of 2014 another layer was inserted inside the ID known as the Insertable B Layer (IBL) for improved tracking closer to the interaction point.

The pixel detector and the SCT work on ionization of silicon which is separated into positive and negative charges which can be separated by an electric field into read out electronics. The read out can be either binary or non-binary. A binary read out registers a hit over some threshold or registers no hit. The non-binary readout registers the charge collected over time over some threshold and reports the amount of charge collected to assist in track reconstruction. Non-binary readouts give better tracks, but are more expensive and the read out electronics take up more space in the valuable real estate near the beamline. The pixel detector and SCT cover  $\eta < 2.5$  [79].

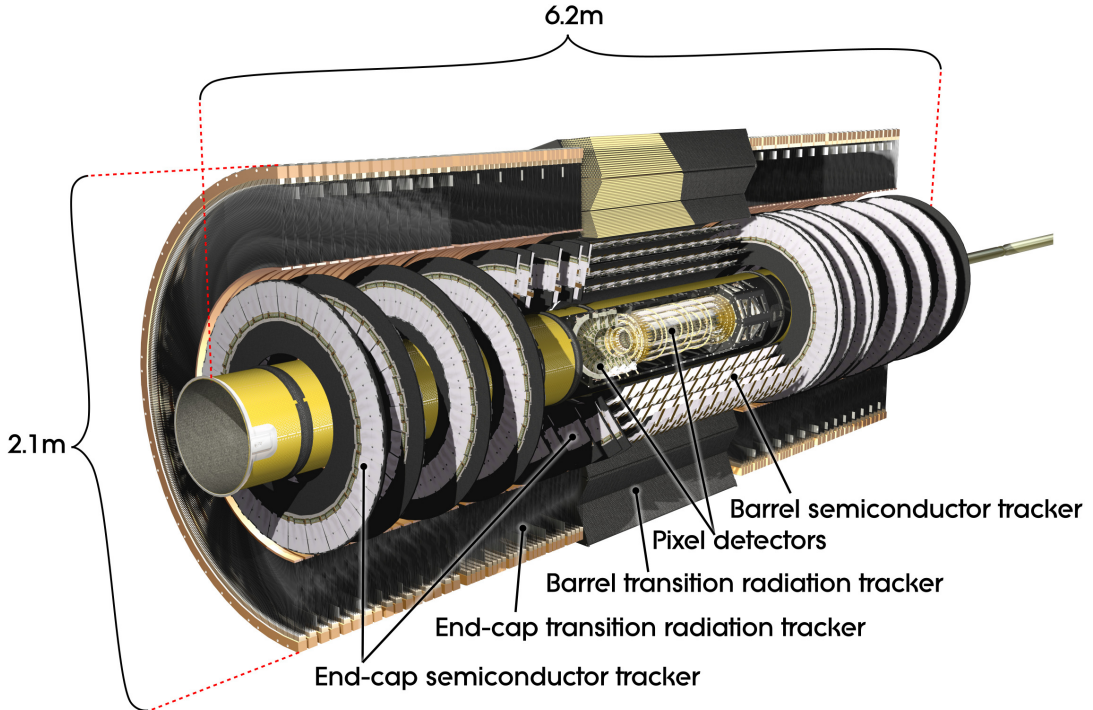


Figure 2.13: Cutaway diagram of the ATLAS inner detector [16].

The SCT strip detectors use a stereo-angle technique to get position measurements where concentric layers are constructed so a small angle of 40 mRad. Without an angle between layers of the strip detector only  $\phi$  could be read out, but with the angle  $\eta$  can be read out as well. By using strips of silicon a lot of money and space can be saved in comparison to pixel detectors, mostly in read out electronics, and there won't be as much supporting material in the way for the calorimeters [80, 81].

The TRT works on the principle of transition radiation. When a high energy particle goes between media with differing dielectric constants, the result will be the emission of radiation or as Jackson puts it “the fields must reorganize themselves as the particle approaches and passes through the interface. In this process, some pieces of the fields are shaken off as transition radiation” [82]. The TRT uses this by filling tubes with a gas of  $Xe$ ,  $CO_2$ , and  $O_2$

which is ionized by charged particles passing through. All charged particles will interact with the TRT giving tracking information, but the TRT has two separate thresholds for readout. The first threshold tracks charged particles while the second higher threshold determines if transition radiation is being detected. This occurs when a particle which is traveling faster than the speed of light in the medium it is entering, creating a sort of shock wave of radiation known as transition radiation. Because the electron participates in transition radiation more strongly than the pion we can obtain good pion rejection while maintaining electron reconstruction efficiency [83, 84, 85].

The largest source of track reconstruction inefficiency is hadronic interaction. When a hadron interacts with the nucleus of the detector material it is usually destroyed, and creates a hadronic and electromagnetic shower. The primary track stops when the original particle undergoes this process and a series of other tracks begin, but unfortunately the track can not be reconstructed. Another problem is electron bremsstrahlung. When a charged particle passes near the nucleus of the detector material it will radiate, loosing energy. This affects electrons more than other particles because the energy loss as it traverses the detector is proportional to energy over mass squared so the light electron will undergo bremsstrahlung more strongly than its heavier counterparts. Another consideration in tracking is multiple scattering which can cause a random change in direction not caused by curvature in the magnetic field. The method of detection can actually be a problem as well because when the particle ionizes the atoms of the detector it loses energy [15]. Even with these effects the track reconstruction efficiency is quite good varying from 90% in the central regions to 80% in the forward regions shown in Figure 2.14 [17].

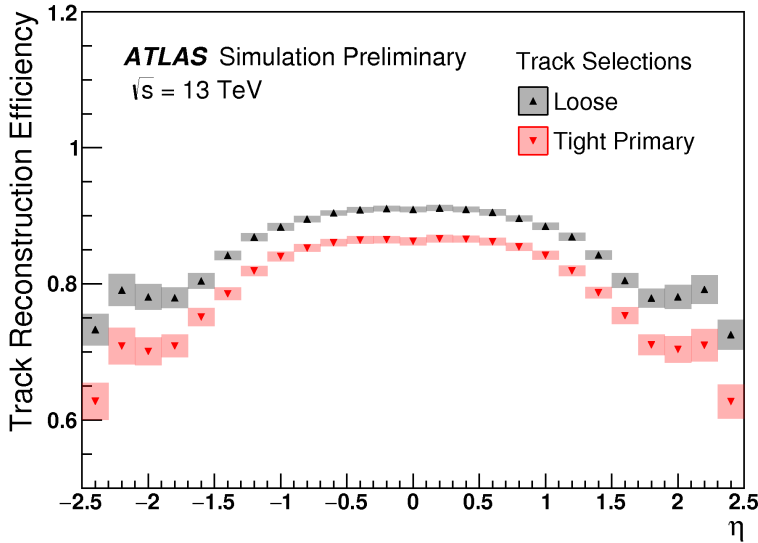


Figure 2.14: Track reconstruction efficiencies for the ID in ATLAS [17].

### 2.3.3 Calorimeters

There are two calorimeter systems for detecting electromagnetically interacting particles and strongly interacting particles referred to as the electromagnetic calorimeter, and hadronic calorimeter respectively, as seen in Figure 2.15. One high energy particle from the hard interaction of an event will shower into many particles creating a wave of energy deposition in the calorimeters. This process is particularly useful for neutral particles that can not be tracked in the inner detector, but is also useful for a more complete picture of a particular object.

Both the electromagnetic and hadronic calorimeters are sensitive to several different types of interactions. The first is radiative interactions where the incoming particle will scatter off a constituent atom creating a Rutherford scattering. They can also Compton scatter off atomic electrons, ionize the atoms of the detector, or have other similar low momentum transfers. After this, particle energies fall to when they are absorbed by atomic interactions

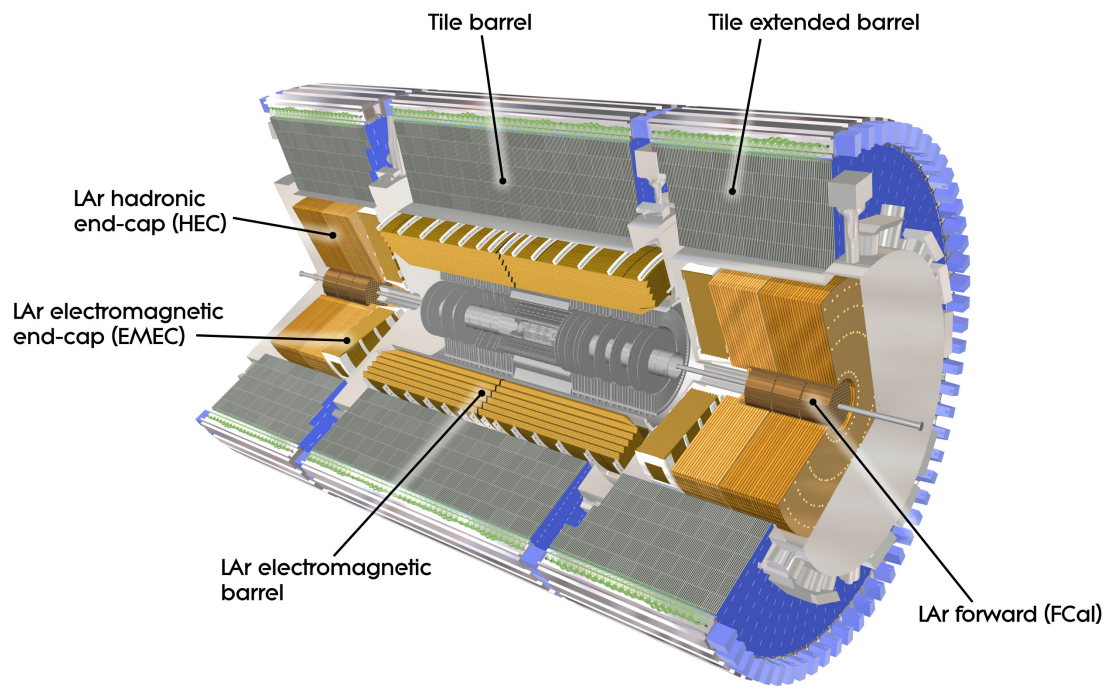


Figure 2.15: Cutaway diagram of the ATLAS calorimeter systems [18].

and the number of particles in the shower begins to fall. It is often noted that muons and protons are minimally ionizing in the electromagnetic calorimeters. This is because the radiative interactions which begin the particle cascade fall by  $m^2$ , so their large mass relative to the electron gets them through the electromagnetic calorimeter [86].

The Liquid Argon (LAr) calorimeters use sampling calorimetry. Because the primary interactions are radiative in nature, it is desirable to have high atomic number in the calorimeter material. The principal of sampling calorimetry is to have two materials in the calorimeter; one to facilitate the radiative interaction and begin the showering process, and another to detect the lower energy interactions that provide the signal that is read out. The LAr calorimeter is accordion shaped lead coated with stainless steel for radiative interactions with liquid argon to collect the resulting shower. The accordion shape is useful to increase the path length of particles in the material, thereby increasing the probability of an interaction and lowering the total amount of material needed. Wires in the liquid argon are held at high voltage to attract the ionized particles and read out the resulting current [86].

Tile calorimeters (TileCal) are placed outside the LAr calorimeters. They work on the same principles as the LAr calorimeters. The sampler for the TileCal is sheet steel without the accordion shape, and the readout material is a collection of plastic scintillators that emit light when hit with the resulting shower. The plastic scintillators are coupled to optical wavelength shifting fibers to redirect light to photomultiplier tubes. The light emitted from the scintillating plastic is typically in the UV range, and is shifted into the blue or green visible wavelengths to help limit attenuation while propagating [87] [88].

The geometry of the calorimeter systems are complex, but a simplified version is given here and can be seen in Figure 2.15. The barrel region of the detector (with  $\eta < 1.475$ ) has both LAr calorimetry and TileCal [89]. The endcap calorimeters cover  $1.375 < \eta < 3.2$

[90]. There is also a LAr forward calorimeter (FCal) that covers the extremely forward region  $3.1 < \eta < 4.9$  with a copper absorber for the electromagnetic portion and a tungsten absorber for the hadronic part. There is also an inner presampler to catch how intensively radiative interactions from interactions with the inner detector took place [91].

This gives an overall energy resolution of the electromagnetic calorimeter of less than 1% [92]. The energy resolution of the hadronic calorimeter is significantly worse, with calibrations from dijet events showing variations of 2-4% [93] but in practice this evaluation is a large source of systematic uncertainties to analysis. Energy resolution effects are described in more detail in Section 7.1.

### 2.3.4 Muon Systems

Muons provide an interesting challenge because they do not interact strongly with the electromagnetic or hadronic calorimeters and pass through the detector. The muon systems have four layers as shown in Figure 2.16; they are the Monitored Drift Tubes (MDT), the Cathode Strip Chambers (CSC), the Resistive Plate Chambers (RPC) and the Thin Gap Chambers (TGC).

The MDT provide most of the precision muon tracking in ATLAS. The MDT have a barrel and endcap section. The barrel section covers  $\eta < 1.0$  while the endcaps cover  $1.0 < \eta < 2.7$ . The MDT works on ionizing gases and is composed of straw tubes filled with gas which is composed of argon, nitrogen, and methane. The muon traverses the straw tube and ionizes the gas and the resulting charged particles are collected on a wire in the center of the tube which is held at high voltage. The amount of time it takes from the first current to reach the center wire until the last current reaches the center wire tells us how far away the muon came to the center of the tube. With this information we can make measurements on the

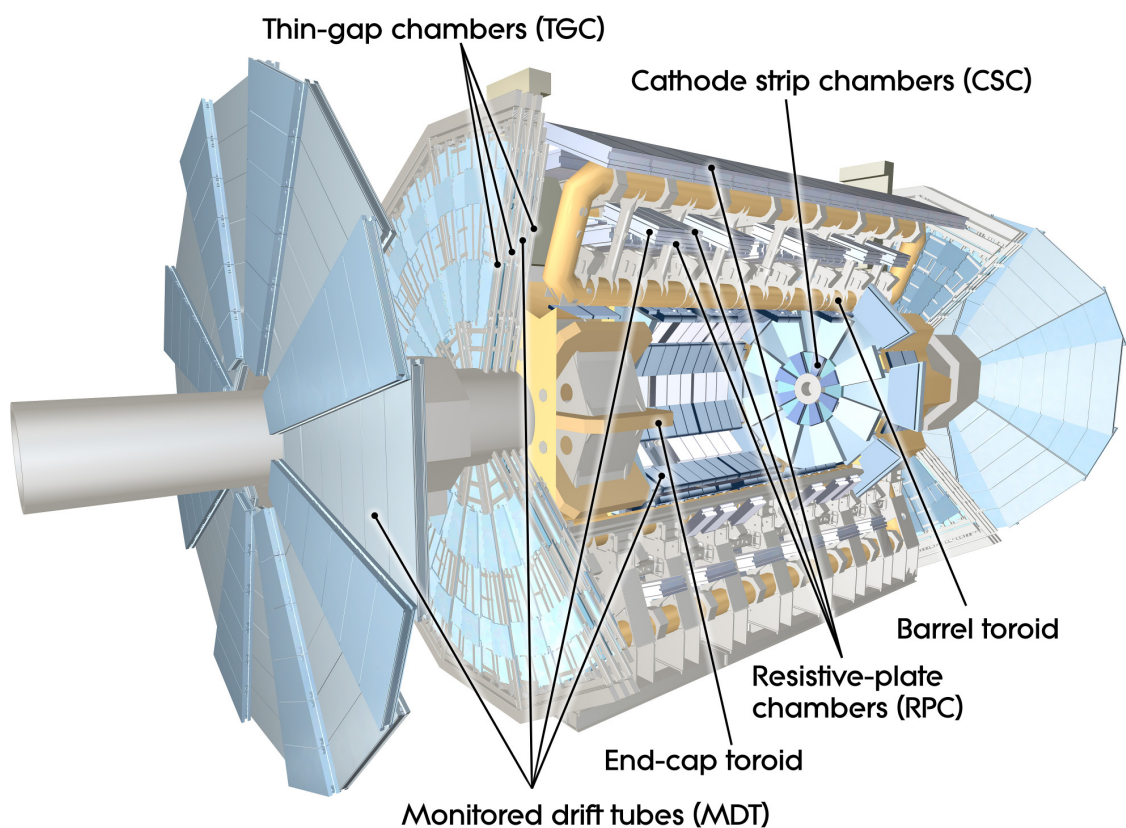


Figure 2.16: Cutaway diagram of the ATLAS muon spectrometer and toroid magnet systems [19].

path of the muon.

The CSC are multiwire proportional chambers used in high radiation zones around AT-LAS at  $2.0 < \eta < 2.7$ . They work on the same principles as the MDT, but with a different gas mixture.

The RPC are designed to supplement the MDT in the barrel region  $\eta < 1.05$  and has a fairly simple design. Each RPC chamber is two resistive plates held at 8900 V across a 2 mm gap. An incoming charged particle ionizes the gas and cause a localized discharge of the capacitor. The location of this discharge can then be read out. This method does not give very good spacial resolution (approximately 1 cm) but is quite fast with a timing uncertainty of 1.5 ns. Due to this excellent timing resolution, the RPC are utilized primarily by the Level 1 trigger described in Section 3.1.

The TGC (as seen in Figure 2.17) are also designed to supplement the MDT but in the forward region of the detector  $1.05 < \eta < 2.4$ . It uses the same technology as the RPC and consequently is used for triggering as well. The TGC have a different gas mixture in order to decrease spacial resolution for bunch identification (down to 9 mm) but suffers in timing response (7 ns) which is still fast enough to be used by the level 1 trigger system [94, 69, 95].

Overall this system gives excellent momentum resolutions of less than 0.1% for momenta used in this analysis [69]. This is possible thanks to the fine segmentation and position resolution of the layers of the muon spectrometers containing over 1 million readout channels [96].

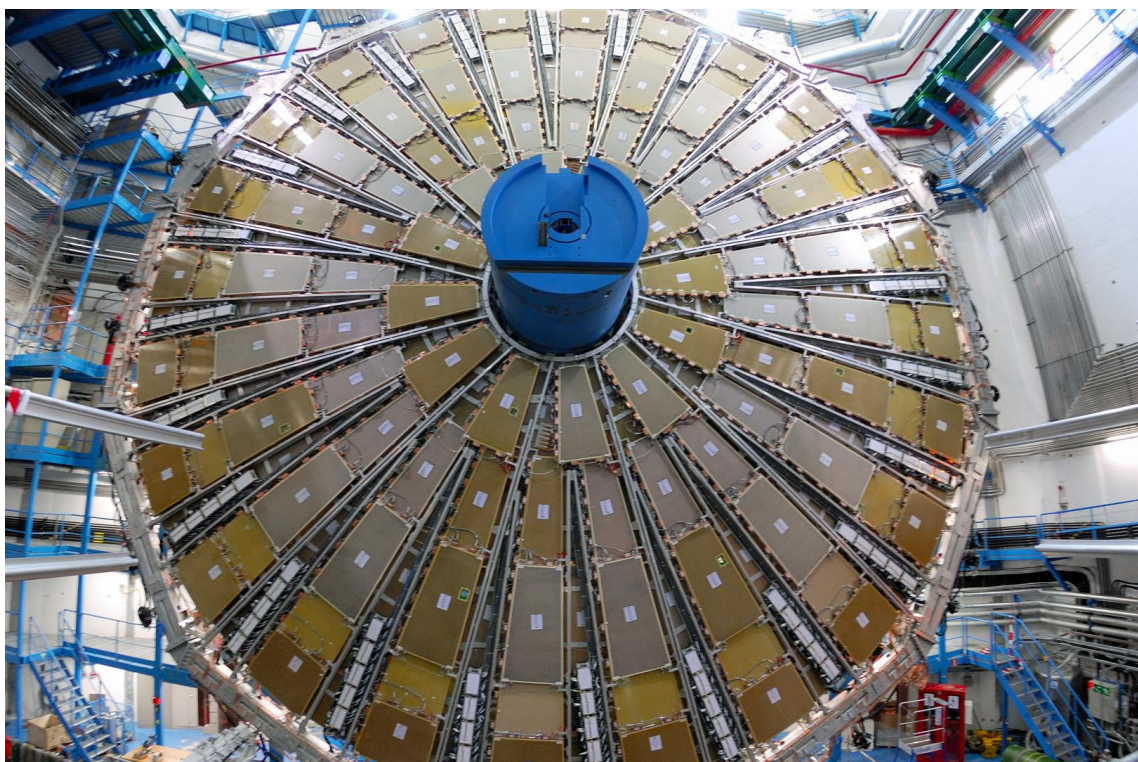


Figure 2.17: The TGC wheel [20].

# Chapter 3

## The Trigger System on ATLAS

Remember kids, the only difference between screwing around and science is writing it down.

-Adam Savage

Interaction rates in the ATLAS detector are staggering. Since we can not store information on every interaction we must filter it through the ATLAS trigger system and keep only events which have the prospects to contain interesting processes. There are three terms worth defining here. The trigger is the decision making process used by ATLAS to distinguish interesting events from non-interesting ones, data acquisition refers to the system that delivers and stores wanted events and variables, and data preparation which prepares saved data for analysis. The trigger is separated into three levels that start with hardware on the detector and get more computationally intensive as they progress. They are Level 1, Level 2, and Event Filter. A trigger chain is a set of trigger settings that can be designed around hardware responses, reconstructed objects, and reconstructed events. There are approximately 700 different trigger chains. With so many types of events to be seen we must limit the rate of any given trigger chain due to bandwidth considerations. Every proposed trigger chain is evaluated for efficiency, purity, overall rate, overlap rate with other trigger chains, response to pile up, response to increased luminosity, and its usability in many analysis or at least one well motivated analysis.

This system is designed with four main principles in mind:

1. Factorization and partitioning.
2. Minimization of data movement.
3. Uniformity and minimization of required developments.
4. Staging of data volumes and rates.

Partitioning of the trigger into relevant components is important so that various subsystems can run independently and concurrently. The capacity to run with only a fraction of the trigger chains is deemed important to be able to debug existing trigger chains as well as be able to commission new trigger chains. Minimizing data movement is key to keeping high rates of throughput with low latency. Uniformity allows adoption of common hardware that can be purchased more cheaply and replaced more easily. Staging the trigger into three levels is done in part to keep the trigger adaptable so as the physics environment changes the trigger can be adapted or expanded.

If problems arise with a trigger chain they can be dealt with in several ways. The first tool of evaluation of many triggers is the tag and probe method. In this method two objects can be selected from an event, one of which (known as the tag) is triggered on and will be given a tight requirement to ensure purity of a particular sample while the other (known as the probe) is taken to be tested on. An example is a  $Z$  boson going to two electrons with one electron being a tag while the other is a probe to test the efficiency of the single electron trigger chain. The Feynman diagram can be seen in Figure 3.1. The probe is then classified into three groups; passing the tag criteria, passing the probe criteria, or failing the probe criteria. Once we know how the electron failed we can take steps to correct the inefficiency. If the trigger rate is too high we will not be able to record events that pass the trigger. In

this case it is common to use prescales which reject a given percentage of events that would otherwise pass a trigger chain in order to make bandwidth for other trigger chains. Their use is often motivated by the generality or usefulness of the trigger chain and political will to keep events from that trigger chain.

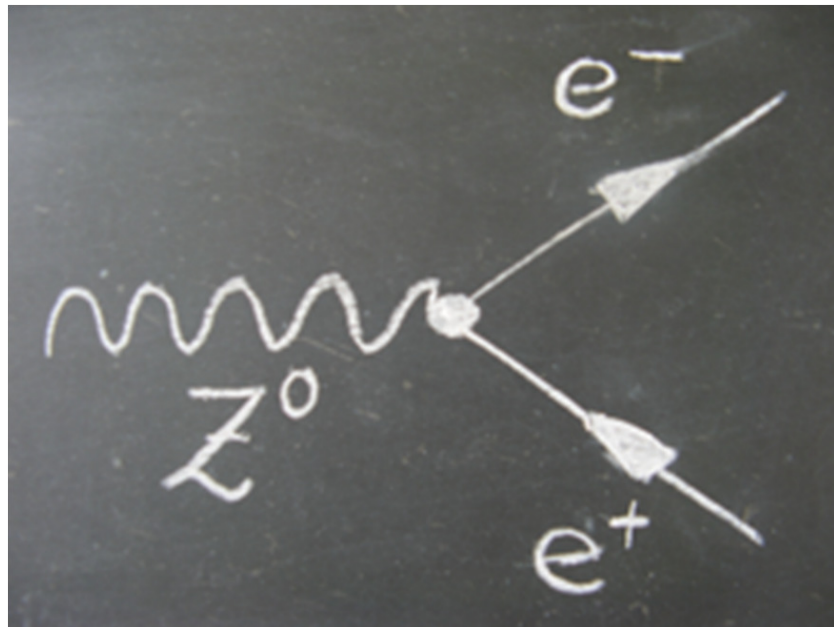


Figure 3.1: A  $Z$  boson decaying to an electron positron pair.

### 3.1 Level 1 Trigger and Data Acquisition (DAQ)

The Level 1 (L1) trigger and Data Acquisition (DAQ) systems are hardware-based and look at each segment of each subdetector individually to determine if the event should be passed. The L1 trigger is composed of several parts. L1Calo looks at the calorimeter deposits and their multiplicity while L1Muon looks at the muon systems in the same way. The L1 trigger works with front end analog-digital processing (the hookup to the actual detector). The front end processing has the L1 buffer which is used to store information for long enough

to accommodate L1 latency (described in the next paragraph), the derandomizing buffer where L1Accept signals are stored to be sent to the L2 trigger, buses for transmitting the front end data stream to the back end electronics. These hardware systems are crucial for the trigger to be able to function efficiently because they give the Central Trigger Processor (CTP) enough time to make the decisions on each event based on a premade trigger menu. The Trigger Timing Control (TTC) is responsible for ensuring that all individual detector readouts and systems in the trigger are synchronized and properly labeled by bunch crossing and interaction point, and the Region of Interest Builder (RoIB) which prepares accepted events for L2.

There are four main environmental considerations that influence the design of the front end readout electronics: radiation effects, magnetic fields, space around the detector for access, and the location of the service caverns housing the back end electronics. Radiation is a concern because, for example, read out electronics can be falsely triggered by radiation energy. Magnetic fields dictate the composition of components in the electronics especially in power supplies. Access is problematic in areas where there is a lot of detector material with little room for read out electronics such as the inner detector. The service caverns can house electronics without worries about radiation, and thus can house electronics that would otherwise be unavailable in the cavern. The types of links are then defined by the type of data being transmitted (analog or digital) as well as the speed it is transmitted through the length of the links which ranges from 50 to 150 meters [94, 95].

The L1 trigger takes the potential data rate from 20 MHz to 75 kHz in a latency of less than  $2.5 \mu\text{s}$  which includes propagation delays of the signal in the cables that get the information to the trigger logic circuit [94]. Latency is the time delay from detector response to the actual trigger decision. Because of the need for such low latency, L1 considers in-

formation on calorimetry and muon systems but not information on tracking because the reconstruction algorithms required are too slow [95].

## 3.2 High Level Trigger (HLT)

The HLT is the name given to the portion of the trigger that is largely software based. The HLT is software based and looks at Regions of Interest (RoI) passed to it by L1. These RoIs give more information to make decisions and are given more time to make those decisions. These ROI fragments must be merged into a single event which is a computationally slow process. Then the entire event as reconstructed by the event builder is investigated to decide if an event will get saved to the ATLAS Tier 0 data storage center.

## 3.3 Trigger Chains

A look at the final state of interest will inform what trigger chains are worth looking into. For  $tZ$  the final state of interest in Figure 1.6 has the  $Z$  boson decaying into two leptons; the top quark decaying to one lepton, one b-jet, and  $E_T^{\text{miss}}$ ; and one additional forward jet. Jets and  $E_T^{\text{miss}}$  are described in Chapter 5. This creates a situation where many different trigger chains can be utilized effectively. The samples used have a requirement that there either be  $\geq 2$  leptons (defined here as electrons or muons) with  $p_T > 15$  GeV and  $|\eta| < 2.5$  OR  $\geq 2$  leptons with  $p_T > 10$  GeV and  $\geq 1$  lepton with  $p_T > 20$  GeV which has  $|\eta| < 2.5$ . This requirement along with the lepton trigger matching requirement described in Chapter 5 and the electron or muon selection described in Chapter 6 mean that the electron and muon trigger chains are the most relevant.

### 3.3.1 Single Muon

The single muon trigger is one of the largest contributions to this analysis. This begins with the muon interacting with the various components of the detector as described in Chapter 2. The most useful interaction for muon triggering purposes is the Resistive Plate Chamber (RPC) hits. If there are coincident hits in multiple layers of the RPC, a muon candidate is flagged and passed to the HLT. The HLT then uses the RoI to make a few requirements on the quality of possible muon candidates. One of the requirements of the HLT is that hits in the RPC, TGC, MDT, and ID line up in  $\eta - \phi$  for a muon candidate. Another is that the muons be isolated from hadronic activity to improve the selection of muons originating from  $W$  boson or  $Z$  boson decays while mitigating muons from pion or heavy quark decays which are put into B-physics streams. Cosmic muons are rejected when the muon hits do not point back to the interaction point. Once the above requirements have been met, further checks are performed to ensure the quality of muons they must be wholly reconstructed by every layer of the detector, and verify that the requirements are accurately met. The event is then stored with information on the various triggers passed or failed, and objects are reconstructed offline [97]. The efficiency of the single muon trigger is assessed separately in the barrel and forward regions, and is significantly better in the forward regions as shown in Figure 3.2 [21]. The difference in efficiency is largely due to the crack region around  $\eta = 0$ .

### 3.3.2 Single Electron

One of the most relevant triggers that applies to this analysis is the single electron trigger. This begins with the electron interacting with the various components of the detector as described in Chapter 2. At L1, energy depositions in the electromagnetic and hadronic

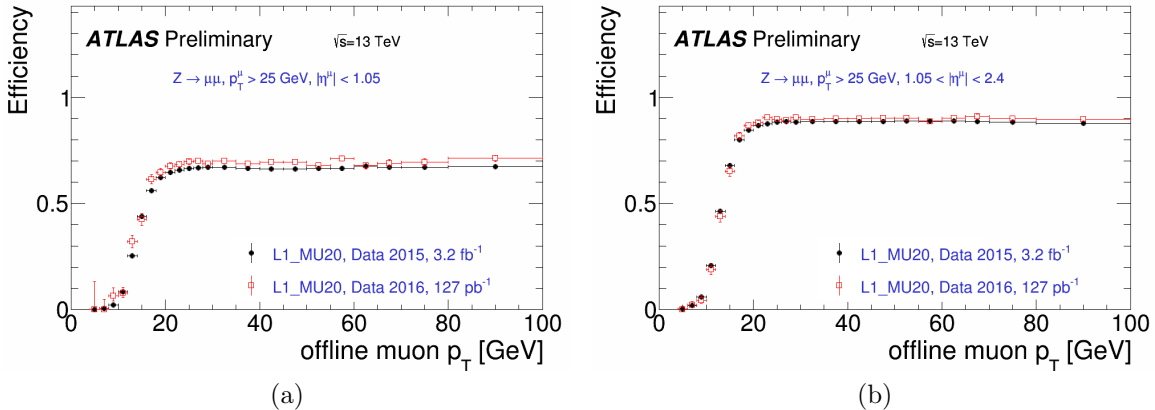


Figure 3.2: Trigger efficiency for the single muon trigger in (a) the barrel region and (b) the endcap region. [21]

calorimeters are considered, and a RoI is built around high energy depositions. For electrons the electromagnetic depositions are used to build the RoI. This RoI cluster must be high enough in energy as well as being isolated from other activity in the electromagnetic calorimeter and the hadronic calorimeter. At this point the ROI is passed to the HLT. Note that the object passed is not an electron yet, because photons exhibit very similar behavior with its interactions in the electromagnetic calorimeter. Once an RoI has been passed to the HLT we can take inner detector interactions into account. Energy clusters in the electromagnetic calorimeter are matched in  $\eta - \phi$  and its energy are compared to the momentum measured by the inner detector tracks. Isolation requirements in the electromagnetic calorimeter and hadronic calorimeter are re-assessed after corrections are applied, and isolation on tracks are applied to ensure the entire energy deposit came from one proton-proton interaction. Once these requirements are met the event is stored with information on the various triggers passed or failed and the electron (and other objects in the event) is reconstructed offline [97]. Overall the efficiency of the single electron trigger is quite good at over 90% for all energies used for this analysis as seen in Figure 3.3 [22].

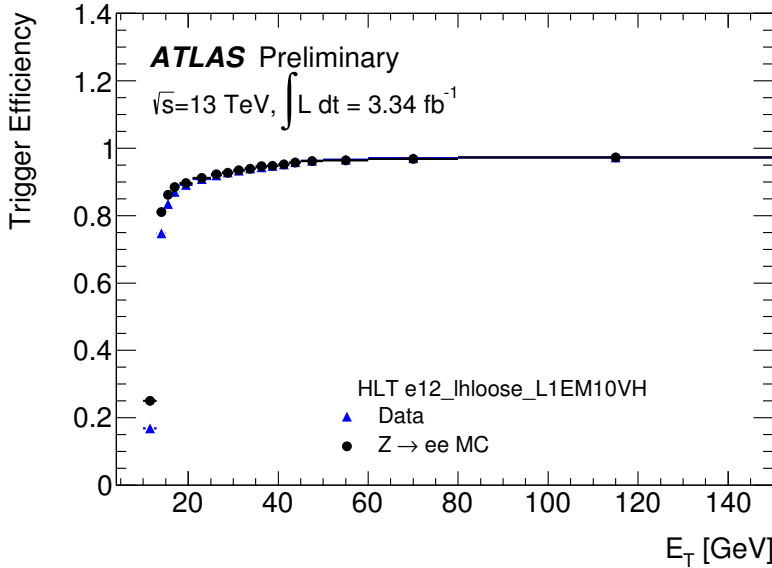


Figure 3.3: Efficiency of the single electron trigger over transverse energy ranges in the ATLAS detector [22].

Multilepton triggers are used that work on similar principles as the single electron and single muon triggers. These trigger chains have varied thresholds to accept pairs of objects that are individually more loosely defined (both in energy/momenta thresholds as well as isolation) compared to their single counterparts [98].

# Chapter 4

## Event Simulation

All laws are simulations of reality. -John C. Lilly

The ability to discover anything in high energy physics hinges on our ability to accurately model our signal and backgrounds in order to distinguish the kinematic properties of the background events from the kinematic properties of the signal being searched for. The simulation comes in several steps. First we simulate the parton level interactions with one of several different Monte Carlo generators. Then we go through a parton showering process to take bare quarks and hadronize them into jets, which is performed by one of several different parton showering programs. Next we go through a detector simulation in order to mimic how particles interact with ATLAS using the GEANT4 [99] package for all processes. Lastly we run our simulations through the same software that is used to process data to reconstruct objects as described in Chapter 5.

Backgrounds considered in this analysis are:

- Diboson processes including  $WW$ ,  $WZ$ , and  $ZZ$ .
- Top-quark pair production,  $t\bar{t}$ .
- Top-quark pair + boson production which is the same as Top-Quark Pair Production but with a radiated  $W$  boson or  $Z$  boson,  $t\bar{t}Z$  or  $t\bar{t}W$ .

- $Z$  boson+jets.
- Single Top-Quark Production including  $s$ -channel,  $t$ -channel, and  $Wt$ -channel as described in Chapter 1.
- $W$  boson+jets and Multijet which are single lepton backgrounds.

and further details about how they were simulated can be found in Table 4.1.

process	generator	parton shower	pdf	order	cross-section (pb)
$t\bar{t}$	Powheg	Pythia6	CT10/ CTEQ6L1	NLO (0 extra partons)/ LO ( $>0$ extra partons)	451.6
Single-Top	Powheg	Pythia8	CT10/ CTEQ6L1	NLO (0 extra partons)/ LO ( $>0$ extra partons)	$t$ -channel :70.3 $Wt$ -channel :35.8 $s$ -channel :3.44
$t\bar{t}V$	Madgraph5	Pythia8	CTEQ6L1	LO	$t\bar{t}Z$ : 0.471 $t\bar{t}W$ : 0.567
$Z + \text{jets}$	Sherpa2.2.1	Sherpa2.2.1	CT10	NLO ( $<2$ extra partons)/ LO (3 or 4 extra partons)	17486.7
Diboson	Powheg	Pythia6	CT10/ CTEQ6L1	NLO (0 extra partons)/ LO ( $>0$ extra partons)	$WW$ : 101.3 $WZ$ : 137.7 $ZZ$ : 124.5
$tZ$	Madgraph5	Pythia8	CTEQ6L1	LO	0.240

Table 4.1: Information on generators for each process considered. All cross-sections consider full decays including hadronic.

## 4.1 The Monte Carlo Method

Simulating the data begins with Standard Model predictions, which in an ideal world could be calculated exactly. We employ the Monte Carlo method to perform integrations that are cumbersome to perform by hand and where numerical methods are more appropriate in order to calculate relative rates at which particles interact with each other. From this, fundamental properties of outgoing partons can be predicted.

There are a plethora of generators and parton showering programs which excel at simulating various processes. The ATLAS top group recommends which Monte Carlo programs

to use for every sample except  $tZ$  for which there is no recommendation.

## 4.2 Signal Simulation

Several Monte Carlo generators are considered to model the  $tZ$  process. Madgraph [100] is used to generate samples and Pythia [101] is used to perform parton showering. Madgraph5+Pythia8 is chosen because this is the same generator and showering setup used to simulate  $t\bar{t}+X$ . Another reason Madgraph5+Pythia8 is chosen is that Madgraph and Pythia have been widely used tools for quite a while in high energy physics and as a result they are very well understood generators with good simulation of a wide variety of physics processes. One of the limitations of Madgraph is that it is a leading order (LO) generator.

One consideration when generating  $tZ$  is what decay modes of the  $Z$  boson and  $W$  boson should be generated. For this analysis we are interested in the all leptonic mode with the  $Z$  boson and the  $W$  boson decaying to leptons. Other analyses within ATLAS are interested in different lepton multiplicities which can be varied by either the  $W$  boson decaying hadronically, the  $Z$  boson decaying hadronically, or the  $Z$  boson decaying to a pair of neutrinos which is known as the invisible mode. The fully hadronic mode for  $tZ$  has a large branching ratio and is not of interest to ATLAS analyses due to the lack of a distinct signature in the detector to trigger on, so to save on computing time it is not included in the Monte Carlo sample. Every other combination is produced.

Another consideration is how we parametrize the incoming partons. This is described by Parton Distribution Functions (PDFs) and the PDF that is used for this Monte Carlo sample is CTEQ6L1 from the LHAPDF interface as per single top group recommendations [102, 103, 104]. A technique where only light quarks are included in the parton distribution function

of the incoming protons (the 4 flavor scheme) is used so the incoming  $b$  quark shown in Figure 1.6 must come from gluon splitting where the  $b$ -antib quark pair are produced from an initial state gluon. The top-quark mass used for Madgraph single top quark samples is 172.5 GeV.

## 4.3 Diboson Production

Among the most prominent backgrounds is Diboson which is a large non-top background in this analysis. Its relative contribution is not surprising considering the most prominent Diboson contribution is  $WZ$ , which contains a real  $Z$  boson , three leptons, and  $E_T^{\text{miss}}$  (which is described in Chapter 5.5). Additional jets can come from Initial State Radiation (ISR) or Final State Radiation (FSR) where a gluon is radiated off and is constructed as another object entirely. Diboson production is modeled with the next to leading order (NLO) generator POWHEG and showered in PYTHIA6 [105, 101].

## 4.4 Top-Quark Pair Production

Top-quark pair production is a dominant background for almost any search involving a top quark. Its large cross-section means that it is difficult to remove even if distinct kinematic differences exist. This process can have 0, 1, or 2 leptons, meaning that every  $t\bar{t}$  event that passes selection by definition has at least one jet which is mis-reconstructed as a lepton. Beyond having a jet mis-reconstructed as a lepton two of those leptons (at least one of which is not a true lepton) will have to be mis-reconstructed as a  $Z$  boson within the constraints outlined in Chapter 6. Powheg is used to model  $t\bar{t}$  and it is showered with Pythia6 [105, 101].

## 4.5 Top-Quark Pair + Boson Production

The  $t\bar{t}+X$  is a process that has been under study within ATLAS and indications are that this process will be observed soon [48]. The  $X$  in  $t\bar{t}+X$  can be a  $Z$  boson, a  $W$  boson, or a Higgs boson. The  $t\bar{t}+Z$  contributes much more strongly when compared with  $t\bar{t}+W$  due to the  $Z$  boson. This process has 0, 1, 2, 3, or 4 real leptons, and only the 3 lepton contribution contributes to our final state as selection cuts in Chapter 6 describe. The  $t\bar{t}+Z$  matches our signal fairly closely. Madgraph5 is used to model  $t\bar{t}+X$  and it is showered with Pythia8 [100, 101].

## 4.6 $Z$ boson+jets

$Z$  boson+jets is another large background because it has a real  $Z$  boson. Despite not having a top quark and only having two real leptons, it still remains an important background to consider due to its large cross-section.  $Z$  boson+jets taken in combination with  $t\bar{t}$  constitutes a majority of mis-reconstructed leptons that come up in this analysis due to these samples naturally containing fewer than three leptons.  $Z$  boson+jets is modeled and showered with Sherpa [106].

## 4.7 Single Top Quark

Both  $t$ -channel and  $s$ -channel have only one lepton, and while considered for this analysis, they contribute no events. However,  $Wt$ -channel has two real leptons and a real top quark which leaves it close enough to  $tZ$  to add to the event yield in a small way. Single top-quark simulation is performed with Powheg+Pythia8 [105, 101].

## 4.8 $W$ boson+jets and Multijet

Also considered for this analysis is  $W$  boson+jets production. This process, despite having a large cross-section in comparison to the other backgrounds considered, is completely eliminated by preselection cuts described in Chapter 6 because it has no  $Z$  boson, no top quark, and only one lepton. This means it would require 2 jets to be mis-reconstructed as leptons. Given that the  $W$  boson+jets process has no contribution due to the combinatorics of requiring so many mis-reconstructed leptons and bosons, multijets will also have no contribution as it requires three mis-reconstructions that match the kinematic properties of the  $W$  boson and  $Z$  boson. Both Sherpa and Powheg+Pythia are considered for  $W$ +jets simulations and for both zero events passed the event preselection (see Section 6.1) [106, 105, 101].

## 4.9 Weighting and Corrections

When generating MC events, we must generate a sufficiently large sample to get a variety of potential kinematic properties and to ensure a low statistical uncertainty. In order to compare this generated Monte Carlo to data we must weight the sample appropriately. Firstly the number of generated Monte Carlo events does not match the number of data events so the Monte Carlo gets scaled by the cross-section ( $XS$ ) of the process. This includes the K-factor ( $K$ ) which scales it to higher order calculations, the branching ratio ( $BR$ ) for decays specified by the process generated, the integrated luminosity ( $L$ ) of the data collected, and the number of generated events ( $N_{MC}$ ) calculated as shown in Equation 4.1.

$$\frac{XS \cdot BR \cdot K \cdot L \cdot PUSF \cdot LepSF \cdot BtagSF}{N_{MC}} \quad (4.1)$$

Another weight used is the pile-up scale factor ( $PUSF$ ) which scales the Monte Carlo to account for both in-time and out-of-time pile up which is discussed in Chapter 2. The lepton scale factor ( $LepSF$ ) adjusts for differences between simulation and data of leptons. Lastly there is a b-tagging scale factor ( $BtagSF$ ) which accounts for data Monte Carlo disagreement. These scale factors are all between 0 and 2. The assessment of these scale factors are systematic uncertainties described in Chapter 7.

# Chapter 5

## Object & Event Reconstruction

I was always interested in figuring things out. I'd do experiments, like combining things I found around the house to see what would happen if I put them together. - Alan Alda

In practice, high energy physics is messy. Having particles that interact with several different layers of the detector makes our particle identification and reconstruction complex but possible. By using tracking from the inner detector, energy measurements from the calorimeters, more tracking from the muon spectrometers, and by looking at global variables that have to do with event kinematic properties we can ensure quality physics objects for analysis. This analysis in particular uses a wide variety of objects including electrons, muons, jets, b-jets,  $E_T^{\text{miss}}$ , reconstructed  $W$  bosons and  $Z$  bosons, and the heaviest of all fundamental particles with one of the most unique signatures, the top quark.

### 5.1 Electron Reconstruction

Electrons use information from the inner detector and the electromagnetic calorimeter. Electrons are among the more scrutinized reconstructed objects because hadronic jets, photons, and taus can fake electrons heightening the importance of quality control. Electron candidates are required to be within  $|\eta| < 2.47$  as measured by the tracks in the inner detector with  $p_T > 7 \text{ GeV}$  as measured by an energy cluster (energy deposits within  $dR$  of 0.4) in the

calorimeter. Requirements on the transverse impact parameter ( $d_0$ ) and the longitudinal impact parameter ( $z_0$ ) constrain the degree to which tracks in the ID are allowed to vary from the interaction point while still being counted as part of the electron object. Ratios of energy measured in the electromagnetic calorimeter and the hadronic calorimeter are also used to reject jets that interact within the electromagnetic calorimeter and could fake electrons. Ratios of energy in varying window sizes in the electromagnetic calorimeter are also used to help distinguish other activity such as pions from electrons. These reconstructed electrons are required to have  $p_T > 25$  GeV, then trigger matched with L1 EM objects and HLT electrons and required to be isolated from hadronic activity [107, 108, 109].

## 5.2 Muon Reconstruction

Muons use information from the inner detector, the muon systems, and to a lesser extent the calorimeters. Muons are not stopped by the detector, making full calorimetry impossible, so their energy must be determined by their curvature in the magnetic field set up by ATLAS's namesake toroidal magnet system.

There are four algorithms that are used in muon reconstruction and define the requirements for various levels of the muon reconstruction provided to analyzers. One method used starts from hits in the muon spectrometer and traces them back to a primary vertex to create a standalone muon. Another method combines an inner detector track with a muon spectrometer track to produce a combined muon. Yet another method performs a search for segments and tracks in the muon spectrometer using an inner detector track as a seed, and if the refit performed is successful, then a Combined muon is made, if not then a tagged muon is made. The fourth method identifies muons by associating an inner detector track

with a standalone muon in a similar way to the first method to produce a tagged muon. Muons from all of these algorithms are added after overlapping definitions are accounted for [110, 111].

### 5.3 Jet Reconstruction

Hadronizing quarks and gluons interact with the inner detector, the electromagnetic calorimeter, and the hadronic calorimeter. We use this information to reconstruct the location and energy of the jets.

There are several jet reconstruction algorithms but the most common are described by equations 5.1 and 5.2,

$$d_{ij} = \min(p_{T,i}^{2p}, p_{T,j}^{2p}) \frac{\Delta\eta_{ij}^2 + \Delta\phi_{ij}^2}{R^2}, \quad (5.1)$$

$$d_i = p_T^{2p}, \quad (5.2)$$

where  $p_T$  is the transverse momentum to the power of  $2p$  which is either 1, 0, or -1. These three values correspond to the kt, Cambridge Achen, or anti-kt algorithm [112]. These algorithms work by considering every cell of the detector as an object in a list enumerated by  $i$  and  $j$  and considering pairs of these cells for combination by this equation. If the minimum  $d_{ij}$  is smaller than  $d_i$  then the two objects are combined into one object. If a  $d_i$  is smaller then that object is removed and considered a jet. This continues until all objects are removed from the list. The parameter  $R$  sets the separation distance between two jets.

The first of these three algorithms is the kt algorithm which gives irregular jets, but

is more theoretically sound than simple cone drawing. The Cambridge Aachen algorithm gives jets that are slightly more regular but are larger than their  $kt$  counterparts, while the anti- $kt$  algorithm gives jets that are more regular than the  $kt$ . The anti- $kt$  algorithm is the one chosen for ATLAS and this analysis considers anti- $kt$  jets with an  $R$  parameter of 0.4, and for high  $p_T$  jets (greater than 50 GeV) the Jet Vertex Tagger (JVT) output variable is required to be greater than 0.64 [113].

After the selection of jets with the anti- $kt$  algorithm, corrections are applied to each jet based on the jet's position and  $p_T$  to correct for specific detector effects. These corrected jets have a series of quality cuts applied including a minimum  $p_T$  threshold of 30 GeV, a check for unphysical negative energy jets, an eta range  $|\eta| < 4.5$  and electron isolation requirements to ensure that an electron is not being double counted as a jet.

### 5.3.1 Jet $b$ -tagging

Jets that are  $b$ -tagged are unique because the  $b$  quark decays after the hadronization process begins but before it interacts with the detector. This creates a secondary vertex (displaced by a few millimeters) which can be found by looking at the tracking information from the inner detector [23]. This can be seen diagrammatically in Figure 5.1. The  $b$ -tagging algorithm used in ATLAS for Run 2 is the MV2c20 algorithm [114]. When this algorithm is applied to anti- $kt$  jets with an  $R$  parameter of 0.4 the  $p_T$  of the jet is required to be greater than 20 GeV, the  $\eta$  is required to be less than 2.5. The MV2c20 algorithm is a neural network analysis of  $b$ -tagging algorithms used in ATLAS to create a single discriminating variable that can distinguish between jets originating from a  $b$  quark and all other jets. [115].

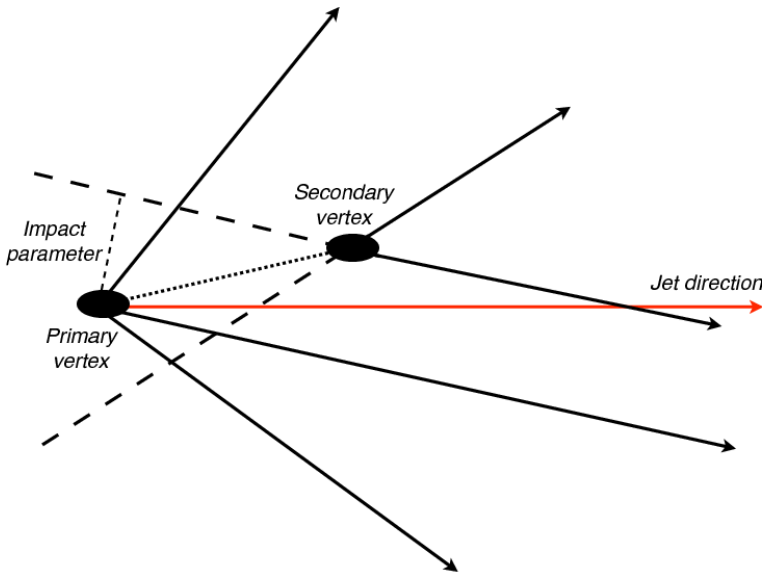


Figure 5.1: Diagram illustrating a displaced vertex. [23].

## 5.4 $Z$ boson

Now that we have the leptons defined we can reconstruct the intermediate  $Z$  boson. We require that the  $Z$  boson be constructed from an Opposite-Sign Same-Flavor (OSSF) lepton pair. With three leptons (which can be electrons or muons) we can have 0, 1, or 2 OSSF pairs. There are two fundamental cuts we make in Section 6.1. When there is one OSSF pair, the  $Z$  boson is reconstructed with those, and the remaining lepton is used to reconstruct the  $W$  boson. When there are two OSSF pairs, then the OSSF pair which reconstructs the  $Z$ -boson mass more closely is considered, and the remaining lepton reconstructs the  $W$  boson. The last case with no OSSF pair represents either a charge misidentification of a lepton or a jet mis-reconstructed as a lepton whose charge couldn't be properly reconstructed. In this case the event is rejected.

## 5.5 Missing Transverse Energy ( $E_T^{\text{miss}}$ ) and the $W$ boson

For each event we apply conservation of momentum in the transverse plane of the detector to obtain what is known as missing transverse energy ( $E_T^{\text{miss}}$ ). We often use  $E_T^{\text{miss}}$  as a stand in for some information on neutrinos. While we can not apply the same method to find the neutrino  $p_z$ , because the colliding partons do not necessarily have balanced  $z$  momenta, we can make the assumption that it came from a  $W$  boson and begin with conservation of four-momentum of the  $W$  boson decay vertex with the momentum of the  $W$  boson  $p_w^\mu$ , the momentum of the neutrino  $p_\nu^\mu$ , and the momentum of the lepton  $p_l^\mu$ .

$$p_w^\mu = p_\nu^\mu + p_l^\mu \quad (5.3)$$

The lepton up for consideration is the one that did not come from the  $Z$  boson. Solving for the  $p_z$  of the neutrino we obtain the following quadratic:

$$p_{z\nu} = \frac{\alpha p_{zl}}{p_{tl}^2} \pm \sqrt{\frac{\alpha^2 p_{zl}^2}{p_{tl}^4} - \frac{E_l^2 p_{t\nu}^2 - \alpha^2}{p_{tl}^2}} \quad (5.4)$$

$$\alpha = \frac{m_w^2}{2} + \cos(\Delta\phi)p_{t\nu}p_{tl}. \quad (5.5)$$

Equation 5.4 can have two, one, or no real solutions. If it has two real solutions, the one with lower  $p_z$  is chosen. In the case where there are no real solutions the measured  $E_T^{\text{miss}}$  is scaled to the point where one real solution is found. The measured  $E_T^{\text{miss}}$  and azimuthal angle ( $\phi$ ) of the  $E_T^{\text{miss}}$  and the reconstructed  $p_z$ , and because neutrinos are functionally massless, define the neutrino four vector.

Now that the neutrino is defined, we have reconstructed the four vectors for all of our

final state particles. We can reconstruct the  $W$  boson, but the mass will already be defined because we assumed the  $W$ -boson mass in reconstructing the neutrino. For this reason, and to remain independent of any assumptions regarding  $z$  momenta, the experimental variable  $m_T^W$  is used. This is the transverse mass of the  $W$  boson, which as defined by the energies of the lepton and neutrino ( $E_{Tl}, E_{Tv}$ ) and the angle between them( $\Delta\phi$ ) in equation 5.6. It is used to help distinguish events that have a real  $W$  boson from events that don't [116, 117].

$$m_T^W = \sqrt{2E_{Tl}E_{Tv}(1 - \cos(\Delta\phi))} \quad (5.6)$$

The helicity of the  $W$  boson is another variable which can be used to distinguish events with a real  $W$  boson from ones that do not. Furthermore,  $W$  bosons from top decays have correlations with the  $b$ -jet because they carry forward information about the spin of the top quark. Helicity is defined as the projection of the spin vector( $s$ ) onto the momentum vector( $p$ ) as defined in equation 5.7.

$$H = \frac{s \cdot p}{|s \cdot p|} \quad (5.7)$$

## 5.6 Reconstructing the top quark

Once the  $W$  boson is reconstructed and the  $b$ -jet selected, the reconstruction of the top quark is simply the result of the addition of the four vectors of the two objects. The top quark decay has properties that are used to help distinguish signal and backgrounds, even though this analysis has a large background contribution from top-quark pair production as seen in Chapter 6. One of those properties is the top-quark polarization, which is unique because the top quark decays before its spin can be flipped by the strong interaction allowing

this to be measured in single top production. The top-quark polarization is evaluated as the angle between the lepton from the top quark decay and the polarization axis, in the top quark rest frame [118]. The polarization of the top quark is dependent on what reference frame you are measuring from. Two common reference frames for this are the Optimal Basis and the Helicity Basis. The Helicity Basis, which is the most common basis of consideration, takes the top quark rest frame. The Optimal basis is the helicity basis measurement boosted into the reference frame of the jet that does not come from the top decay in the case of single top  $t$ -channel.

# Chapter 6

## Analysis

Let's think the unthinkable, let's do the undoable. Let us prepare to grapple with the ineffable itself, and see if we may not eff it after all. -Douglas Adams

After the  $Z$  boson, the top quark, the  $W$  boson from the top quark decay, and the neutrino from the  $W$  boson decay are reconstructed as described in Chapter 5, they are used to help separate  $tZ$  from the various backgrounds. The energies and momenta of each of these objects in our detector, as well as the multiplicity of the objects, are used to achieve this separation. The decisions made in the preselection and cut flow are informed by the kinematic properties of the  $tZ$  process. The  $tZ$  Feynman diagram is shown in Figure 1.6.

### 6.1 Preselection

One goal in setting up an analysis is to understand the background model in relation to the observed data. To accomplish this, defining characteristics of the signal region are determined in order to limit the number of Monte Carlo samples needed. Because the signal has three leptons and a  $Z$  boson, cuts on the number of leptons and  $Z$ -boson mass (for instance) are applied to limit any contribution from certain low lepton multiplicity non- $Z$ -boson sources such as  $W$  boson+jets and multijets.

The following cuts are optimized by maximizing  $S/\sqrt{B}$  where  $S$  is the total expected

signal contribution and  $B$  is the total expected background contribution. This is done to improve agreement between data and the background model while maintaining as much signal statistics as possible.

- Exactly 3 leptons with  $p_T > 10$  GeV. Exactly 3 leptons is a defining feature of this analysis. Two of the leptons come from the  $Z$  boson decay, while the third comes from the top quark decay. Because these leptons are required to be electrons or muons their distributions are mirrors of each other by definition which can be seen in Figure 6.15.
- At least one OSSF pair. Because we are concerned with processes that contain a real  $Z$  boson, this requirement ensures that we can always attempt to reconstruct a valid  $Z$  boson candidate even if it is an event that is mis-identified as containing a  $Z$  boson.
- Leading lepton  $p_T > 40$  GeV. The leading lepton's threshold is higher than the second and third due to being more likely that it is the candidate that is required to pass the single lepton trigger or a candidate in the case of a multi-lepton trigger. Figure 6.1 shows that this cut removes some background, but little signal is lost.
- Second lepton  $p_T > 20$  GeV. This lepton is not required to have passed a single lepton trigger, but may have been required to pass the di-electron trigger threshold. Figure 6.1 shows that this cut removes some background, but little signal is lost. Tightening this cut is also investigated because  $Z+jets$  and  $t\bar{t}$  peak at a lower momentum than the signal, but in the interest of maintaining statistics a lower  $p_T$  threshold is chosen.
- Third lepton  $p_T > 10$  GeV. The  $p_T$  of this lepton is significantly lower than the rest. 10 GeV is chosen due to the thresholds that define how electrons are reconstructed. Figure 6.1 shows that the signal peaks at higher  $p_T$  than  $Z+jets$  and  $t\bar{t}$ , and tightening

this cut is investigated, but in the interest of maintaining statistics, a lower  $p_T$  threshold is chosen.

- 2, 3, or 4 jets with  $p_T > 25$  GeV. Figure 6.2 shows that the one jet region contains virtually no signal, so removing it eliminates background at no cost, while events with  $\geq 5$  jets have little signal and are not as well modeled.
- Leading jet  $p_T > 40$  GeV. Figure 6.1 shows that below 40 GeV, there is less than 1 expected signal events, so very little is removed.
- Exactly 1  $b$ -jet. Figure 6.2 shows that there is little signal outside the one  $b$ -jet region. The signal and top backgrounds have one  $b$ -jet from the top decay while non-top backgrounds are unlikely to have one.
- $80 \text{ GeV} < Z\text{-boson mass} < 100 \text{ GeV}$ . The  $Z$  boson is a defining feature of this analysis. The signal and all backgrounds except  $t\bar{t}$  and single top quark production have a real  $Z$  boson. Figure 6.3 shows how much  $t\bar{t}$  is off the  $Z$  peak and a cut here will give substantial gains in removing  $t\bar{t}$  background without removing a significant amount of signal events.
- $E_T^{\text{miss}} > 20$  GeV. This cut defines processes that have a real source of  $E_T^{\text{miss}}$  such as the neutrino from top-quark decays. Figure 6.2 shows that the low  $E_T^{\text{miss}}$  region is populated heavily by  $Z+\text{jets}$  with little signal.
- If  $m_T^W < 40$  GeV then  $E_T^{\text{miss}} > 40$  GeV is required. If viewed in the two dimensional plane, cases where jets are mis-reconstructed as leptons are expected to have low  $m_T^W$  and low  $E_T^{\text{miss}}$ . Distributions for  $m_T^W$  and  $E_T^{\text{miss}}$  can be seen independently in Figure 6.2. The 2D plane of  $m_T^W$  vs.  $E_T^{\text{miss}}$  is shown for both signal and data in

Figure 6.3. Here we can see that the signal peaks above 20 GeV in  $E_T^{\text{miss}}$  and above 40 GeV in  $m_T^W$  while data preferentially resides in the region where both  $m_T^W$  and  $E_T^{\text{miss}}$  are below 40 GeV. This cut is primarily targeted at  $Z+\text{jets}$  events (as well as potential backgrounds with mis-identified  $W$  bosons) which heavily populate the low  $m_T^W$  region. This cut is referred to as the notch cut because of its unique shape.

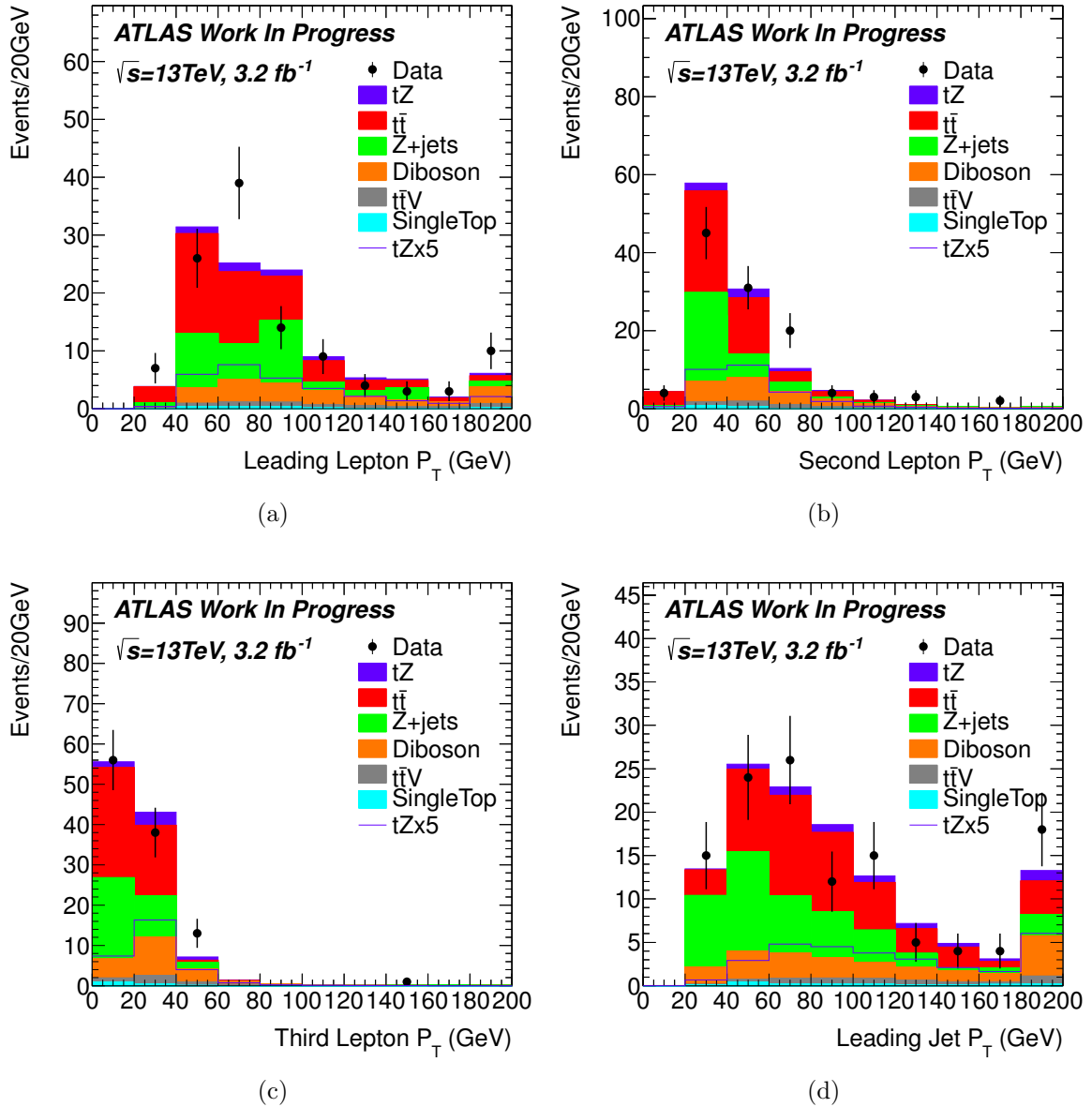


Figure 6.1: Distributions of Lepton  $p_T$  for (a) leading, (b) second, and (c) third leptons as well as (d) leading jet  $p_T$  with preselection applied except the cuts on minimum  $p_T$  thresholds shown which are 40 GeV for the leading lepton, 20 GeV for the second lepton, 10 GeV for the third lepton, or 40 GeV for the leading jet. There are minimum  $p_T$  reconstruction thresholds for these objects which are 25 GeV for the leading lepton and leading jet, and 10 GeV for the second and third leptons.

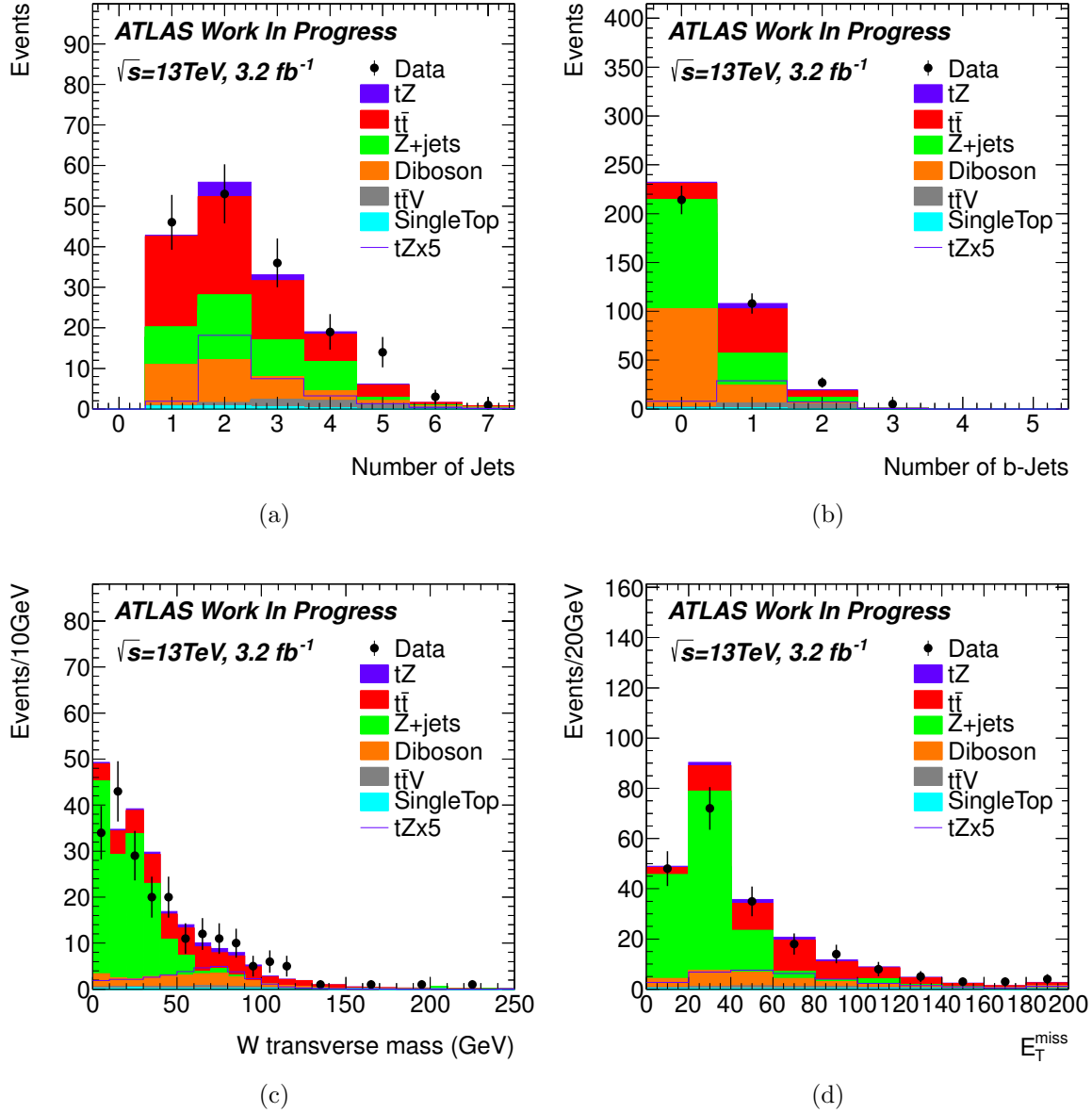


Figure 6.2: Distributions of (a) number of jets, (b) number of  $b$ -jets, (c)  $m_T^W$ , (d)  $E_T^{\text{miss}}$ . At least one jet is required at this level in all cases, but the cut on the variable shown is omitted in order to assess the full distribution. The distribution of the number of jets does not include the cut on the number of jets, the distribution of the number of  $b$ -jets does not include the cut on the number of  $b$ -jets, and the  $m_T^W$  and  $E_T^{\text{miss}}$  distributions do not contain the  $E_T^{\text{miss}}$  or the notch cuts.

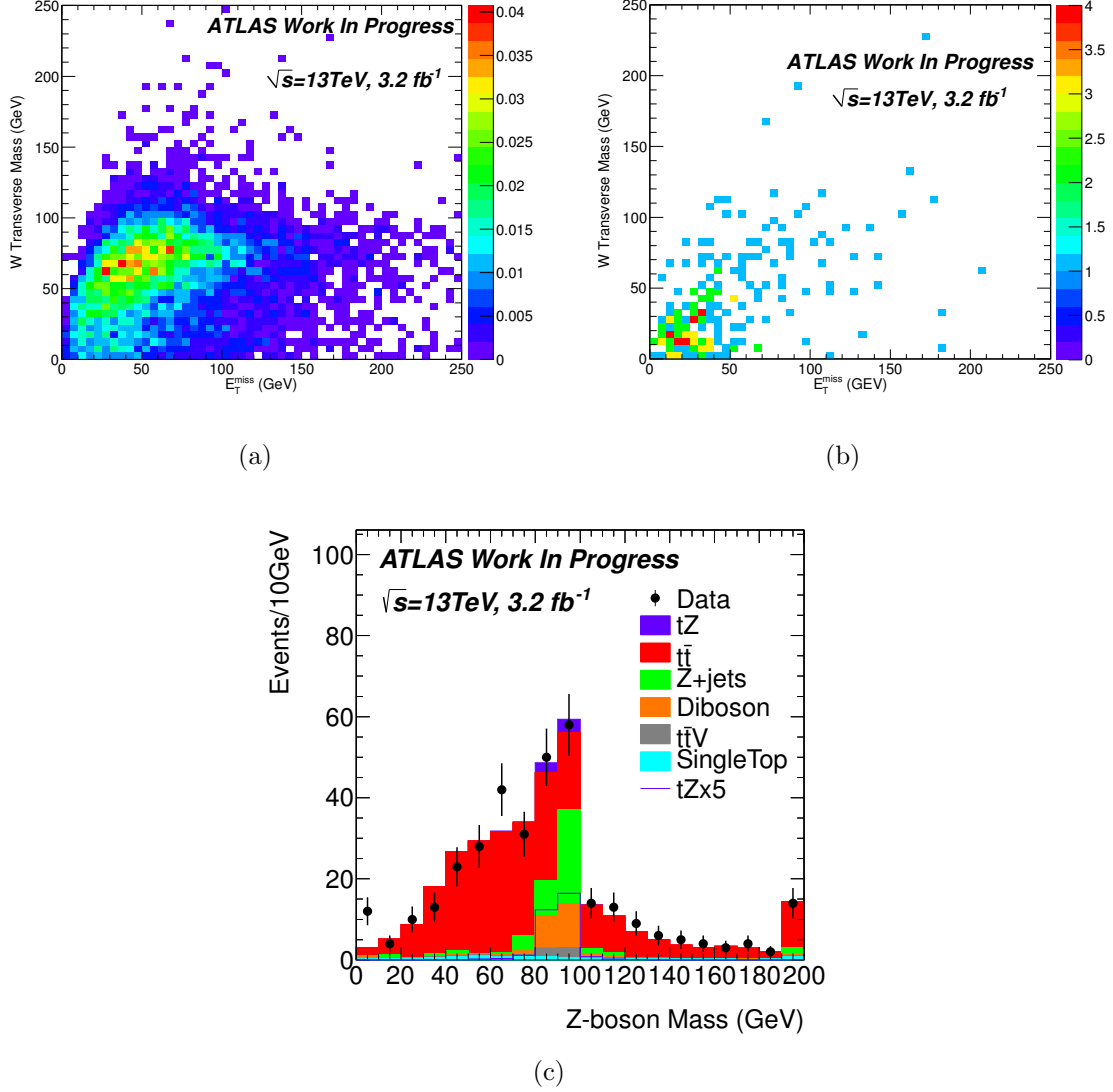


Figure 6.3: Distributions of (a) two-dimentional map of  $m_T^W$  vs  $E_T^{\text{miss}}$  for the signal, (b) two dimentional map of  $m_T^W$  vs  $E_T^{\text{miss}}$  for the data, and (c) invariant mass of the  $Z$  boson. For both (a) and (b) the  $E_T^{\text{miss}}$  cut and the notch cut are not applied and for (c) the  $Z$ -boson mass window cut is not applied in order to show the full distribution.

## 6.2 Control Regions

Three control regions are considered for the three primary backgrounds to ensure that the background model describes the data well. The control regions are for  $t\bar{t}$ , Diboson, and  $Z+jets$  and their yields are summarized in Table 6.1 where it can be seen that  $tZ$  contamination is small and that the control regions are fairly pure in their respective backgrounds. The control region for  $t\bar{t}$  is defined by the preselection cuts with the exception of the  $Z$ -boson mass window which is inverted. This has the effect of cutting out large contributions which contain a real  $Z$  boson, leaving primarily  $t\bar{t}$ . In every distribution shown in Figures 6.4 and 6.5, there is good agreement between data and simulated events with a quite pure sample of  $t\bar{t}$ . In order to isolate Diboson and  $Z+jets$ , we begin with the preselection again, but instead of requiring exactly 1  $b$ -jet, we require exactly 0  $b$ -jets in order to eliminate top-quark contributions. This defines an intermediate control region with Diboson and  $Z+jets$  mixed as shown in Figures 6.6 and 6.7. This is expected because both Diboson and  $Z+jets$  have a real  $Z$  boson and do not have a  $b$  quark that would come from a top-quark decay. To isolate Diboson more precisely, a cut is placed on  $m_T^W$  to constrain it to higher than 80 GeV as shown in Figures 6.8 and 6.9. This provides a region with high Diboson purity to evaluate the quality of its modeling. In order to isolate  $Z+jets$  from the intermediate control region a cut on  $E_T^{\text{miss}}$  is made to constrain it to lower than 60 GeV as shown in Figures 6.10 and 6.11. This region has lower purity in  $Z+jets$  when compared to the  $t\bar{t}$  control region and the Diboson control region, and shows areas of mis-modeling in low to mid  $m_T^W$  (less than 70 GeV). Low lepton  $p_T$  also seems to be poorly modeled (20-40 GeV for each of the three leptons). This is likely because the third lepton must be a mis-reconstructed one. Despite also having a mis-reconstructed lepton, due to only having two real leptons,  $t\bar{t}$  does not show

similar mis-modeling for two primary reasons. The first reason is that  $t\bar{t}$  MC statistics is much better than  $Z$ +jets. The second reason is that  $t\bar{t}$  has more hard objects (extra jets) stemming from the primary interactions, while  $Z$ +jets has extra hard objects come from initial-state or final-state radiation. This mis-modeling is mitigated by cuts on  $p_T$ ,  $m_T^W$ , and  $E_T^{\text{miss}}$  as well as cuts made to the signal region. Even with these measures taken the mis-modeling reflects itself as large uncertainties on  $Z$ +jets which is shown in Chapter 7. Collectively these control regions give insight to the contribution of the largest backgrounds to this analysis.

Event Yields	Preselection	$t\bar{t}$ CR	intermediate CR	Diboson CR	$Z$ +jets CR	final selection
$t\bar{t}$	45	196	16	4.0	5.7	$10 \pm 45\%$
single top quark	1.4	7.7	0.85	0.26	0.30	$0.34 \pm 66\%$
$ttV$	4.4	2.7	1.0	0.38	0.30	$0.61 \pm 66\%$
$Z$ + jets	32	10	110	4.0	78	$1.7 \pm 413\%$
Diboson	18	5.0	100	31	48	$3.3 \pm 32\%$
$tZ$	5.7	0.63	1.6	0.4	0.68	$2.9 \pm 11\%$
Total Expected	108	223	232	41	134	$19 \pm 71\%$
Data Observed	108	237	214	52	131	22
S/B	0.06	0.00	0.01	0.01	0.01	0.18
S/ $\sqrt{B}$	0.57	0.04	0.10	0.07	0.06	0.71

Table 6.1: Event yields for various stages of analysis to compare with control region (CR) yields. The final selection is described in Section 6.3 and uncertainties provided on the final selection are described in Chapter 7 taken in quadrature for each sample. They are provided here for reference.

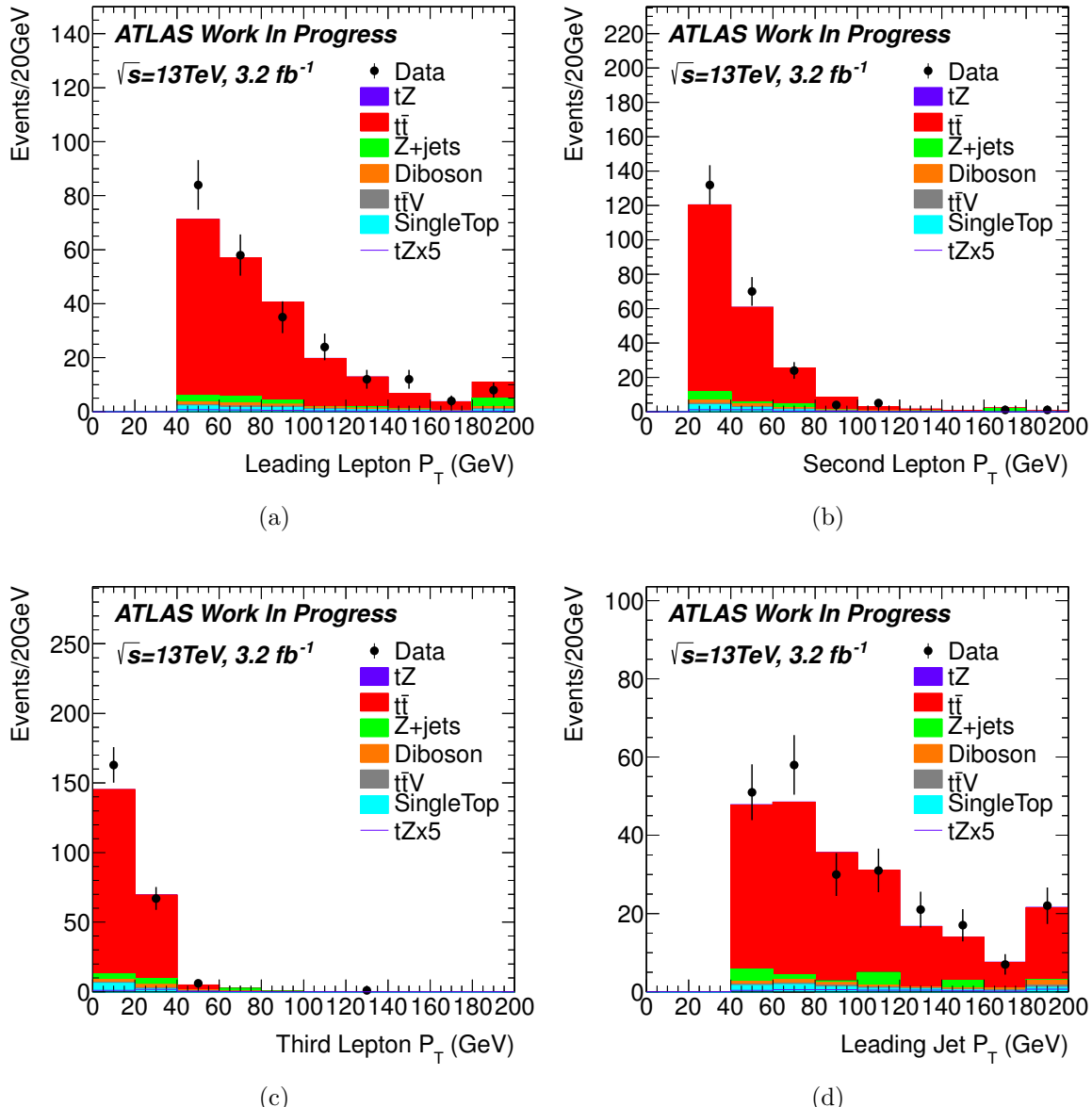


Figure 6.4: Distributions of transverse momenta for (a) the leading lepton, (b) the second lepton, (c) the third lepton, and (d) the leading jet in the control region for  $t\bar{t}$ .

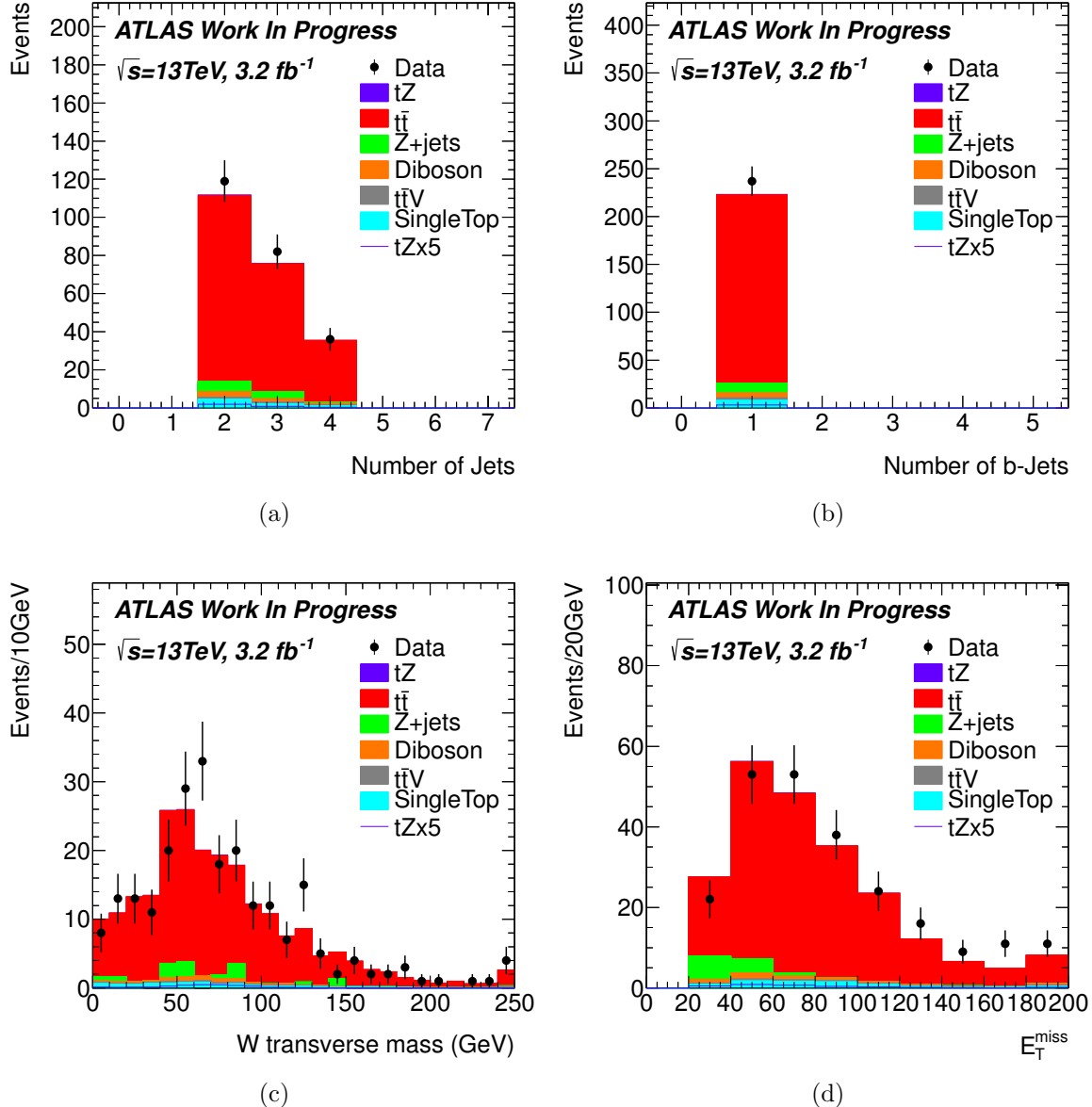


Figure 6.5: Distributions of (a) jet multiplicity, (b)  $b$ -jet multiplicity, (c)  $m_W^T$ , and (d)  $E_T^{\text{miss}}$  in the control region for  $t\bar{t}$ .

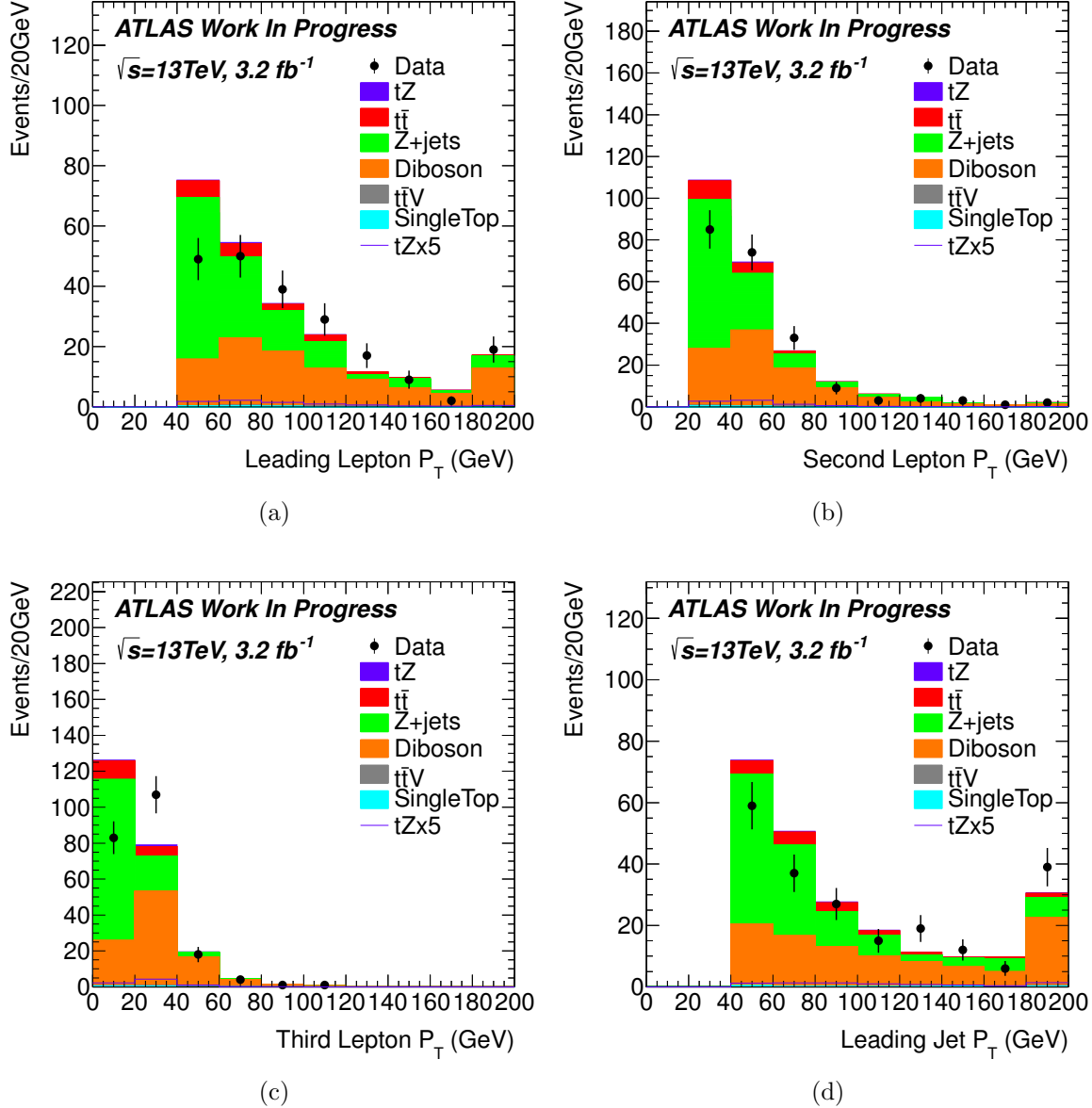


Figure 6.6: Distributions of transverse momenta for (a) the leading lepton, (b) the second lepton, (c) the third lepton, and (d) the leading jet in the intermediate control region for Diboson and  $Z+jets$ .

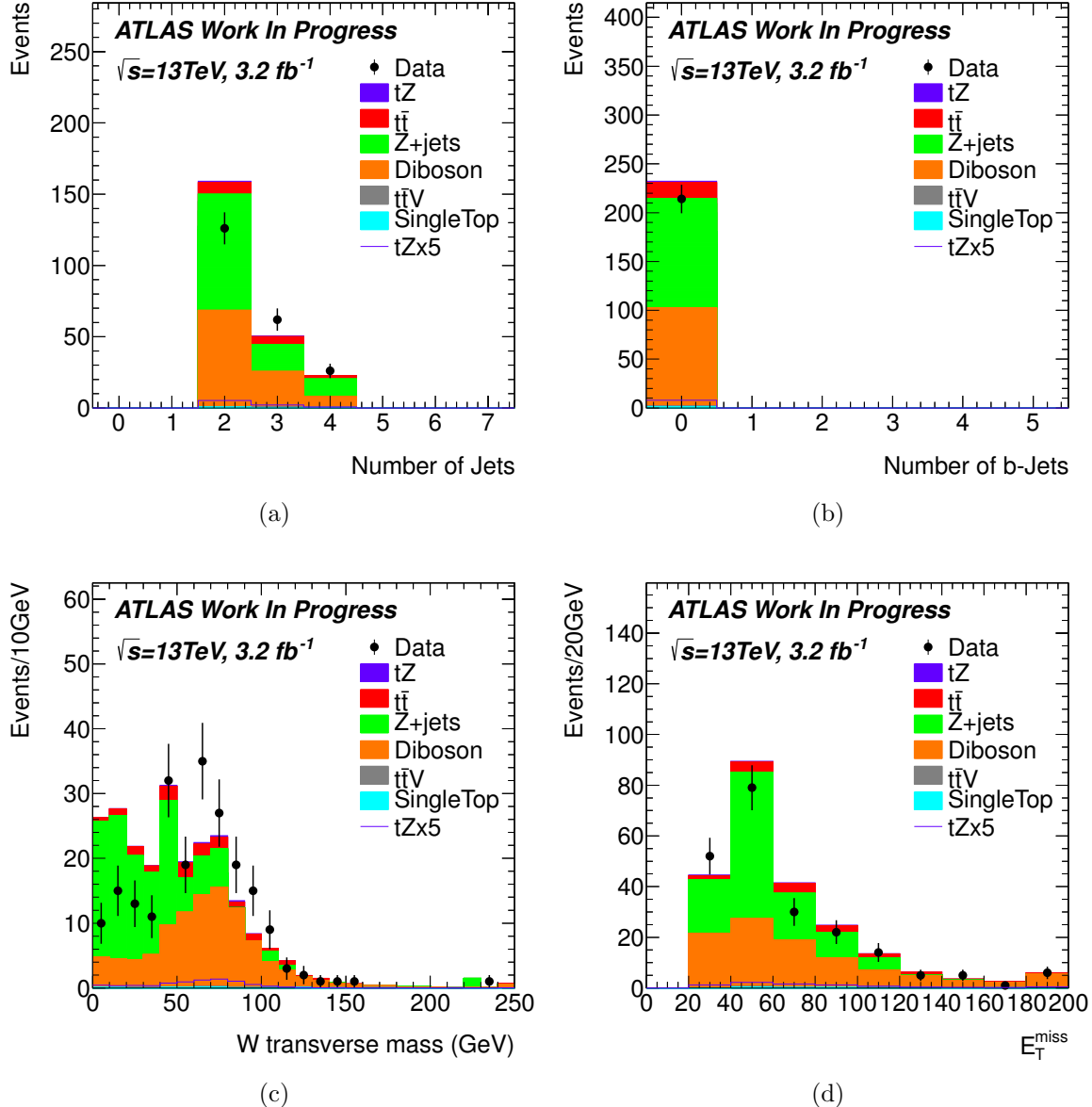


Figure 6.7: Distributions of (a) jet multiplicity, (b)  $b$ -jet multiplicity, (c)  $m_W^T$ , and (d)  $E_T^{\text{miss}}$  in the intermediate control region for Diboson and  $Z+\text{jets}$ .

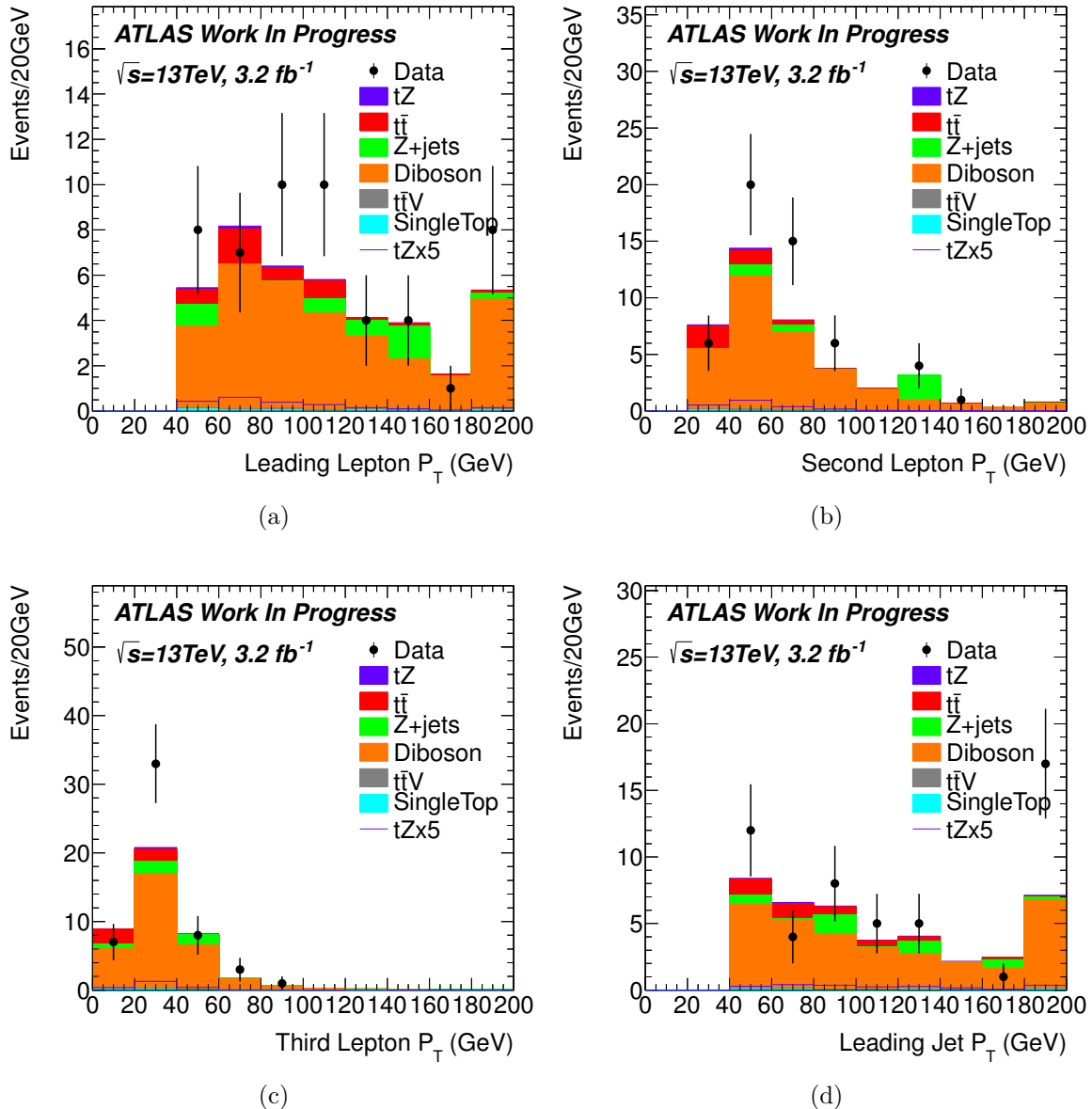


Figure 6.8: Distributions of transverse momenta for (a) the leading lepton, (b) the second lepton, (c) the third lepton, and (d) the leading jet in the control region for Diboson.

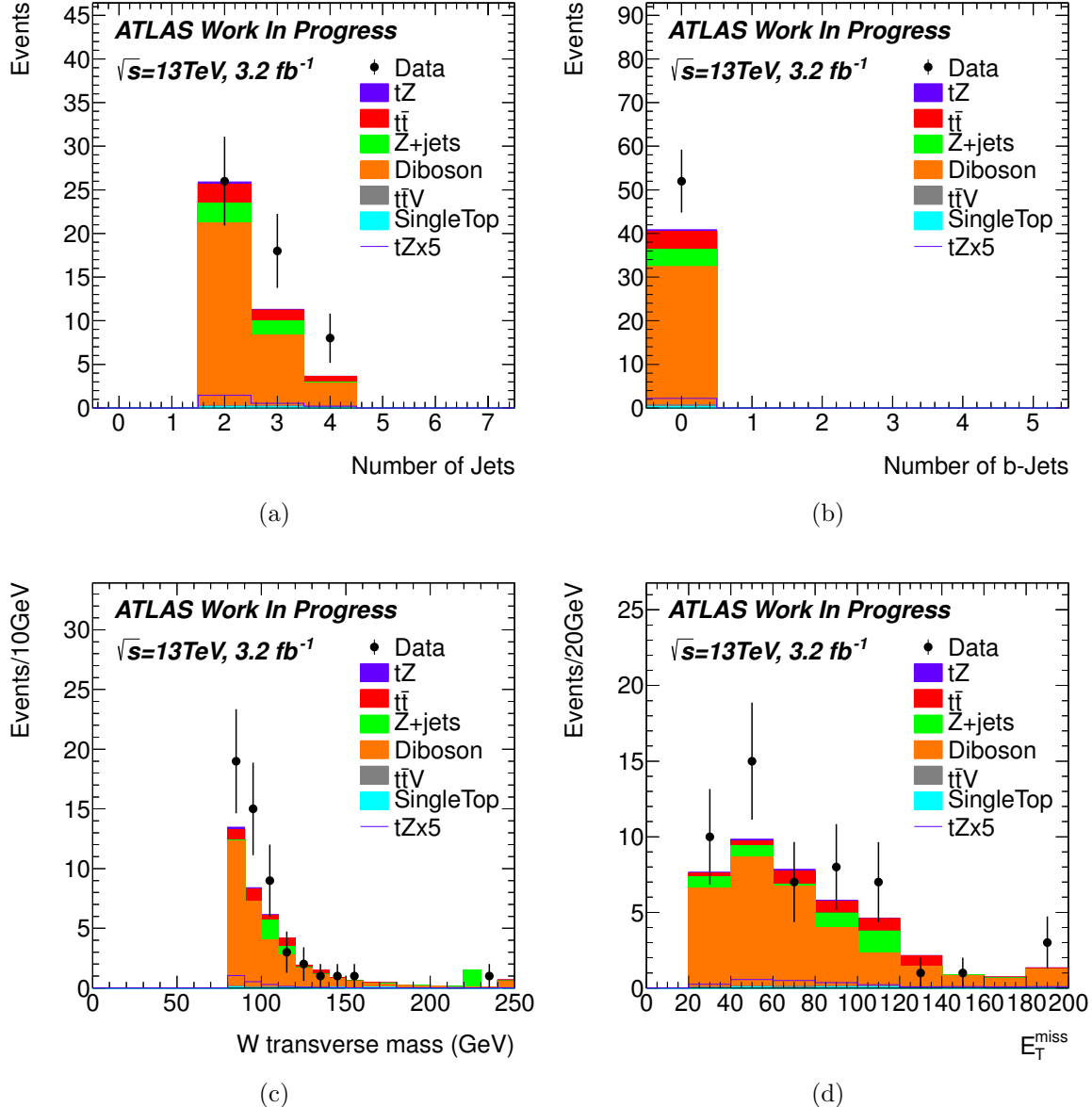


Figure 6.9: Distributions of (a) jet multiplicity, (b)  $b$ -jet multiplicity, (c)  $m_W^T$ , and (d)  $E_T^{\text{miss}}$  in the control region for Diboson.

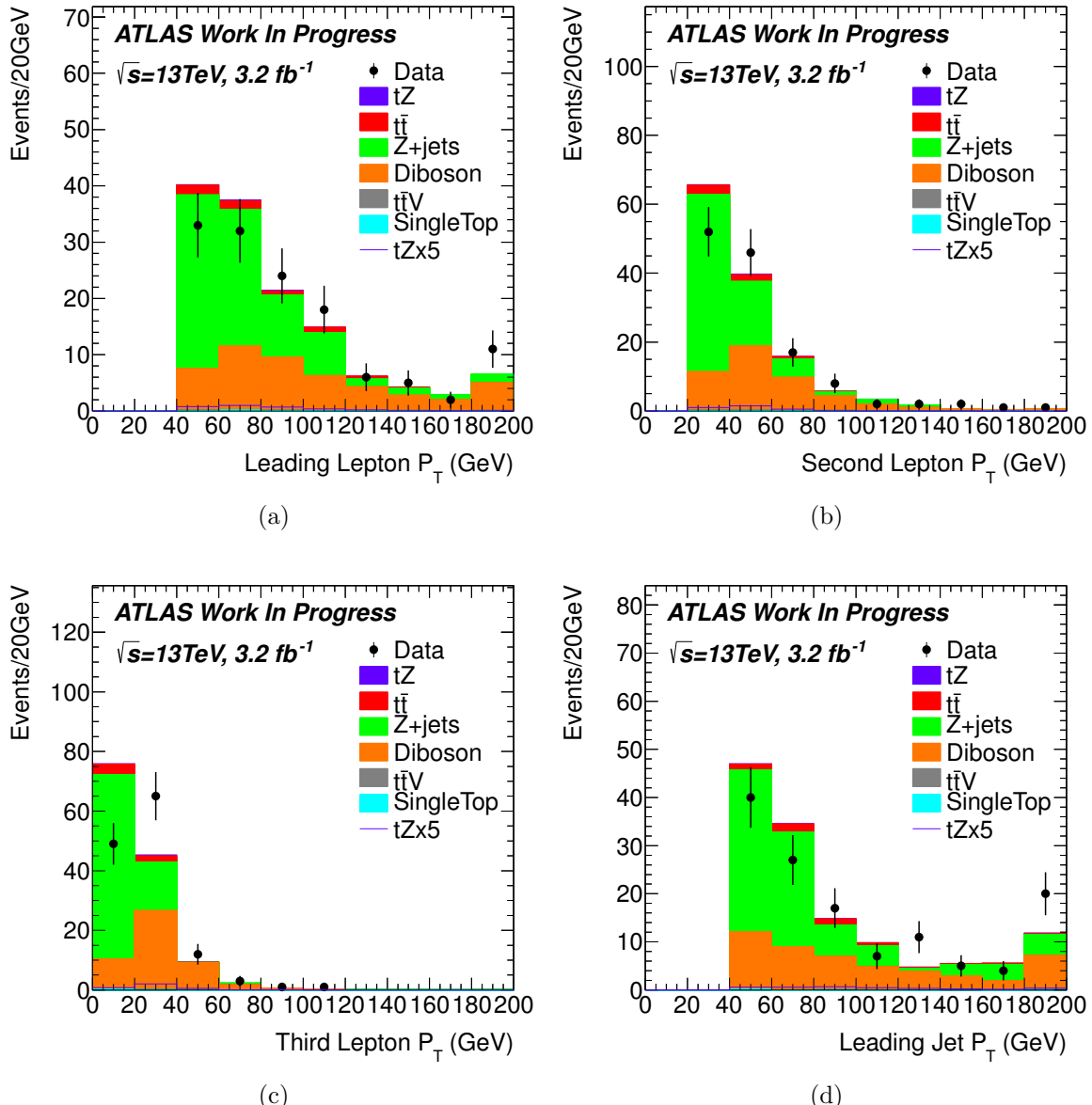


Figure 6.10: Distributions of transverse momenta for (a) the leading lepton, (b) the second lepton, (c) the third lepton, and (d) the leading jet in the control region for  $Z+jets$ .

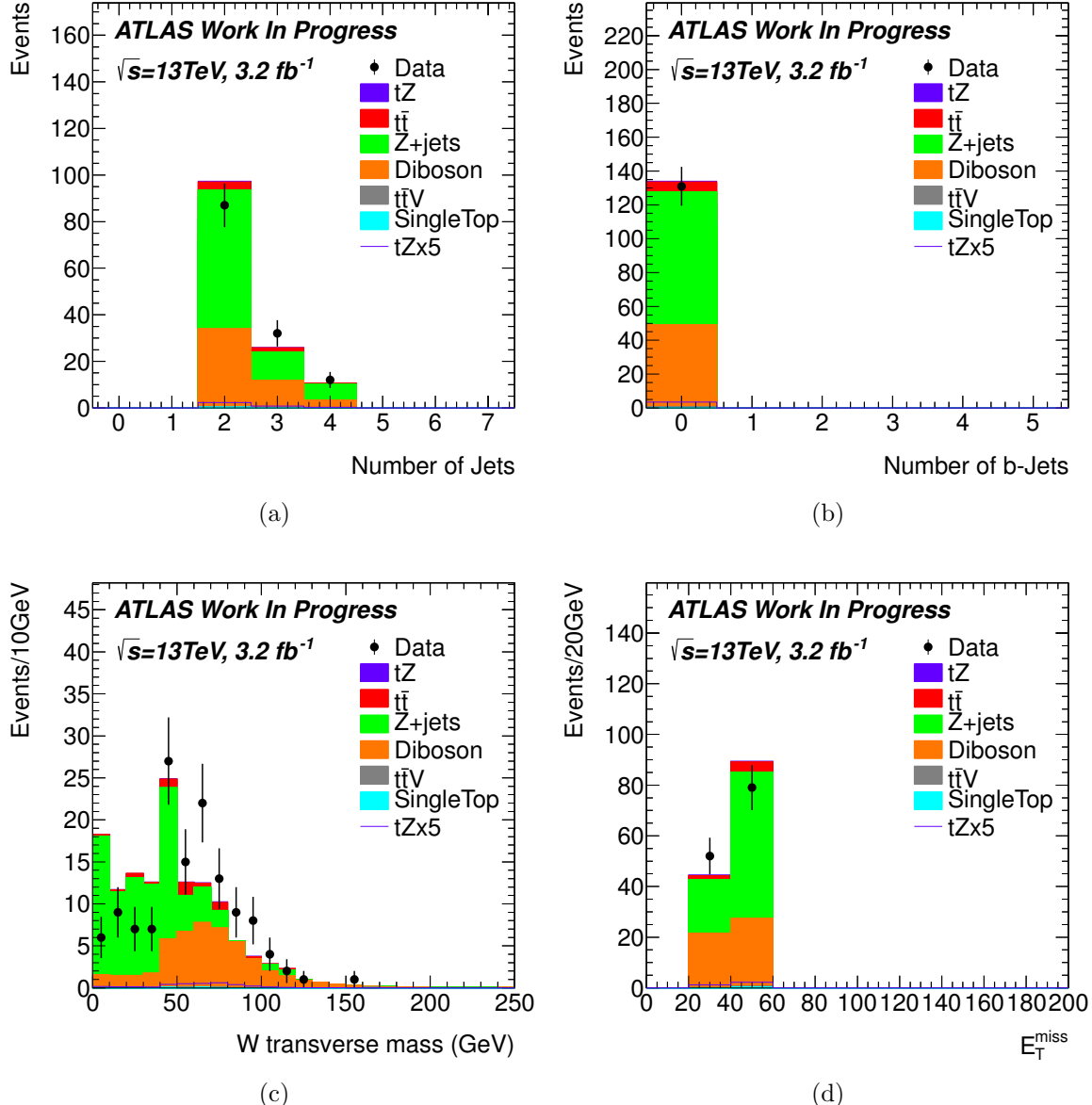


Figure 6.11: Distributions of (a) jet multiplicity, (b)  $b$ -jet multiplicity, (c)  $m_W^T$ , and (d)  $E_T^{\text{miss}}$  in the control region for  $Z + \text{jets}$ .

### 6.3 Cut Flow

Once the preselection region is defined, our goal is to improve the sensitivity of the analysis. We do this by searching for kinematic variables where the shape of the signal distribution significantly differs from the shape of one or all of the background distributions and evaluating its effect on the value  $S/\sqrt{B}$ . The variable  $S/\sqrt{B}$  is used to optimize because it ensures both strong signal to background ratios while also ensuring that we limit the contribution of statistical errors. Many distributions are considered for their background rejection, and/or physical motivations but distributions of special interest are the angular variables and top-quark mass shown in Figure 6.16 because they display the properties of the top quark. The polarization of the top quark is most notable in Figure 6.16 where the optimal basis shows both  $t\bar{t}$  and  $tZ$  have a distribution favoring values closer to 1, while Diboson is comparatively flat. In principle these variables could be used to distinguish backgrounds without a top quark from the signal which does. In practice the discrimination power of these variables is not as strong as that of others. The variables with the best discriminating power are shown in Table 6.2 and are,

- $m_T^W > 50$  GeV. This selects for events with higher energy  $W$  bosons.
- Leading non- $b$ -jet  $|\eta| > 1.5$ . This selects for events with a forward jet as is the case with single top  $t$ -channel and  $tZ$ .
- $\Delta R$  between the  $b$ -jet and Leading non- $b$ -jet  $> 2.5$ .  $\Delta R$  is calculated as the  $\Delta\eta$  and the  $\Delta\phi$  added in quadrature. These two objects are expected to not be near each other in the signal selecting for events where the jets do not both come from the same source.

The distributions of these variables are shown in Figure 6.12 and are re-optimized sequentially to show that any correlations are minor, and to ensure optimal sensitivity. Table 6.2 also shows what background each cut is preferentially removing. The  $m_T^W$  cut targets  $Z + \text{jets}$ , while also eliminating  $t\bar{t}$  and some Diboson. The cut on the leading non- $b$ -jet  $\eta$  is less obviously targeted at a specific background, but is removing approximately half of all backgrounds while removing comparatively little signal. This is due to the forward jet, a characteristic kinematic property of single top-quark production. The cut on the  $\Delta R$  between the  $b$ -jet and leading non- $b$ -jet performs well because the  $b$ -jet and the leading non- $b$ -jet are coming from opposite legs of the hard interaction. This creates a distribution where the top quark and its decay products (in this case the  $b$ -jet) come out preferentially far apart in  $\Delta R$  in the signal compared to the backgrounds.

Process	Preselection	$m_T^W$	Leading-non $b$ -jet $\eta$	full selection
$t\bar{t}$	45	28	15	$10 \pm 45\%$
single top quark	1.4	1.0	0.49	$0.34 \pm 66\%$
$tV$	4.4	3.1	1.0	$0.61 \pm 66\%$
$Z + \text{jets}$	32	5.3	2.3	$1.7 \pm 413\%$
Diboson	18	13	5.2	$3.3 \pm 32\%$
$tZ$	5.7	4.3	3.2	$2.9 \pm 11\%$
Total Expected	108	55	27	$19 \pm 71\%$
Data Observed	108	62	29	22
S/B	0.06	0.08	0.13	0.18
S/ $\sqrt{B}$	0.57	0.60	0.66	0.71

Table 6.2: Event yields after selection cuts are applied. Uncertainties provided on the final selection are the uncertainties described in Chapter 7 taken in quadrature for each sample.

Once we have applied the full cut flow, we are left with the remaining distributions to analyze. These represent the kinematic properties of events selected by this analysis which are shown in Figures 6.13 and 6.14. The application of the full selection takes us from an  $S/B$  of 0.06 to 0.18. These efforts are to improve the sensitivity of our analysis as shown in the next chapter. There is reasonable agreement throughout the signal region, and in  $p_T$  distributions

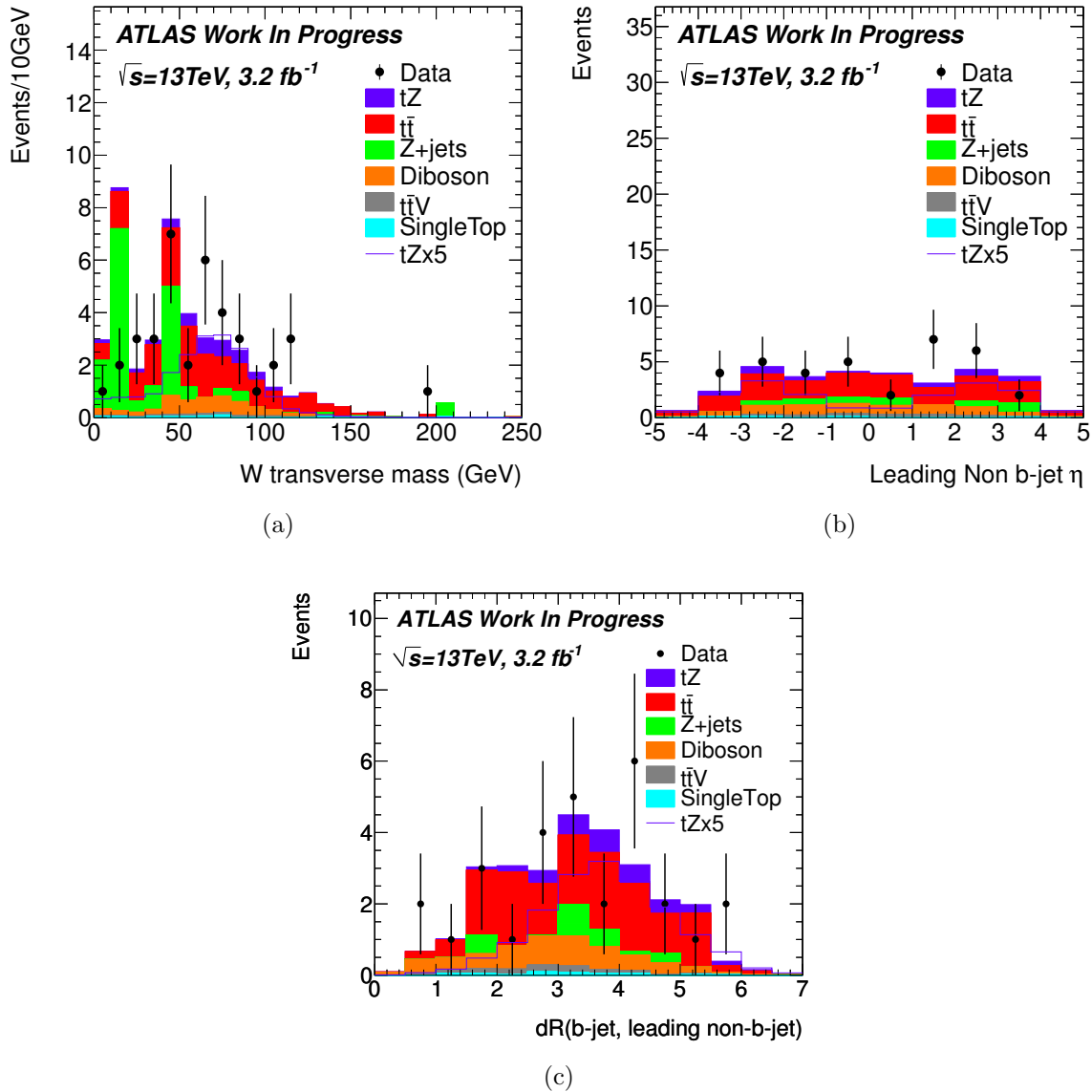


Figure 6.12: Distributions of (a)  $m_T^W$  which is required to be  $> 50$  GeV, (b) the  $\eta$  of the leading non b-tagged jet which is required to be  $> 1.5$ , and (c) the  $\Delta R$  between the  $b$ -jet and leading non- $b$ -jet which is required to be  $> 2.5$ . Each has the entire selection applied except the variable plotted to view the full distribution.

it can be seen that the signal peaks higher when the cuts are placed. These cuts were chosen because they optimized  $S/\sqrt{B}$  which in this case prioritized preserving statistics over improving signal purity. With more data collected these cuts could be tightened to further improve  $S/\sqrt{B}$ .

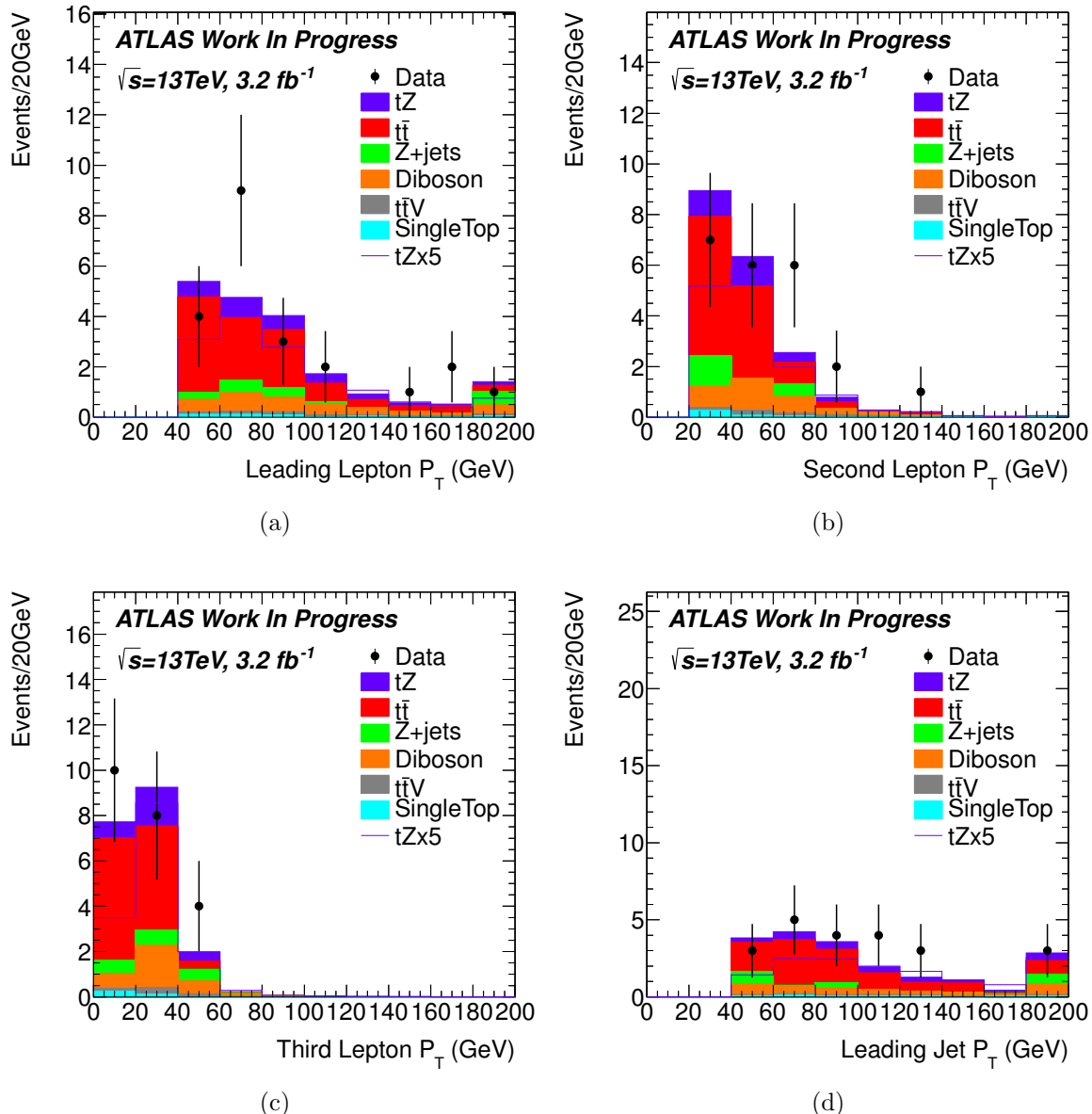


Figure 6.13: Distributions of transverse momenta for (a) the leading lepton, (b) the second lepton, (c) the third lepton, and (d) the leading jet in the signal region.

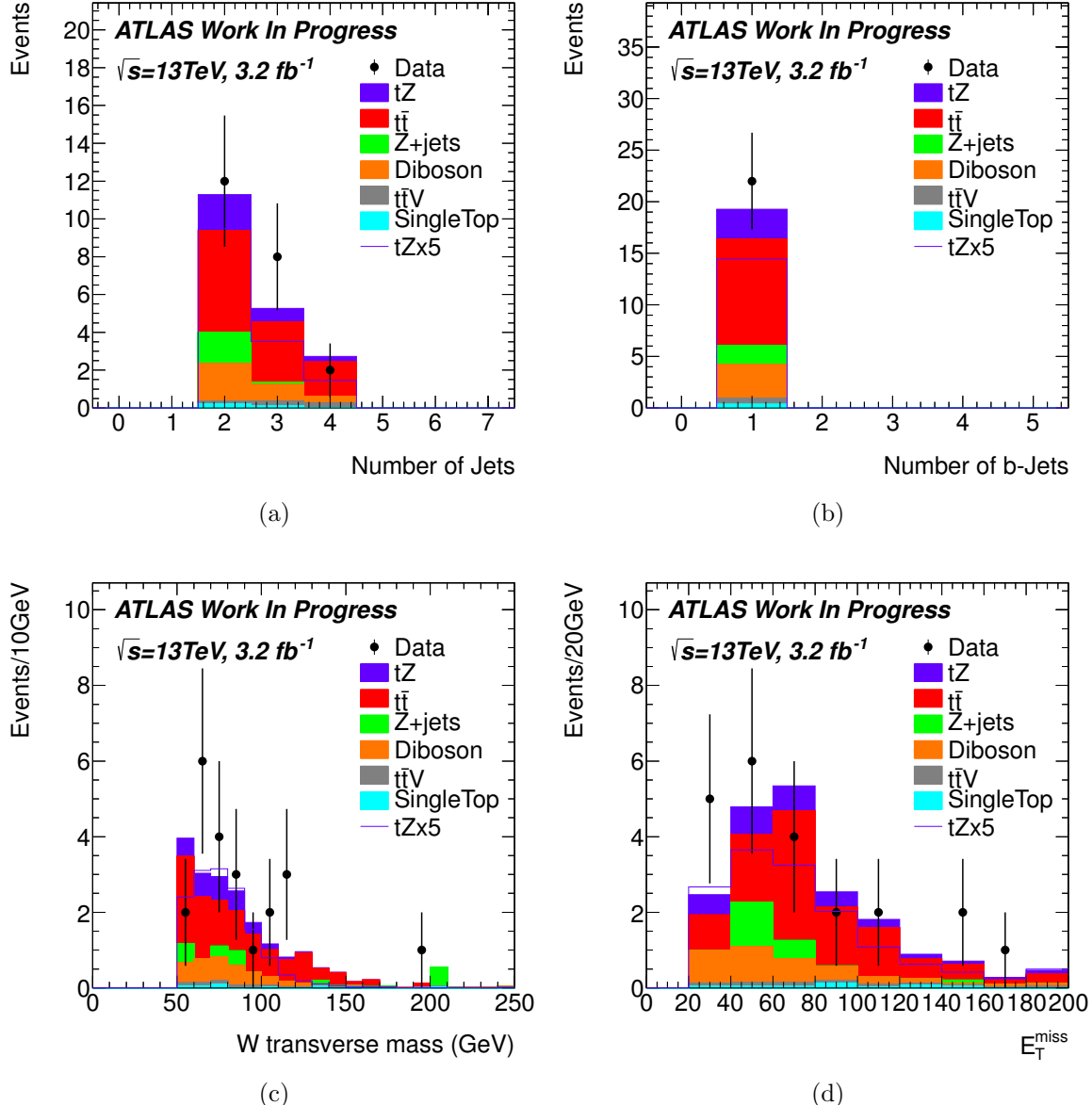


Figure 6.14: Distributions of (a) jet multiplicity, (b)  $b$ -jet multiplicity, (c)  $m_W^T$ , and (d)  $E_T^{\text{miss}}$  in the signal region.

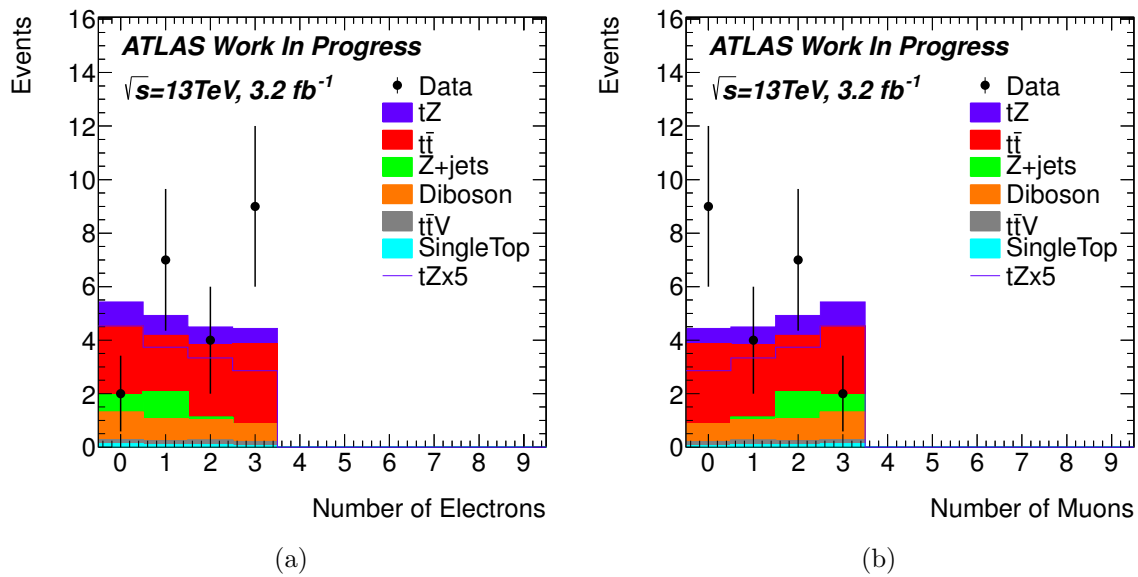


Figure 6.15: (a) Number of electrons and (b) number of muons.

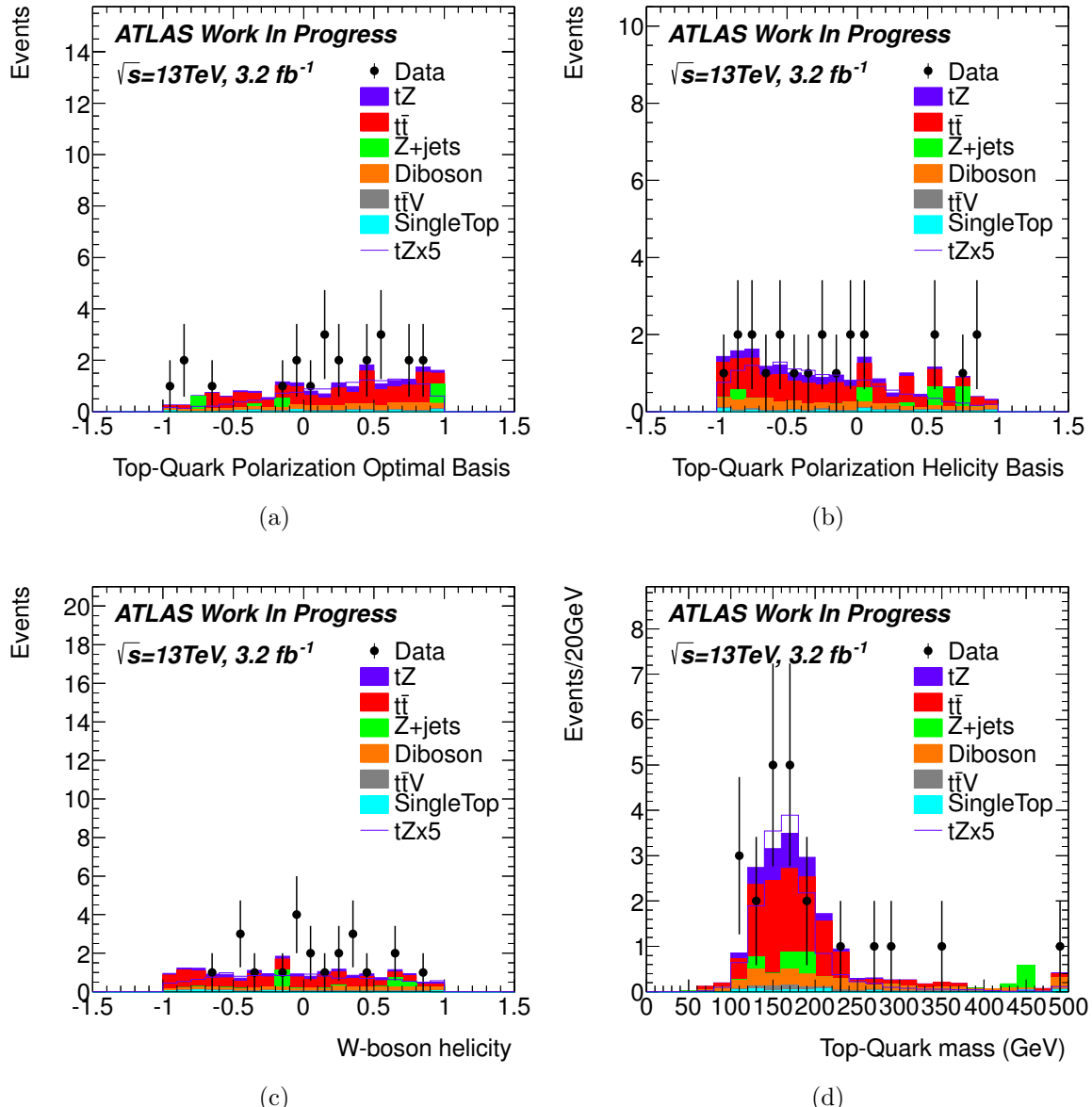


Figure 6.16: Distributions of the top-quark polarization in the (a) Optimal basis and (b) the helicity basis, (c) the  $W$ -boson helicity, and (d) the mass of the top quark.

# Chapter 7

## Results

Bayesian address the question everyone is interested in by using assumptions no one believes.

Frequentest use impeccable logic to deal with an issue of no interest to anyone. - L.Lyons

A single bin profile likelihood calculation is performed to extract limits on the  $tZ$  cross-section at the 95% confidence limit using roostats [119]. Profile likelihood calculations can produce confidence intervals on non-normal distributions more accurately than maximum or partial likelihood functions [120] and for this reason they have become a popular statistical method for high energy physics. However, before we can do this evaluation, a series of systematic uncertainties must be addressed and evaluated. The expected sensitivity to larger data-sets from the LHC is also evaluated.

### 7.1 Systematic Uncertainties

Systematic uncertainties on the object reconstruction, event reconstruction, normalization, and theoretical modeling affect the acceptance and expected event yield for each source. Tables 7.1 and 7.2 contain evaluated uncertainties. Some uncertainties are symmetric in nature, while others have distinct up and down variations. Nearly all uncertainties have been symmetrized either because of practical reasons (their effect is small so we can simplify them or they happen to come out symmetric) or for theoretical reasons (there is a physical

motivation for them to be symmetric). For these symmetric systematic uncertainties both up and down variations are considered and the greater of the two is used [121].

- Luminosity - The uncertainty on the integrated luminosity is  $\pm 2.1\%$ . It is obtained from Van Der Meer scans are performed in which the beam positions in the  $x-y$  plane are varied [122, 123].
- Pile Up - Pile up is discussed briefly in Chapter 3. Here we need to evaluate how well we estimate the degree to which pile up interferes with our ability to distinguish events from each other. This is one of the few uncertainties that was not symmetrized having different uncertainties for the up and down variations [124].
- Lepton efficiency scale factors - Leptons from our simulated Monte Carlo samples are needed to replicate our data in identification criteria (Electron ID, Muon ID Systematic, and Muon ID Statistics), isolation criteria, and trigger simulation (Electron Trigger, Muon Trigger). A prescription for how to assess this uncertainty is provided by the EGamma (which evaluates electrons and photons) and Muon groups which are derived from  $Z- > \ell\ell$  samples. [109, 125]
- Electron calibration - Electron momentum scale (Electron Scale) and resolution (Electron Resolution) are handled separately from lepton efficiency scale factors. Scale corrections are derived for data and smearing corrections for Monte Carlo. These corrections assess the systematic uncertainties associated with the processing of photons, and in this case, electrons [126].
- Muon calibration - Muon momentum scale and resolution are handled separately from lepton efficiency scale factors. Muon track identification (Muon track ID), transverse

momentum scale (Muon Scale), and resolution (Muon Resolution) are corrected as well as [125].

- $E_T^{\text{miss}}$  calibration - Lepton and jet energy and momentum scale and resolution uncertainties propagate into calculations of  $E_T^{\text{miss}}$  (giving MET Scale and MET Resolution).

How we include soft tracks into this calculation corresponds to a source of uncertainty [127].

- Jet energy scale (JES) - JES and its uncertainty are derived combining information from test-beam data, collision data, and simulation. The JES uncertainty is split into several orthogonal components using *insitu* techniques resulting in independent effective uncertainties. This is determined with 8 TeV data and extrapolated to 13 TeV running conditions [128].
- Jet energy resolution (JER) - The precision with which a jet's energy is measured has an uncertainty associated with it. A mis-modeling of this energy resolution can lead to varying acceptances in final state kinematics [128, 129].
- $b$ -jet tagging -  $b$ -tagging scale factors are used on a per-event basis to correct  $b$ -tagging efficiency. This is determined with 8 TeV data and extrapolated to 13 TeV running conditions using three independent eigenvectors for the efficiency of  $b$ -jets,  $c$ -jets, and light jets as well as two parameters to account for the extrapolation from 8 to 13 TeV [130].
- Initial-state radiation and final-state radiation (ISR/FSR) - ISR/FSR is evaluated on the  $t\bar{t}$  sample by varying the renormalization and factorization scales up and down by a factor of two from the nominal value of 1. This process is done to  $t\bar{t}$  because it is the dominant background to single top analyses and is small when compared to other

uncertainties that affect the other backgrounds.

- NLO subtraction - The uncertainties of how the NLO subtraction method is applied is evaluated on the  $t\bar{t}$  sample. Powheg and aMC@NLO are two tools that are used to calculate higher order corrections. A comparison of the two tools applied to  $t\bar{t}$  is used to estimate this uncertainty.
- Parton showering (PS) and Hadronization - The uncertainty on parton showering and hadronization is evaluated by comparing the cluster model in Herwig and the Lund string model in Pythia applied to  $t\bar{t}$ . A comparison of the two techniques implemented in these tools is used to estimate the uncertainty on this process.
- Parton Distribution Function (PDF) - The uncertainties that come from the choice of PDF is evaluated on the  $t\bar{t}$  sample by comparing PDF4LHC15 and CT10.
- Normalization - Normalization uncertainties for Diboson and  $Z+jets$  are estimated from control regions. For  $t\bar{t}$  [131], single top [132], and  $t\bar{t}Z$  [133], theory uncertainties on scale variations, PDF, and top-quark mass are used.
- MC Statistics - The uncertainty due to limited statistics in our simulated samples is assessed by taking the sum of the square of the weights of each event in each sample. When selecting for a narrow piece of phase space in order to look for small signals as is done in this analysis, it becomes increasingly difficult to both separate signal from background and maintain meaningful statistics both for MC and data.

Systematics	$t\bar{t}$	Other Top	$Z + \text{jets}$	Diboson	$tZ$	background total
Pile Up UP	-11%	64%	94%	10%	-2.4%	5.8%
Pile Up DOWN	2.1%	-13%	6.8%	1.8%	0.69%	1.3%
Normalization	$\pm 5.5\%$	$\pm 10\%$	$\pm 20\%$	$\pm 20\%$	$\pm -$	$\pm 10\%$
MC Statistics	$\pm 8.3\%$	$\pm 9.2\%$	$\pm 47\%$	$\pm 3.0\%$	$\pm 1.6\%$	$\pm 9.9\%$
PDF	$\pm 4.3\%$	-	-	-	-	$\pm 2.3\%$
PS and Hadronization	$\pm 0.86\%$	-	-	-	-	$\pm 0.46\%$
NLO subtraction	$\pm 20\%$	-	-	-	-	$\pm 11\%$
ISR/FSR RadLo	27%	-	-	-	-	14%
ISR/FSR RadHi	-24%	-	-	-	-	-11%

Table 7.1: Systematic uncertainties related to background normalization and theory modeling. Other Top is the combination of  $t\bar{t}V$  and single top.

Systematics	$t\bar{t}$	Other Top	$Z + \text{jets}$	Diboson	$tZ$	background total
Muon ID Systematic	$\pm 0.57\%$	$\pm 0.90\%$	$\pm 1.1\%$	$\pm 0.90\%$	$\pm 1.0\%$	$\pm 0.77\%$
Muon ID Statistics	$\pm 0.48\%$	$\pm 0.90\%$	$\pm 0.57\%$	$\pm 0.60\%$	$\pm 0.69\%$	$\pm 0.570\%$
Electron ID	$\pm 2.6\%$	$\pm 1.8\%$	$\pm 1.1\%$	$\pm 1.5\%$	$\pm 1.7\%$	$\pm 2.1\%$
Electron Trigger	$\pm 2.1\%$	$\pm 5.4\%$	$\pm 6.8\%$	$\pm 1.8\%$	$\pm 0.69\%$	$\pm 1.3\%$
Electron Reconstruction	$\pm 1.2\%$	$\pm 0.90\%$	$\pm 1.1\%$	$\pm 0.90\%$	$\pm 0.69\%$	$\pm 1.0\%$
Electron Scale	$\pm 1.7\%$	$\pm 3.8\%$	$\pm 0\%$	$\pm 1.2\%$	$\pm 0\%$	$\pm 0.99\%$
Electron Resolution	$\pm 0.86\%$	$\pm 2.9\%$	$\pm 0\%$	$\pm 0.30\%$	$\pm 0.34\%$	$\pm 0.72\%$
Muon Scale	$\pm 0.48\%$	$\pm 2.1\%$	$\pm 0.57\%$	$\pm 0.60\%$	$\pm 0.69\%$	$\pm 0.57\%$
Muon Resolution	$\pm 0.48\%$	$\pm 7.0\%$	$\pm 2.8\%$	$\pm 0.90\%$	$\pm 0.69\%$	$\pm 0.41\%$
Muon track ID	$\pm 1.3\%$	$\pm 1.9\%$	$\pm 0.57\%$	$\pm 0.60\%$	$\pm 0.69\%$	$\pm 0.82\%$
MET Scale	$\pm 0.67\%$	$\pm 0\%$	$\pm 0\%$	$\pm 0.60\%$	$\pm 0.34\%$	$\pm 0.46\%$
MET Resolution	$\pm 1.3\%$	$\pm 0\%$	$\pm 0\%$	$\pm 0\%$	$\pm 0.34\%$	$\pm 0.77\%$
JER	$\pm 4.7\%$	$\pm 4.5\%$	$\pm 130\%$	$\pm 8.4\%$	$\pm 1.40\%$	$\pm 10\%$
bTagSF $b$ -jets	$\pm 5.7\%$	$\pm 1.2\%$	$\pm 1.1\%$	$\pm 0.30\%$	$\pm 1.2\%$	$\pm 3.2\%$
bTagSF $c$ -jets	$\pm 0.48\%$	$\pm 1.3\%$	$\pm 6.0\%$	$\pm 10\%$	$\pm 0\%$	$\pm 2.0\%$
bTagSF light jets	$\pm 1.7\%$	$\pm 2.1\%$	$\pm 12\%$	$\pm 13\%$	$\pm 1.0\%$	$\pm 2.4\%$
JES 1 up	1.2%	-3.0%	150%	9.6%	0%	15%
JES 1 down	-4.7%	-3.0%	130%	8.4%	1.3%	10%
JES 2 up	0.76%	-2.1%	290%	4.5%	0.34%	27%
JES 2 down	-2.1%	-1.2%	0%	-3.4%	0%	-1.7%
JES 3 up	4.1%	-0.90%	190%	10%	0.69%	20.90%
JES 3 down	-4.6%	2.1%	0%	-10.0%	-0.69%	-4.1%

Table 7.2: Systematic uncertainties related to object identification, resolution, and scale. Other Top is the combination of  $t\bar{t}V$  and single top.

## 7.2 Statistical Analysis

Maximum likelihood ratio tests are among the most used methods in statistics because of their strength in hypothesis testing and generality. A popular variant of this method is the profile likelihood ratio test which considers nuisance parameters which are not of primary interest ( $\theta$ ) to be functions of the parameter which is of interest ( $\beta$ ). The parameter of interest,  $\beta$ , in this case is defined as the ratio of the measured cross section to the standard model cross section. The nuisance parameters,  $\theta$ , are measures of systematic uncertainties which are modeled by Gaussian statistics. By profiling we simplify the problem of finding  $\beta$  and  $\theta$  which optimizes the likelihood function in Equation 7.1 to constrain  $\theta = f(\beta)$  so that we can optimize Equation 7.2 which is often a preferable procedure when only one nuisance parameter is important.

$$\mathcal{L}(\beta, \theta | data) \tag{7.1}$$

$$\mathcal{L}(\beta, f(\beta) | data) \tag{7.2}$$

Because we have only one parameter which needs to be optimized for a profile likelihood fit is performed. This procedure is further simplified by only considering a distribution of a single bin. This simplification makes the profiling of the nuisance parameters easy, as each is simply a Gaussian, not dependent on the parameter of interest at all. These nuisance parameters are treated as correlated between sources of signal and background in the optimization procedure. The signal cross-section is then extracted from the likelihood function. The extracted cross-section measurement is  $\sigma_{tZ} = 448 \pm 672$  (stat)  $\pm 448$  (syst) fb.

This is 1.9 times the expected Standard Model cross-section of 236 fb which is due to the data excess over the expected background shown in Table 6.2. Because of the large uncertainties this is still in agreement with the standard model expectation. This corresponds to an upper bound at the 95% confidence limit on the  $tZ$  cross-section of  $\sigma_{tZ} = 1345$  fb. A lower bound can not be set due to large systematic uncertainties. The most notable systematic uncertainties in this analysis are the experimental uncertainties JES and JER, MC statistics for samples that have a mis-reconstructed lepton, and normalization uncertainties.

## 7.3 Outlook

In order to estimate the potential sensitivity to  $tZ$  with increased data collection, a series of simplified statistical analyses is performed. Systematic uncertainties are removed in order to see the effects of increased statistics in an idealized way. The expected yields obtained by this analysis are scaled up by a factor of 10 to estimate the expected precision of the cross-section measurement with the full 2016 data set, which corresponds to an integrated luminosity of approximately  $30 \text{ fb}^{-1}$ . The expected yields are then also scaled up by a factor of 100 in order to estimate the expected precision of the cross-section measurement with the full Run 2 and Run 3 data set, which corresponds to an integrated luminosity of approximately  $300 \text{ fb}^{-1}$ . When this is performed with the event yields of this analysis we can get an expected uncertainty on the cross-section of 150%. With the full 2016 data set the expected uncertainty drops to 50%. With the full set of run 2 data the expected uncertainty falls to 20%. This analysis is currently statistics limited, but with the full run 2 data set we will become systematics limited. The most immediate gains can be made from increasing MC statistics, with longer-term gains to be made from better understanding JES and JER. To

improve the sensitivity of this analysis, more complex multivariate analysis methods could be employed, the profile likelihood could be performed on a strong discriminating distribution, and/or control regions could be fit and included in the statistical analysis. Beyond that we will need to wait for the LHC to deliver more data in order to put further constraints on the  $tZ$  cross-section.

# Chapter 8

## Conclusion

The voyage of discovery is not in seeking new landscapes but in having new eyes. - Marcel Proust

An upper limit on the cross-section for  $tZ$  is measured using  $3.2 \text{ fb}^{-1}$  of data collected by the ATLAS detector at  $\sqrt{s} = 13 \text{ TeV}$ . Events are selected using a series of selection cuts which select for three leptons, between 2 and 4 jets,  $E_T^{\text{miss}}$ , and 1  $b$ -tag. A profile likelihood is performed in order to make a measurement of the  $tZ$  cross-section. The extracted cross-section measurement is  $\sigma_{tZ} = 448 \pm 672 \text{ (stat)} \pm 448 \text{ (syst)} \text{ fb}$ . The resulting upper limit is consistent with the standard model prediction with an exclusion of  $\sigma_{tZ} = 1345 \text{ fb}$  at the 95% confidence level.

## **BIBLIOGRAPHY**

## BIBLIOGRAPHY

- [1] N. Kidonakis, *Top quark pair and single top production at Tevatron and LHC energies*, , 2010. arXiv:1008.2460 [hep-ph].
- [2] P. Kant, O. M. Kind, T. Kintscher, T. Lohse, T. Martini, S. Mlbitz, P. Rieck, and P. Uwer, *HatHor for single top-quark production: Updated predictions and uncertainty estimates for single top-quark production in hadronic collisions*, Comput. Phys. Commun. **191** (2015) 74–89, arXiv:1406.4403 [hep-ph].
- [3] K. Cranmer, *A fresh look for the standard model*, <http://theoryandpractice.org/2013/08/a-fresh-look-for-the-standard-model/#.V9Lx67MY200>, 2016.
- [4] The Economist online, *The Standard Model of high energy physics Years from concept to discovery*,  
<http://www.economist.com/blogs/graphicdetail/2012/07/daily-chart-1>, 2012.
- [5] A. Heinson, *Feynmann Diagrams for Top Physics Talks and Notes*,  
[http://www-d0.fnal.gov/Run2Physics/top/top\\_public\\_web\\_pages/top\\_feynman\\_diagrams.html](http://www-d0.fnal.gov/Run2Physics/top/top_public_web_pages/top_feynman_diagrams.html), 2011.
- [6] D. Binosi and L. Theul, *JaxoDraw: A graphical user interface for drawing Feynman diagrams*, Computer Physics Communications **161** (2004) no. 1-2, 76 – 86.  
<http://www.sciencedirect.com/science/article/pii/S0010465504002115>.
- [7] J. Campbell, R. K. Ellis, and R. Rontsch, *Single top production in association with a Z boson at the LHC*, Phys.Rev. **D87** (2013) 114006, arXiv:1302.3856 [hep-ph].
- [8] M. Benedikt, R. Cappi, M. Chanel, R. Garoby, M. Giovannozzi, S. Hancock, M. Martini, E. Mtral, G. Mtral, K. Schindl, and J. L. Vallet, *Performance of the LHC Pre-Injectors*, <https://cds.cern.ch/record/494746>, 2001.
- [9] M. Brice, *First LHC magnets installed. Installation du premier aimant du LHC*, <https://cds.cern.ch/record/834351>, 2005.
- [10] ATLAS Collaboration, *Updated Luminosity Determination in pp Collisions at  $\sqrt{s} = 7$  TeV using the ATLAS Detector*, ATLAS-CONF-2011-011 .  
<https://cds.cern.ch/record/1334563>.

- [11] M. Brice, *Installing the ATLAS calorimeter. Vue centrale du dtecteur ATLAS avec ses huit toroïdes entourant le calorimtre avant son dplacement au centre du dtecteur*, <https://cds.cern.ch/record/910381>, 2005.
- [12] J. Pequenao, *Computer generated image of the whole ATLAS detector*, <https://cds.cern.ch/record/1095924>, 2008.
- [13] J. Pequenao and P. Schaffner, *An computer generated image representing how ATLAS detects particles*, <https://cds.cern.ch/record/1505342>, 2013.
- [14] ATLAS Collaboration, *The ATLAS Experiment at the CERN Large Hadron Collider*, JINST **3** (2008) S08003.
- [15] A. Salzburger, *The ATLAS Track Extrapolation Package*, ATL-SOFT-PUB-2007-005. ATL-COM-SOFT-2007-010, CERN, Geneva, 2007.  
<https://cds.cern.ch/record/1038100>.
- [16] J. Pequenao, *Computer generated image of the ATLAS inner detector*, CERN-GE-0803014 (2008) . <https://cds.cern.ch/record/1095926>.
- [17] *Early Inner Detector Tracking Performance in the 2015 data at  $\sqrt{s} = 13$  TeV*, ATL-PHYS-PUB-2015-051 (2015) no. ATL-PHYS-PUB-2015-051, .  
<http://cds.cern.ch/record/2110140>.
- [18] J. Pequenao, *Computer Generated image of the ATLAS calorimeter*, 2008.
- [19] J. Pequenao, *Computer generated image of the ATLAS Muons subsystem*, <https://cds.cern.ch/record/1095929>, 2008. CERN-GE-0803017 (2008) .
- [20] C. Marcelloni, *Installation of the first of the big wheels of the ATLAS muon spectrometer, a thin gap chamber (TGC) wheel. Installation de la premire des grandes roues du ATLAS spectromtre muons, une roue TGC*, CERN-EX-0609016 .  
<https://cds.cern.ch/record/986163>.
- [21] R. Bielski, *The ATLAS Muon Trigger Performance in Run I and Initial Run II Performance*, . <https://cds.cern.ch/record/2055529>.
- [22] M. Backes, A. Ruiz-Martinez, S. D. Jones, F. Monticelli, and J. Hoya, *Electron/photon trigger efficiency plots for ICHEP2016*, ATL-COM-DAQ-2016-086, CERN, 2016. <https://cds.cern.ch/record/2200359>.

- [23] A. Coccaro, *Track Reconstruction and b-Jet Identification for the ATLAS Trigger System*, J. Phys. Conf. Ser. **368** (2012) 012034, [arXiv:1112.0180 \[hep-ex\]](#).
- [24] D. Griffiths, *Introduction to Elementary Particles*. Wiley-VCH Verlag GmbH & Co. KGaA, Weinheim, 2004.
- [25] M. E. Peskin and D. V. Schroeder, *An Introduction to Quantum Field Theory*. Westview Press, 1995.
- [26] C. Itzykson and J.-B. Zuber, *Quantum Field Theory*. McGraw-Hill, 1980.
- [27] ATLAS Collaboration, *Observation of a new particle in the search for the Standard Model Higgs boson with the ATLAS detector at the LHC*, Phys. Lett. **B716** (2012) 1–29, [arXiv:1207.7214 \[hep-ex\]](#).
- [28] J. A. Gallian, *Contemporary Abstract Algebra*. Houghton Mifflin Company, 2002.
- [29] W.-K. Tung, *Group Theory in Physics*. World Scientific Publishing Co. Pte. Ltd., 1985.
- [30] Particle Data Group. Berkeley Collaboration, T.M. Liss, F. Maltoni, and A. Quadt, *The Top Quark*, J. Phys. G (2010) .
- [31] M. Jezabek J. Kuhn, *Top quark width: Theoretical update*, Phys. Rev. D **48** (1993) .
- [32] CDF Collaboration, T. Aaltonen et al., *Direct Top-Quark Width Measurement CDF*, Phys. Rev. Lett. **105** (2010) 232003, [arXiv:1008.3891 \[hep-ex\]](#).
- [33] D0 Collaboration, V. M. Abazov et al., *Determination of the width of the top quark*, Phys. Rev. Lett. **106** (2011) 022001, [arXiv:1009.5686 \[hep-ex\]](#).
- [34] D0 Collaboration, V. M. Abazov et al., *An Improved determination of the width of the top quark*, Phys. Rev. **D85** (2012) 091104, [arXiv:1201.4156 \[hep-ex\]](#).
- [35] A. Heinson, A. S. Belyaev, and E. E. Boos, *Single top quarks at the Fermilab Tevatron*, Phys. Rev. **D56** (1997) 3114–3128, [arXiv:hep-ph/9612424 \[hep-ph\]](#).
- [36] CDF Collaboration, F. Abe et al., *Observation of top quark production in  $\bar{p}p$  collisions*, Phys. Rev. Lett. **74** (1995) 2626–2631, [arXiv:hep-ex/9503002 \[hep-ex\]](#).

- [37] D0 Collaboration, S. Abachi et al., *Observation of the top quark*, Phys. Rev. Lett. **74** (1995) 2632–2637, [arXiv:hep-ex/9503003 \[hep-ex\]](https://arxiv.org/abs/hep-ex/9503003).
- [38] D0 Collaboration, V. M. Abazov et al., *Observation of Single Top Quark Production*, Phys. Rev. Lett. **103** (2009) 092001, [arXiv:0903.0850 \[hep-ex\]](https://arxiv.org/abs/0903.0850).
- [39] CDF Collaboration, T. Aaltonen et al., *First Observation of Electroweak Single Top Quark Production*, Phys. Rev. Lett. **103** (2009) 092002, [arXiv:0903.0885 \[hep-ex\]](https://arxiv.org/abs/0903.0885).
- [40] ATLAS Collaboration, *Search for anomalous couplings in the  $Wtb$  vertex from the measurement of double differential angular decay rates of single top quarks produced in the  $t$ -channel with the ATLAS detector*, JHEP **04** (2016) 023, [arXiv:1510.03764 \[hep-ex\]](https://arxiv.org/abs/1510.03764).
- [41] ATLAS Collaboration, *Comprehensive measurements of  $t$ -channel single top-quark production cross sections at  $\sqrt{s} = 7$  TeV with the ATLAS detector*, Phys. Rev. **D90** (2014) no. 11, 112006, [arXiv:1406.7844 \[hep-ex\]](https://arxiv.org/abs/1406.7844).
- [42] ATLAS Collaboration, *Measurement of the  $t$ -channel single top-quark production cross section in  $pp$  collisions at  $\sqrt{s} = 7$  TeV with the ATLAS detector*, Phys. Lett. **B717** (2012) 330–350, [arXiv:1205.3130 \[hep-ex\]](https://arxiv.org/abs/1205.3130).
- [43] CMS Collaboration, *Measurement of the  $t$ -channel single top quark production cross section in  $pp$  collisions at  $\sqrt{s} = 7$  TeV*, Phys. Rev. Lett. **107** (2011) 091802, [arXiv:1106.3052 \[hep-ex\]](https://arxiv.org/abs/1106.3052).
- [44] F.-P. Schilling, *Top Quark Physics at the LHC: A Review of the First Two Years*, Int.J.Mod.Phys. **A27** (2012) 1230016, [arXiv:1206.4484 \[hep-ex\]](https://arxiv.org/abs/1206.4484).
- [45] ATLAS Collaboration, *Observation of  $t$  Channel Single Top-Quark Production in  $pp$  Collisions at  $\sqrt{s} = 7$  TeV with the ATLAS detector*, ATLAS-CONF-2011-088 (2011) . <https://cds.cern.ch/record/1356197>.
- [46] ATLAS Collaboration, *Measurement of the production cross-section of a single top quark in association with a  $W$  boson at 8 TeV with the ATLAS experiment*, JHEP **01** (2016) 064, [arXiv:1510.03752 \[hep-ex\]](https://arxiv.org/abs/1510.03752).
- [47] CMS Collaboration, *Observation of the associated production of a single top quark and a  $W$  boson in  $pp$  collisions at  $\sqrt{s} = 8$  TeV*, Phys. Rev. Lett. **112** (2014) no. 23, 231802, [arXiv:1401.2942 \[hep-ex\]](https://arxiv.org/abs/1401.2942).

- [48] ATLAS Collaboration, *Measurement of the  $t\bar{t}Z$  and  $t\bar{t}W$  production cross sections in multilepton final states using  $3.2 \text{ fb}^{-1}$  of  $pp$  collisions at 13 TeV at the LHC*, ATLAS-CONF-2016-003 . <https://cds.cern.ch/record/2138947>.
- [49] J. A. Dror, M. Farina, E. Salvioni, and J. Serra, *Strong  $tW$  Scattering at the LHC*, JHEP **01** (2016) 071, arXiv:1511.03674 [hep-ph].
- [50] UA1 Collaboration, G. Arnison et al., *Experimental Observation of Isolated Large Transverse Energy Electrons with Associated Missing Energy at  $s^{**}(1/2) = 540\text{-GeV}$* , Phys. Lett. **B122** (1983) 103–116. [,611(1983)].
- [51] UA1 Collaboration, G. Arnison et al., *Experimental Observation of Lepton Pairs of Invariant Mass Around  $95\text{-GeV}/c^{**2}$  at the CERN SPS Collider*, Phys. Lett. **B126** (1983) 398–410.
- [52] The LEP Collaborations and the LEP Electroweak Working Group, *A Combination of Preliminary Electroweak Measurements and Constraints on the Standard Model*, 1998.
- [53] T. J. Berners-Lee, *Information management: a proposal*, CERN-DD-89-001-OC, CERN, Geneva, 1989. <https://cds.cern.ch/record/369245>.
- [54] A. Variola, M. Amoretti, G. Bonomi, A. Boutcha, P. Bowe, C. Carraro, C. L. Cesar, M. Charlton, M. Doser, V. Filippini, A. Fontana, M. C. Fujiwara, R. Funakoshi, P. Genova, J. S. Hangst, R. S. Hayano, L. V. Jrgensen, V. Lagomarsino, R. Landua, D. Lindelf, E. Lodi-Rizzini, M. Macri, N. Madsen, G. Manuzio, P. Montagna, H. S. Pruys, C. Regenfus, A. Rotondi, P. Riedler, G. Testera, and D. P. Van der Werf, *Production and detection of cold anti-hydrogen atoms: A first step towards high precision CPT test*, AIP Conf. Proc. **698** (2003) 205–208.  
<https://cds.cern.ch/record/818451>.
- [55] ATLAS Collaboration, *Observation of a new particle in the search for the Standard Model Higgs boson with the ATLAS detector at the LHC*, Physics Letters B **716** (2012) no. 1, 1 – 29.  
<http://www.sciencedirect.com/science/article/pii/S037026931200857X>.
- [56] CMS Collaboration, *Observation of a new boson at a mass of 125 GeV with the CMS experiment at the LHC*, Physics Letters B **716** (2012) no. 1, 30 – 61.  
<http://www.sciencedirect.com/science/article/pii/S0370269312008581>.

- [57] S. Myers, *The LEP Collider, from design to approval and commissioning*. John Adams' Lecture. CERN, 1991. <http://cds.cern.ch/record/226776>. Delivered at CERN, 26 Nov 1990.
- [58] C. O'Luanaigh, *The Large Hadron Collider*, <http://cds.cern.ch/record/1998498>, 2014.
- [59] E. Boltezar, H. Haseroth, W. Pirkl, G. Plass, T. R. Sherwood, U. Tallgren, P. Ttu, D. Warner, and M. Weiss, *Performance of the new CERN 50 MeV linac*, IEEE Trans. Nucl. Sci. **26** (1979) no. CERN-PS-LR-79-15, 3674–3676.  
<https://cds.cern.ch/record/134670>.
- [60] B. Mikulec, A. Blas, C. Carli, A. Findlay, K. Hanke, G. Rumolo, and J. Tan, *LHC Beams from the CERN PS Booster*, in *Particle accelerator. Proceedings, 23rd Conference, PAC'09, Vancouver, Canada, May 4-8, 2009*, p. TU6PFP086. 2010.  
<http://accelconf.web.cern.ch/AccelConf/PAC2009/papers/tu6pfp086.pdf>.
- [61] M. Barnes, M. Benedikt, E. W. Blackmore, A. Blas, J. Borburgh, R. Cappi, M. Chanel, V. Chohan, F. Cifarelli, G. Clark, G. Daems, L. R. Evans, A. B. Fowler, R. Garoby, J. Gonzlez, D. G. Grier, J. Gruber, S. Hancock, C. E. Hill, A. Jansson, E. Jensen, S. R. Koscielniak, A. Krusche, R. Losito, P. Maesen, F. Mammarella, K. D. Metzmacher, A. Mitra, J. Olsfors, M. Paoluzzi, J. Pedersen, R. Poirier, U. Raich, K. W. Reiniger, T. C. Ries, J. P. Riunaud, J. P. Royer, M. Sassowsky, K. Schindl, H. O. Schnauer, L. Sermeus, M. Thivent, H. M. Ullrich, W. Van Cauter, M. Vretenar, and F. V. Vlker, *The PS complex as proton pre-injector for the LHC: design and implementation report*. CERN, Geneva, 2000.  
<https://cds.cern.ch/record/449242>.
- [62] P. Collier and B. Goddard, *Preparation of the SPS as LHC injector*, in *Particle accelerator. Proceedings, 6th European conference, EPAC'98, Stockholm, Sweden, June 22-26, 1998. Vol. 1-3*, pp. 335–337. 1998.  
<http://accelconf.web.cern.ch/AccelConf/e98/PAPERS/MOP03C.PDF>.
- [63] N. M. AB, *Press Release: The 1984 Nobel Prize in Physics*, . [http://www.nobelprize.org/nobel\\_prizes/physics/laureates/1984/press.html](http://www.nobelprize.org/nobel_prizes/physics/laureates/1984/press.html).
- [64] C. Bernardini, G. F. Corazza, G. Di Giugno, G. Ghigo, J. Haissinski, P. Marin, R. Querzoli, and B. Touschek, *Lifetime and Beam Size in a Storage Ring*, Phys. Rev. Lett. **10** (1963) 407–409.  
<http://link.aps.org/doi/10.1103/PhysRevLett.10.407>.

- [65] O. S. Brning, P. Collier, P. Lebrun, S. Myers, R. Ostojic, J. Poole, and P. Proudlock, *LHC Design Report*. CERN, Geneva, 2004. <https://cds.cern.ch/record/782076>.
- [66] V. Papadimitriou, *Luminosity determination at the Tevatron*, LHC Lumi Days (2011) 90–95, 1106.5182:<http://arxiv.org/abs/1106.5182v1>.
- [67] ATLAS Collaboration, *ATLAS Luminosity Public Results*, [https://twiki.cern.ch/twiki/bin/view/AtlasPublic/LuminosityPublicResults#Multiple\\_Year\\_Collision\\_Plots](https://twiki.cern.ch/twiki/bin/view/AtlasPublic/LuminosityPublicResults#Multiple_Year_Collision_Plots).
- [68] G. Bayatian, C. collaboration, et al., *The Compact Muon Solenoid Technical Proposal*, CERN/LHCC **94** (1994) 38.
- [69] ATLAS Collaboration, *Expected Performance of the ATLAS Experiment - Detector, Trigger and Physics*, arXiv:0901.0512 [hep-ex].
- [70] MoEDAL Collaboration, *Technical Design Report of the MoEDAL Experiment*, CERN-LHCC-2009-006. MoEDAL-TDR-001, 2009. <https://cds.cern.ch/record/1181486>.
- [71] TOTEM Collaboration, *Total cross-section, elastic scattering and diffraction dissociation at the Large Hadron Collider at CERN: TOTEM Technical Design Report*. Technical Design Report TOTEM. CERN, Geneva, 2004. <https://cds.cern.ch/record/704349>.
- [72] LHCf Collaboration, *LHCf experiment: Technical Design Report*. Technical Design Report LHCf. CERN, Geneva, 2006. <https://cds.cern.ch/record/926196>.
- [73] ALICE Collaboration, *The ALICE experiment at the CERN LHC*, Journal of Instrumentation **3** (2008) no. 08, S08002.
- [74] LHCb Collaboration, *The LHCb detector at the LHC*, Journal of Instrumentation **3** (2008) no. 08, S08005.
- [75] ATLAS Collaboration Collaboration, *ATLAS magnet system: Technical Design Report, 1.* Technical Design Report ATLAS. CERN, Geneva, 1997. <https://cds.cern.ch/record/338080>.
- [76] M. Capeans, G. Darbo, K. Einsweiller, M. Elsing, T. Flick, M. Garcia-Sciveres, C. Gemme, H. Pernegger, O. Rohne, and R. Vuillermet, *ATLAS Insertable B-Layer*

*Technical Design Report*, Tech. Rep. CERN-LHCC-2010-013. ATLAS-TDR-19, 2010.  
<https://cds.cern.ch/record/1291633>.

- [77] A. Miucci, *The ATLAS Insertable B-Layer project*, Journal of Instrumentation **9** (2014) no. 02, C02018. <http://stacks.iop.org/1748-0221/9/i=02/a=C02018>.
- [78] ATLAS Collaboration Collaboration, *ATLAS inner detector: Technical Design Report, 1.* Technical Design Report ATLAS. CERN, Geneva, 1997.  
<https://cds.cern.ch/record/331063>.
- [79] ATLAS Collaboration, *ATLAS pixel detector electronics and sensors*, Journal of Instrumentation **3** (2008) no. 07, P07007.
- [80] A. Abdesselam and T. Akimoto, *The Barrel Modules of the ATLAS SemiConductor Tracker*, ATL-INDET-PUB-2006-005. ATL-COM-INDET-2006-009. CERN-ATL-COM-INDET-2006-009, CERN, Geneva, 2006.  
<https://cds.cern.ch/record/974073>.
- [81] A. Abdesselam and F. Anghinolfi, *The ATLAS semiconductor tracker end-cap module*, Nucl. Instrum. Methods Phys. Res., A **575** (2007) no. 3, 353–389.
- [82] J. D. Jackson, *Classical Electrodynamics*. John Wiley & Sons, Inc., New Jersey, USA, 3 ed., 1991.
- [83] A. Bingl, *The ATLAS TRT and its Performance at LHC*, Journal of Physics: Conference Series **347** (2012) no. 1, 012025.
- [84] ATLAS Collaboration, *The ATLAS TRT barrel detector*, Journal of Instrumentation **3** (2008) no. 02, P02014.
- [85] ATLAS Collaboration, *The ATLAS TRT end-cap detectors*, Journal of Instrumentation **3** (2008) no. 10, P10003.
- [86] R. Wigmans, *Calorimetry - Energy Measurement in Particle Physics*. Oxford University Press, 2000.
- [87] ATLAS Collaboration Collaboration, *ATLAS tile calorimeter: Technical Design Report*. Technical Design Report ATLAS. CERN, Geneva, 1996.  
<https://cds.cern.ch/record/331062>.

- [88] J. Proudfoot, *Hadron Calorimetry at the LHC*, in *Proceedings, 34th SLAC Summer Institute on Particle Physics: The Next Frontier: Exploring with the LHC (SSI 2006): Menlo Park, California, July 17-28, 2006.* 2006.  
<http://www.slac.stanford.edu/econf/C060717/proceedings.htm>.
- [89] B. Aubert et. al., *Construction, assembly and tests of the ATLAS electromagnetic barrel calorimeter*, Nuclear Instruments and Methods in Physics Research Section A: Accelerators, Spectrometers, Detectors and Associated Equipment **558** (2006) no. 2, 388 – 418.
- [90] ATLAS Electromagnetic Liquid Argon Endcap Calorimeter Group, *Construction, assembly and tests of the ATLAS electromagnetic end-cap calorimeters*, Journal of Instrumentation **3** (2008) no. 06, P06002.
- [91] M.L Andrieux et. al., *Construction and test of the first two sectors of the ATLAS barrel liquid argon presampler*, Nuclear Instruments and Methods in Physics Research Section A: Accelerators, Spectrometers, Detectors and Associated Equipment **479** (2002) no. 2-3, 316 – 333.
- [92] A. E. B. Calorimeter, *Energy linearity and resolution of the ATLAS electromagnetic barrel calorimeter in an electron test-beam*, Nucl. Instrum. Meth. **A568** (2006) 601–623, [arXiv:physics/0608012 \[physics\]](https://arxiv.org/abs/physics/0608012).
- [93] ATLAS Collaboration, *Data-driven determination of the energy scale and resolution of jets reconstructed in the ATLAS calorimeters using dijet and multijet events at  $\sqrt{s} = 8 \text{ TeV}$* , ATLAS-CONF-2015-017 . <https://cds.cern.ch/record/2008678>.
- [94] D. Green, *At the leading edge: the ATLAS and CMS LHC experiments*. World Scientific, Singapore, 2010.
- [95] T. Ferbel, *Experimental Techniques in High Energy Physics*. Addison-Wesley Publishing Company, Inc., 1987.
- [96] ATLAS Collaboration, *ATLAS detector and physics performance: Technical Design Report, 1.* Technical Design Report ATLAS. CERN, 1999.  
<https://cds.cern.ch/record/391176>.
- [97] ATLAS Collaboration Collaboration, J. Machado Miguens, *The ATLAS Run-2 Trigger: Design, Menu, Performance and Operational Aspects*, ATL-DAQ-SLIDE-2016-448 (2016) . <https://cds.cern.ch/record/2205808>.

- [98] R. Hauser, *The ATLAS Data Acquisition and High Level Trigger Systems: Experience and Upgrade Plans*, ATL-DAQ-PROC-2012-073, CERN, Geneva, 2012. <https://cds.cern.ch/record/1497132>.
- [99] GEANT4 Collaboration, S. Agostinelli et al., *GEANT4: A simulation toolkit*, Nucl. Instrum. Meth. A **506** (2003) 250–303.
- [100] J. Alwall, M. Herquet, F. Maltoni, O. Mattelaer, and T. Stelzer, *MadGraph 5 : Going Beyond*, JHEP **1106** (2011) 128, arXiv:1106.0522 [hep-ph].
- [101] T. Sjostrand, S. Mrenna, and P. Skands, *PYTHIA Generator version 6.418*, JHEP **05** (2006) 026.
- [102] P. M. Nadolsky, H.-L. Lai, Q.-H. Cao, J. Huston, J. Pumplin, D. Stump, W.-K. Tung, and C. P. Yuan, *Implications of CTEQ global analysis for collider observables*, Phys. Rev. **D78** (2008) 013004, arXiv:0802.0007 [hep-ph].
- [103] J. Pumplin et al., *New generation of parton distributions with uncertainties from global QCD analysis*, JHEP **07** (2002) 012.
- [104] A. Martin, W. Stirling, R. Thorne, and G. Watt, *Uncertainties on alpha s in global PDF analyses and implications for predicted hadronic cross sections*, Eur.Phys.J.C - Particles and Fields **64** (2009) 653–680.
- [105] P. Nason, *A new method for combining NLO QCD computations with parton shower simulations*, JHEP 11(2004)-040, hep-ph/0409146 (2004) .
- [106] T. Gleisberg, S. Hoeche, F. Krauss, M. Schonherr, S. Schumann, F. Siegert, and J. Winter, *Event generation with SHERPA 1.1*, JHEP **02** (2009) 007, arXiv:0811.4622 [hep-ph].
- [107] ATLAS Collaboration, *Expected electron performance in the ATLAS experiment*, Tech. Rep. ATL-PHYS-PUB-2011-006, CERN, Geneva, 2011. <https://cds.cern.ch/record/1345327>.
- [108] ATLAS Collaboration, *Electron efficiency measurements with the ATLAS detector using the 2015 LHC proton-proton collision data*, ATLAS-CONF-2016-024 . <https://cds.cern.ch/record/2157687>.
- [109] A. Ezhilov, *Electrons in ATLAS: from Run1 to Run2*, ATL-PHYS-PROC-2015-180, CERN, Geneva, 2015. <https://cds.cern.ch/record/2112121>.

- [110] ATLAS Collaboration, *Preliminary results on the muon reconstruction efficiency, momentum resolution, and momentum scale in ATLAS 2012 pp collision data*, ATLAS-CONF-2013-088 . <https://cds.cern.ch/record/1580207>.
- [111] ATLAS Collaboration, *Muon reconstruction performance of the ATLAS detector in protonproton collision data at  $\sqrt{s} = 13$  TeV*, Eur. Phys. J. **C76** (2016) no. 5, 292, arXiv:1603.05598 [hep-ex].
- [112] M. Cacciari, G. Salam, and G. Soyez, *The anti- $k_t$  jet clustering algorithm*, Journal of High Energy Physics **2008** (2008) no. 04, 063.
- [113] ATLAS Collaboration, *Tagging and suppression of pileup jets with the ATLAS detector*, ATLAS-CONF-2014-018 . <https://cds.cern.ch/record/1700870>.
- [114] J. W. Hetherly and A. Collaboration, *Real-time Flavour Tagging Selection in ATLAS*, ATL-DAQ-PROC-2015-035, CERN, Geneva, 2015.  
<https://cds.cern.ch/record/2057644>.
- [115] T. P. Calvet, *Expected b-tagging performance for ATLAS in LHC Run 2*, ATL-PHYS-PROC-2015-104, CERN, Geneva, 2015.  
<https://cds.cern.ch/record/2058102>.
- [116] ATLAS Collaboration, *Performance of Missing Transverse Momentum Reconstruction in Proton-Proton Collisions at 7 TeV with ATLAS*, Eur.Phys.J. **C72** (2012) 1844.
- [117] ATLAS Collaboration, *Expected performance of missing transverse momentum reconstruction for the ATLAS detector at  $\sqrt{s} = 13$  TeV*, ATL-PHYS-PUB-2015-023, CERN, Geneva, 2015. <https://cds.cern.ch/record/2037700>.
- [118] R. Schwienhorst, C. P. Yuan, C. Mueller, and Q.-H. Cao, *Single top quark production and decay in the t-channel at next-to-leading order at the LHC*, Phys. Rev. **D83** (2011) 034019, arXiv:1012.5132 [hep-ph].
- [119] Moneta, Lorenzo and Belasco, Kevin and Cranmer, Kyle and Lazzaro, Alfio and Piparo, Danilo and Schott, Gregory and Verkerke, Wouter and Wolf, Matthias and Belasco, Kevin and Cranmer, Kyle and Lazzaro, Alfio and Piparo, Danilo and Schott, Gregory and Verkerke, Wouter and Wolf, Matthias, *The RooStats Project*, PoS **ACAT2010** (2010) no. arXiv:1009.1003, 057.  
<https://cds.cern.ch/record/1289965>.

- [120] P. Royston, *Profile likelihood for estimation and confidence intervals*, Stata Journal **7** (2007) no. 3, 376–387(12).
- [121] A. A. Maier, *Statistical and systematic treatment issues in top quark mass combinations*, ATL-PHYS-PROC-2015-168, CERN, Geneva, 2015.  
<https://cds.cern.ch/record/2110988>.
- [122] V. Balagura, *Notes on van der Meer Scan for Absolute Luminosity Measurement*, Nucl. Instrum. Meth. **A654** (2011) 634–638, arXiv:1103.1129 [physics.ins-det].
- [123] ATLAS Collaboration, *Improved luminosity determination in pp collisions at  $\sqrt{s} = 7$  TeV using the ATLAS detector at the LHC*, Eur. Phys. J. **C73** (2013) no. 8, 2518, arXiv:1302.4393 [hep-ex].
- [124] ATLAS Collaboration, *Jet energy measurement and systematic uncertainties using tracks for jets and for b-quark jets produced in proton-proton collisions at  $\sqrt{s} = 7$  TeV in the ATLAS detector*, ATLAS-CONF-2013-002 .  
<https://cds.cern.ch/record/1504739>.
- [125] W. Spearman, *Study of the ATLAS muon identification efficiency in the presence of high pile-up*, ATL-MUON-PROC-2012-007, CERN, Geneva, 2012.  
<https://cds.cern.ch/record/1478180>.
- [126] L. Fayard, C. R. Goudet, T. Guillemin, L. Iconomidou-Fayard, S. Manzoni, K. Tackmann, R. Turra, P. Mastrandrea, and G. Unal, *Energy calibration prerecommendation for Run 2*, ATL-COM-PHYS-2015-1300 (2015) .  
<https://cds.cern.ch/record/2060328>.
- [127] ATLAS Collaboration, *Reconstruction and Calibration of Missing Transverse Energy and Performance in Z and W events in ATLAS Proton-Proton Collisions at 7 TeV*, ATLAS-CONF-2011-080 . <https://cds.cern.ch/record/1355703>.
- [128] ATLAS Collaboration, *Jet Calibration and Systematic Uncertainties for Jets Reconstructed in the ATLAS Detector at  $\sqrt{s} = 13$  TeV*, ATL-PHYS-PUB-2015-015 (2015) . <https://cds.cern.ch/record/2037613>.
- [129] ATLAS Collaboration, *Jet global sequential corrections with the ATLAS detector in proton-proton collisions at  $\sqrt{s} = 8$  TeV*, ATLAS-CONF-2015-002 .  
<https://cds.cern.ch/record/2001682>.
- [130] ATLAS Collaboration, *Performance of b-Jet Identification in the ATLAS Experiment*, JINST **11** (2016) no. 04, P04008, arXiv:1512.01094 [hep-ex].

- [131] LHC Top Working Group, *NNLO+NNLL top-quark-pair cross sections*,  
<https://twiki.cern.ch/twiki/bin/view/LHCPhysics/TtbarNNLO>.
- [132] LHC Top Working Group, *NLO single-top channel cross sections*,  
<https://twiki.cern.ch/twiki/bin/view/LHCPhysics/SingleTopRefXsec>.
- [133] C. J. E. Suster,  *$t\bar{t}W$  and  $t\bar{t}Z$  production cross section in leptonic final states at 8 TeV with ATLAS*, ATL-PHYS-PROC-2015-156, CERN, Geneva, 2015.  
<https://cds.cern.ch/record/2108895>.